内容提要

本报告由三部分组成。第一部分围绕量子级联激光器的材料生长及器件探索这一主题，分别对 InP 衬底上 InGaAs/InAlAs 异质结构材料的生长工艺进行探索和改进，掌握了 InP 基微结构材料的主要生长技术。在此基础上成功地在*本所生产的 InP 衬底*上制备出 InGaAs/InAlAs 优质量子级联激光材料。具体指标为：(1)每层层厚在 0.9-6.8nm 范围而总层数大于 500 层的级联激光材料的双晶 x 射线显示出 20 级以上的卫星峰；(2)全器件(总厚 4-5μm)的晶格失配度 $\Delta a/a_s=3\text{-}6\times10^{-4}$；(3)在有意舍弃激光器的第一级注入区后，宽接触器件的 I-V 曲线显示出显著的负微分电阻，表明材料的界面平整度较好。目前已研制出宽接触及条形激光器原型器件，器件的 I-V 特性已接近 AT&T Bell 实验室 F.Capasso 等人的结果。器件的进一步测试及评估工作正在进行中。第二部分是关于 In(GaAs)/InAlAs/InP 量子点结构材料的生长及光学性质研究，这部分是对 InP 衬底上异质结材料的生长与工艺控制的补充，包括三篇独立的研究论文，分别对 InAs 量子点的纵向尺寸量子化及光学性质、$In_{0.9}Ga_{0.1}As$ 横向尺寸的双重分布及光学性质，以及量子点组装量子线进行研究。第三部分由两篇研究论文组成，分别对嵌埋于多空硅中的 Ge 团簇及表面氧化 Ge 团簇的光学性质进行研究。

关键词：量子级联激光器，异质结构材料，I-V 特性，负微分电阻，量子点，团簇。

目 录

绪 论

本报告由三部分组成。第一部分是 InP 衬底上 InGaAs/InAlAs 量子级联激光器的材料生长及物理问题研究，围绕该激光器的工作原理、材料设计、材料生长进行探索研究；第二部分是关于 In(GaAs)/InAlAs/InP 量子点结构材料的生长及光学性质研究；第三部分是关于 Ge 团簇制备及光学性质研究。

1. "量子级联激光器的材料生长及物理问题研究"是国家九五"863"项目"新型红外激光晶体材料及应用技术"的子课题、国家自然科学基金"量子级联激光材料及器件探索"及中国博士后基金"量子级联激光器中 Bragg 反射器的设计及材料生长"的部分研究内容。

以量子级联激光器为先导的新型量子阱、超晶格子带/微带激光器，以其优越的性能及其在材料选取、器件设计等方面前所未有的自由度，为新一代中、远红外半导体激光器的研制注入了新的活力，展示了诱人的发展前景。

迄今包括和量子阱激光器在内的所谓传统半导体激光器无不基于正向偏置 PN 结导带和价带之间的辐射复合，因而带隙决定了工作波长。例如 III-V 族材料 GaAs/GaAlAs、InGaAsP/InP 双异质结激光器的发射波长分别约 0.85μm 和 1.55μm，最长的 InGaAsSb 和 InAsPSb 也不过约 4μm，再长波长只能采用 IV-IV 族的铅盐系及 II-VI 族的汞硫系等所谓窄带隙材料了。但窄带隙材料制备技术还欠成熟，难以制备无缺陷的材料。而窄带隙材料本身的种种不足，如过大的俄歇复合损耗以及过大的自由载流子吸收损耗等，又为高性能激光器的研制增加了新的难度。尽管在材料生长及器件制备方面一直进行着艰辛努力，但窄带隙 PN 结半导体激光器如果仍沿用以往的模式是很难有所作为的。

量子级联激光器的出现开创了利用宽带隙材料研制中、远红外半导体激光器的先河，在中、远红外半导体激光器的发展史上树立了新的里程碑。

量子级联激光器是利用单极载流子(电子)注入多级串接的耦合量子阱有源区及梯度带隙超晶格结构弛豫/注入区，而在耦合量子阱有源区的子带间产生粒子数反转分布并产生受激辐射的。该激光器的工作波长与所用材料的带隙无直接关系，仅由耦合量子阱子带间距决定，因而由耦合量子阱有源区的阱/垒宽度决定。原则上利用同一种量子阱材料就可得到从中红外至远红外甚至亚毫米波的不同波长的激光。这种独特的激射波长"剪裁"特性和如此宽的光谱范围是传统激光器无法与之媲美的。这种单极粒子跃迁辐射具有单向偏振(TM 波)性，极适合于"回音壁模式"微腔激光器的制作。这些跃迁态的联合态密度和相应的增益光谱半宽都很窄且对称，因而可望实现低阈值激光器和单纵模工作。此外，与窄带隙的铅盐等材料相比，InGaAs/InAlAs 宽带隙材料具有较小的温度敏感系数；由于子带间俄歇复合可以忽略，因而量子级联激光器具有较大的特征温度，极有利于器件的室温工作。就中、远红外波段而言，大气透射的三个重要红外窗口(1~2.7μm，3~5μm，8~14μm)基本上都处于量子级联激光器的的工作波段之内。因此，量子级联激光器的即具有极大的军事应用潜力(如中远红外夜视、中远红外光学雷达、红外通信等)、极好的民用市场前景(如大气污染监测、工业烟尘分析、化学过程监测等)，也具有重要的科学研究价值(如光谱学研究、遥感及痕量气体监测等)，作为中、远红外波段的新型光源具有广阔的发展前景。国际上美、日等发达国家对量子级联激光器的研究予以极大关注。AT&T Bell 实验室 94 年首先实现低温脉冲激射而荣获当年"Science"杂志优秀论文奖，96 年器件实现室温脉冲激射。

由于量子级联激光器的研制还处于起步阶段，许多问题还有待于研究。本报告是对该国际前沿领域的跟踪及探索。通过对 InGaAs/InAlAs 异质结构材料的生长工艺进

行改进，基本掌握了 InP 基微结构材料的主要生长技术，成功地在本所生产的 InP 衬底上制备出 InGaAs/InAlAs 优质量子级联激光材料。另外对量子级联激光器的材料生长相关的物理问题进行了研究。

2. "In(GaAs)/InAlAs/InP 量子点结构材料的生长及光学性质研究" 是院九五重大项目 "InP 基半导体微结构、微器件及相关物理研究" 的子课题 "InP 基半导体微结构材料物理研究" 的部分内容。

    目前量子点的制备及其应用研究正引起人们极大的兴趣，八十年代初人们就预言量子点激光器的许多优异特性，比如量子点激光器进一步改善了温度特性，更高的增益和更低的阈值电流密度等。此后，相继发展了各种各样的量子点制备方法，如在高质量超晶格、量子阱材料的基础上采用横向微加工技术刻蚀量子点。这些方法制备量子点的优点在于尺寸均匀可控，但加工带来的损伤及横向尺寸较大使这些材料发光效率低，距实际应用还有很大的差距。近几年来，利用自组装生长模式原位生长量子点取得了很大成功。目前这种生长方法涉及的材料体系 GeSi/Si，In(Ga)As/GaAs，InGaAs/AlGaAs 等，量子点的发光波长覆盖了从近红外到可见光的范围。 InP 基 In(Ga)As 量子点的发光波长在 $1.3 \sim 2 \mu m$ 附近，是该波段量子点激光器的首选材料。与 Si 基及 GaAs 基量子点的研究相比，InP 基量子点的研究还很少。这方面的研究一方面拓宽了 InP 基半导体微结构材料研究领域，另一方面也是为应变补偿量子级联激光器的材料生长打下基础。

3. "Ge 团簇制备及光学性质研究" 是对博士阶段部分研究工作的继续和深化。

    半导体团簇及团簇组装纳米材料目前是半导体科学和材料科学的热点之一，这方面的研究将和自组装原位生长量子点及微加工技术刻蚀量子点互为补充，构成二十一世纪半导体纳米科技诞生的温床。本报告的第三部分就嵌埋 Ge 团簇和支撑 Ge 团簇的光学性质进行研究。

    限于作者的水平和时间关系，文中错误和疏漏之处在所难免，敬请批评指正。

量子级联激光器的工作原理

量子级联激光器是一种基于子带间电子跃迁的中红外波段单极光源[1]。近年来，量子级联激光器已成功地工作在一个很宽的波长(3.5~11.5μm)[2-7]和温度(液 H_2 至室温)范围。多种结构的连续激射得以演示，典型功率为 10~20mW ，而脉冲输出功率已达数百 mW 。
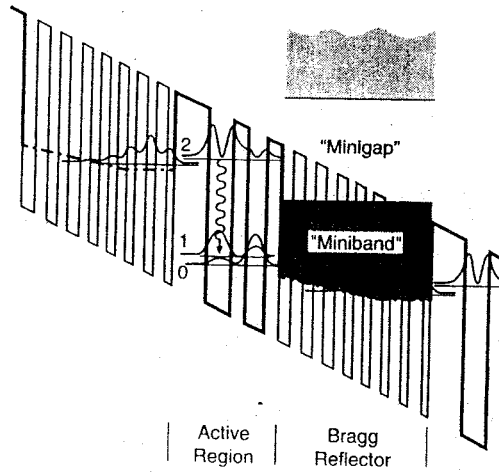

图 1 正向偏压下量子级联激光器的部分有源区结构的导带示意图。每一级(周期)的 $In_{0.52}Al_{0.48}As/In_{0.53}Ga_{0.47}As$ 层厚及顺序为，自左至右从注入势垒开始(单位 nm): (6.8/4.8), (2.8/3.9), (2.7/2.2), (2.2/2.1), (2.1/2.0), (2.0/*1.8*), (*1.8/1.7*), (*2.0/1.6*), (*2.2/1.6*), (2.4/1.4)。其中下划线部分(12-18 层)N 型掺杂至约 $3\times10^{17}cm^{-3}$ 。

量子级联激光器的有源区由多级串接组成，如图 1 所示[3,4]，每一级又由耦合量子阱有源区和梯度带隙超晶格结构弛豫/注入区构成。弛豫/注入区的作用是从有源区的一侧注入电子，而从另一侧收集电子并在电子注入到下一级有源区之前使其充分弛豫降低能量(冷却)，以避免因电子速度过高(较宽的速度分布函数)而引起的隧穿效率降低[1]。在阈值电压下，有源区的两个低能态子带(n=1 和 n=2)间距等于光学声子能量，这两个子带间的散射时间很小($\tau_{21}\leq0.6ps$)，导致 n=2 态的寿命很短；另一方面，子带 3 与子带 2 之间的间距较大，与大的动量转移相关的光学声子发射使得子带 3 与子带 2 之间的散射时间相当长($\tau_{32}\geq2ps$)，导致 n=3 态的寿命较长(1.3ps)，满足粒子数反转条件。梯度带隙超晶格结构弛豫/注入区设计成 n=3 态电子波的 Bragg 反射器而具有抑制电子从耦合阱的 n=3 激发态的逃逸和促使电子从耦合阱的低能态(n=1)顺序遂穿抽运的双重作用。当注入能量对应于 n=3 态要求每一对阱垒满足 Bragg 反射条件。

从 n=1 态散射出来的电子进入梯度带隙超晶格结构区迅速弛豫其动量和能量。有两种因素促使这种迅速弛豫：一方面是因为梯度带隙超晶格结构区的能级之间分离很小(几十 meV ，如图 2 所示；另一方面在于子带间的弹性散射，而梯度带隙区超薄层的界面粗糙和掺杂有利于这种子带间的弹性散射。
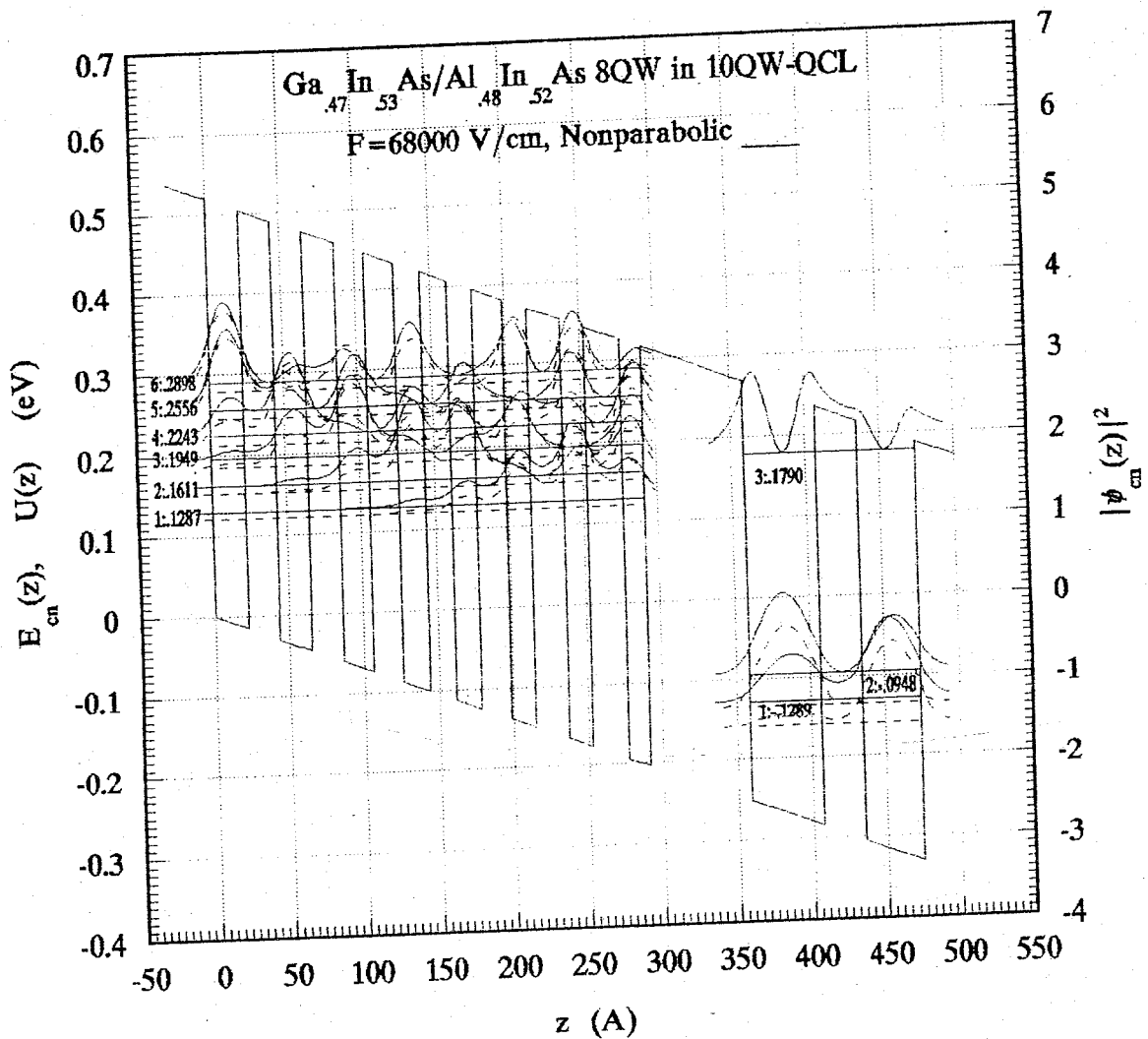
图2 一定正向偏压下量子级联激光器一个周期的耦合量子阱有源区和梯度带隙超晶格结构弛豫/注入区的导带示意图. 弛豫/注入区的能级间距~30-34meV.

梯度带隙区域的准费密能级和激光跃迁的最低能态之间的能量差 Δ 是一个控制器件高温特性的重要参量, 因为在阈值条件下为了满足反转条件, 则 n=2 态的热布居 (~exp(-Δ/kT))必须借助于较大的注入电流来补偿. 增大Δ 将降低高温下的阈值电流、提高最大工作温度、增加连续波的斜效率. 对于 n=3 态, 阈值电场由其对应的梯度带隙注入器的平带排列决定. Δ (阈值偏压)正比于注入器的长度.

2

参考文献

1. J.Faist, F.Capasso, D.L.Sivco, C.Sirtori, A.L.Hutchinson and A.Y.Cho, Science **264**, 553(1994); B.G.Levi, Phys. Today (July), 20(1994).

2. J.Faist, F.Capasso, D.L.Sivco, A.L.Hutchinson, S.-N.G.Chu, and A.Y.Cho, Appl.Phys.Lett. **72**, 680(1998).

3. J.Faist, F.Capasso, C.Sirtori, D.L.Sivco, A.L.Hutchinson and A.Y.Cho, Appl.Phys.Lett. **66**, 538(1995).

4. J.Faist, F.Capasso, C.Sirtori, D.L.Sivco, A.L.Hutchinson and A.Y.Cho, Appl.Phys.Lett. **67**, 3057(1995).

5. J.Faist, F.Capasso, C.Sirtori, D.L.Sivco, J.N.Baillargeon, A.L.Hutchinson, S.-N.G.Chu, and A.Y.Cho, Appl.Phys.Lett. **68**, 3680(1996).

6. C.Sirtori, J.Faist, F.Capasso, D.L.Sivco, A.L.Hutchinson, S.N.G.Chu, and A.Y.Cho, Appl.Phys.Lett. **68**, 1745(1996).

7. C.Gmachl, J.Faist, F.Capasso, C.Sirtori, D.L.Sivco, and A.Y.Cho, IEEE J.Quantum Electron.**33**, 1567(1997).

量子级联激光器的初步设计

量子级联激光器的有源区由多级串接组成，每一级又由耦合量子阱有源区和梯度带隙超晶格结构弛豫/注入区构成。弛豫/注入区的作用是从有源区的一侧注入电子，而从另一侧收集电子并在电子注入到下一级有源区之前将其冷却[1]。我们以双阱耦合有源区为例[2,3]，对其设计原理进行初步探索。

1. 激光跃迁量子阱的设计

要满足激射条件，量子级联激光器的外加电场必须是由窄阱指向宽阱。如图 1 所示，在阈值电压下：

$$E_{3F}-E_{2F}=h\nu=1.24/\lambda_0 \tag{1}$$

下标 F 表示电场。假设我们需要激射波长为 $\lambda_0=4.2\mu m$，则 $E_{3F}-E_{2F}=0.2952eV$ 可近似地选取 $E_3-E_2=E_{3F}-E_{2F}$。对 InGaAs/InAlAs 量子阱，考虑非抛物性(取非抛物性因子$\gamma=1.13\times10^{-14}cm^2$)的校正后，上述能级差 0.2952eV 对应于阱宽 4.4nm (两个能级分别为 0.1481 和 0.4434eV)[4]。

2. 窄阱及耦合势垒的设计
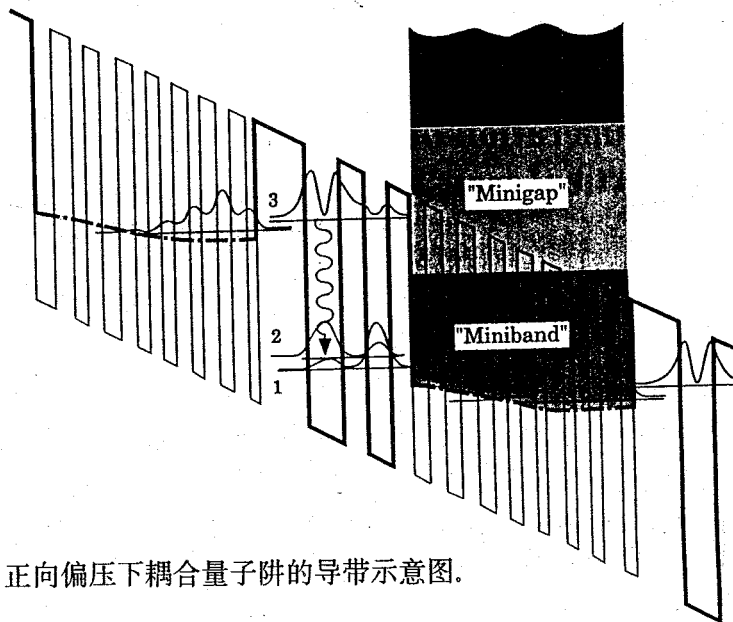
图 1 正向偏压下耦合量子阱的导带示意图。

为了满足粒子数反转条件，提高辐射跃迁效率，子带间由光学声子限制的非辐射跃迁时间τ_{32}应尽量长。另一方面，为了抽空 n=2 态应使 n=2 态的寿命($\tau_2\sim\tau_{21}$)尽量短。为了达此目的，通常使两个量子阱的基态在阈值电场下反交迭，并使 n=1 态和 n=2 态的间距近似等于光学声子能量(~34meV)。这两个低能态之间的光学声子共振发射使这两个能级间的散射时间很小($\tau_{21}\leq0.6ps$)，导致 n=2 态的寿命很短。这是窄阱及耦合势垒设计一个的原则。即：

$$E_{2F}-E_{1F}=0.034eV \tag{2}$$
$$\tau_{21}=0.6ps(与耦合势垒有关) \tag{3}$$
$$E_{3F}=E_3-(d_{w1}/2)\cdot F \tag{4}$$
$$E_{2F}=E_2-(d_{w1}/2)\cdot F \tag{5}$$
$$E_{1F}=E_1-[d_{w1}+d_b+d_{w2}/2]\cdot F \tag{6}$$

$$E_2 - E_1 = E_{2F} - E_{1F} - [(d_{w1} + d_{w2})/2 + d_b] \cdot F \qquad (7)$$

$$E_1 = E_2 - (E_{2F} - E_{1F}) + [(d_{w1} + d_{w2})/2 + d_b] \cdot F \qquad (8)$$

其中 d_{w1} 和 d_{w2} 分别为两个阱的厚度，d_b 是耦合势垒的厚度。以上各参数尚有 d_{w2}、d_b 和 F 需要确定。

子带间光学声子限制的散射时间 τ_{21}、τ_{32} 由非辐射散射决定，因为光学声子发射是主要的非辐射跃迁。低温下子带间的纵光学声子散射速率可以由下式计算[5,6]：

$$W_{ij}(k_t) = \frac{e^2 \omega_0 [n(\omega_0) + 1]}{8\pi\epsilon_\rho} \times \int \frac{|\langle j|e^{iq_z z}|i\rangle|^2}{\sqrt{\frac{\hbar^4 k_t^2 q_z^2}{2m^*} + \left(\frac{\hbar^2 q_z^2}{2m^*} + E_i - E_j - \hbar\omega_0\right)^2}} dq_z \qquad (9)$$

其中 $n(\omega_0)$ 是光学声子数，ω_0 是纵光学声子频率，k_t 是电子在平面内的动量，q_z 是声子动量的 z 分量，E_i 和 E_j 分别是 $k_t = 0$ 时第 i 及第 j 个子带的能量，ϵ_ρ 是约化介电常数：

$$\epsilon_\rho^{-1} = \epsilon_0^{-1} + \epsilon_\infty^{-1} \qquad (10)$$

在 $k_t = 0$ 时电子在 n=3 及 n=2 态的寿命为

$$\tau_3^{-1} \approx W_{31} + W_{32} \quad ; \quad \tau_2^{-1} \approx W_{21} \qquad (11)$$

电子在 n=2 态的寿命对电子的动量十分敏感。电子从子带 3 经过一个大的动量转移后，W_{21}^{-1} 在 $k_t \neq 0$ 时约为 ~1ps，而当 $k_t = 0$ 时，电子在 n=2 态的寿命 $\tau_2 \approx \tau_{21} = W_{21}^{-1} < 0.6$ps 非常短。如果确定了阈值电场 F，由以上关系式可以确定窄阱及耦合势垒的厚度。

3. 注入区及其等效带底的拉平——确定阈值电场 F

为了增加 n=3 激发态的限制作用以阻止电子从 n=3 态向连续态的逃逸及促使电子从耦合阱的 n=1 低能态顺序遂穿抽运作用，梯度带隙超晶格结构设计成阈值电压下使有效导带底维持平带，当注入能量对应于 n=3 态时，这就要求每一对阱和垒满足 n=3 态的电子波的 Bragg 反射条件。我们用 x_j 代表梯度带隙超晶格第 j 个周期的位置，则有效导带势满足以下关系式：

$$V(x_j) \cong \triangle E_c \frac{l_{b,j}}{l_{w,j} + l_{b,j}} \qquad (12)$$

这里 $\triangle E_c = 0.52$eV 是阱垒材料的导带带阶。阈值电压下有效导带势产生的准电场抵消外加电场 F_{th}：

$$\frac{V(x_j) - V(x_{j-1})}{(l_{b,j} + l_{w,j})} = -F_{th} \qquad (13)$$

每一对阱和垒层 (l_{wj}, l_{bj}) 满足 Bragg 反射条件：

$$k_{wj} l_{wj} + k_{bj} l_{bj} = \pi \qquad (14)$$

这里 k_{wj} 和 k_{bj} 分别是阱中和垒中的波数。这个条件保证被所有周期反射的电子波的相长干涉。

$$k_{w,j} = \sqrt{2m_{wj}E_{3F}}/\hbar \quad ; \quad k_{b,j} = \sqrt{2m_{bj}(V(x_j) - E_{3F})}/\hbar \qquad (15)$$

$$E_{3F} = E_3 - V_p \qquad (16)$$

其中 V_p 为一个周期的电压降。

将上述一组方程式对每一相继的阱垒对进行迭代求解，便可具体得到梯度带隙超晶格每对阱垒层的厚度。

4. 梯度带隙超晶格组成 Bragg 反射器的"微带"及"微带隙"
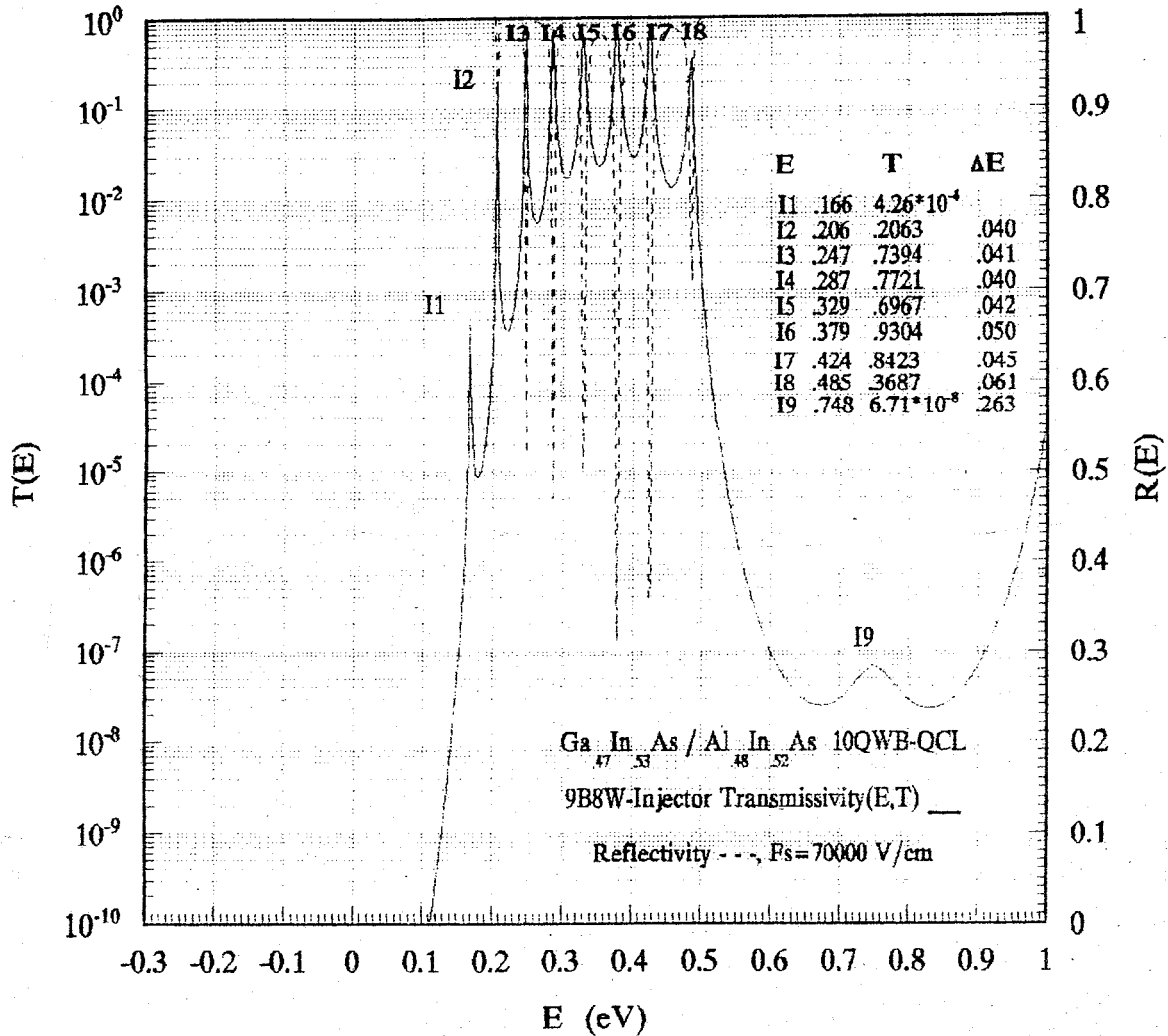
图2 计算得到的正向偏压 70000V/cm 下梯度带隙区的透射谱随能量的变化关系。

在正向偏压下，梯度带隙弛豫区的电子能谱类似于常规的超晶格的能谱。它有一个面对有源区低能态的微带而促使激光跃迁基态的电子有效的逃逸；另外，它有一个面对有源区高能态的微带隙而有效地阻止电子从高能态的逃逸。这种对高能态的拘禁效应可以从梯度带隙区的透射谱(图2)中清楚地看出。对应于 n=3 态的能量处的透射系数很低(<10^-7)；而对应于 n=1 态的能量处的透射系数却保持足够大，保证了从 n=1 态的迅速逃逸(<0.6ps)。

6

为了计算梯度带隙区的透射系数, 我们仿照光学法布里－玻罗腔的原理对电子隧穿的一维运动作较详细的分析[7,8].

考虑图 1 的 9 垒 8 阱梯度带隙的电子穿透问题(行波解). 取入射波(平面波)的振幅为 1. 设 r_{ij} 和 t_{ij} 分别代表电子隧穿单个势垒时的反射波和透射波复振幅, i 代表入射区, j 代表出射区. 实际上 r_{ij} 和 t_{ij} 就是电子隧穿单个势垒问题的解. 设电子从耦合量子阱有源区入射到右边的 9 垒 8 阱梯度带隙区, 最后从右边射出, 出射波的复振幅为 S. 另一方面可以设想, 入射波首先隧穿过左边单个势垒, 其入射波的复振幅为 t_{13}, 这个波在势阱中来回反射, 每在右边势垒反射一次, 都有一部分从右边势垒射出. 总的出射波振幅为 S 可以看作多束波隧穿过最右边的势垒后的出射波的叠加:

S=S₁+S₂+S₃+...

$$= \frac{t_{1,3}t_{3,5}}{1-r_{3,5}r_{3,1}} \cdot \frac{t_{5,7}t_{7,9}}{1-r_{7,9}r_{7,5}} \cdots \frac{t_{15,17}t_{17,19}}{1-r_{17,19}r_{17,15}} \tag{17}$$

总的透射几率为

$$T = \frac{k_{19}}{k_1} S \cdot S^* \tag{18}$$

将上式与(14)式的 Bragg 反射条件联合起来, 就可以求解梯度带隙区的透射系数.

这里还涉及一个问题是, 单个势垒的 r_{ij} 和 t_{ij} 在能量高于及低于势垒之上具有截然不同的表达式. 这就使问题变得更加复杂. 这也是 Bragg 反射器对 E_3 和对 E_1 及 E_2 具有不同的透射几率的真正根源所在.

我们还可以从另一条途径求解透射系数. 将电子波与光波类比. 在正向偏压下, 设电子的能量为 E_F, 电子在阱、垒中的波矢分别为

$$k_w = \sqrt{2m_w E_F}/\hbar = \frac{2\pi}{\lambda_w} = \frac{2\pi}{\lambda_e} \cdot N_w \tag{19}$$

$$k_b = \sqrt{2m_b(V_{bc} - E_F)}/\hbar = \frac{2\pi}{\lambda_b} = \frac{2\pi}{\lambda_b} \cdot N_b \tag{20}$$

其中 λ_w 和 λ_b 分别为阱和垒中的电子波长, λ_e 为真空电子波长, N_w 和 N_b 是阱和垒中的电子波等效折射率. 等效折射率为 N_j, 厚度为 d_j 的第 j 层膜对于真空电子波长为 λ_e 的电子波的特征矩阵为

$$M_j = \begin{bmatrix} \cos\delta_j & i\cdot\frac{\sin\delta_j}{N_j} \\ iN_j\sin\delta_j & \cos\delta_j \end{bmatrix} \qquad \delta_j = \frac{2\pi}{\lambda_e} \cdot N_j d_j \tag{21}$$

每一个阱垒对的特征矩阵为

$$M = M_1 M_2 = \begin{bmatrix} m_{11} & m_{12} \\ m_{21} & m_{22} \end{bmatrix} \tag{22}$$

那么我们可以得到整个梯度带隙区的特征矩阵为

$$M_T = \begin{bmatrix} \mu_{11} & \mu_{12} \\ \mu_{21} & \mu_{22} \end{bmatrix} \tag{23}$$

利用(14)式的 Bragg 反射条件可以简化特征矩阵，从而求得透射系数。

5. 其它考虑

梯度带隙区域的准费密能级和激光跃迁的最低能态之间的能量差 Δ 是一个控制器件高温特性的重要参量，因为在阈值条件下为了满足反转条件，避免热化电子从弛豫区微带的高能态向有源区的反填充，则 n=2 态的热布居($\sim\exp(-\Delta/kT)$)必须借助于较大的注入电流来补偿。增大 Δ 将降低高温下的阈值电流、提高最大工作温度、增加连续波的斜效率。对于 n=3 态，阈值电场由其对应的梯度带隙注入器的平带排列决定。Δ（阈值偏压下）正比于注入器的长度。为了进一步提高注入效率，梯度带隙区的掺杂仅限于远离耦合量子阱有源区的中间层，而基态波函数集中的区域不掺杂，以尽可能减少施主杂质散射。

参考文献

1. J.Faist, F.Capasso, D.L.Sivco, C.Sirtori, A.L.Hutchinson and A.Y.Cho, Science **264**, 553(1994);

2. J.Faist, F.Capasso, C.Sirtori, D.L.Sivco, A.L.Hutchinson and A.Y.Cho, Appl.Phys.Lett. **66**, 538(1995).

3. J.Faist, F.Capasso, C.Sirtori, D.L.Sivco, A.L.Hutchinson and A.Y.Cho, Appl.Phys.Lett. **67**, 3057(1995).

4. 郭长志、陈水莲，私人通讯。

5. G.Sun and J.B.Khurgin, IEEE J.Quantum Electron. **29**, 1104(0993).

6. S.Slivken, C.Jelen, A.Rybaltowski, J.Diaz, and M.Razeghi, Appl.Phys.Lett. **71**, 2593(1997).

7. 阎守胜，甘子钊，*介观物理学*，北京大学出版社，1995 年。

8. 夏建白，朱邦芬，*半导体超晶格物理*，上海科学技术出版社，1995 年。

9. J.Faist, A.Tredicucci, F.Capasso, C.Sirtori, D.L.Sivco, J.N.Baillargeon, A.L.Hutchinson and A.Y.Cho, IEEE J.Quantum Electron.**34**, 336(1998).

10. 郭长志、陈水莲，*物理学报*，**46**(9)，1731(1997).

量子级联激光器的材料生长

利用 Riber 32p 分子束外延设备生长匹配在 n^+ InP 衬底上的 InGaAs/InAlAs 量子级联激光器结构。 n^+ InP 衬底 (掺 S, $n=3.2\times10^{18}cm^{-3}$)为本所生产。生长高质量的 InGaAs/InAlAs 量子阱(超晶格)是制备相关量子级联激光器的前提。利用分子束外延(MBE)技术开展 InGaAs/InAlAs 多量子阱、超晶格材料制备技术研究，主要从两方面考虑：一方面使层厚的涨落控制在一个单原子层左右，并抑制界面处 AlAs 和 InAs 的分凝，保证原子级平整的 InGaAs/InAlAs 界面；另一方面研究固溶体组分的变化引起的晶格失配和应力对材料质量的影响，确保晶格失配 $\Delta a_\perp/a_s$ 达到~10^{-4} 量级。要达到器件要求的质量必须考虑多种生长条件的影响，这主要包括：衬底的清洗及化学预处理，选则合适的衬底温度，选则合适的 V/III 束流比，选则合适的生长速率，掺杂浓度的精确控制等以及它们之间的相互影响。另外，考虑到 InGaAs 的最佳生长条件和 InAlAs 的条件存在差别，要生长高质量的材料，最好有两个 In 源炉可供使用。

1. 生长条件的优化

(1). 衬底制备: 要使 MBE 生长得以成功，最重要的是用合适的方法来制备衬底，因为衬底的表面处理严重影响着生长膜的质量。我们所用的衬底材料为本所生产的 InP(001) 衬底 (掺 Fe 的半绝缘衬底和掺 S 的 n 型衬底)。首先用丙酮和三氯乙烯等有机溶剂去油，然后依次用 $H_2SO_4:H_2O_2:H_2O=3:1:1$ 溶液腐蚀 3 分钟和 5:1:1 溶液腐蚀 6 分钟以去除机械抛光而造成的损伤层。最后用去离子水冲洗对样品表面进行钝化，经过滤的氮气吹干。再用 In 作焊接剂将衬底安装在 Mo 质样品架上，并立即送入 MBE 系统中以避免沾污。

(2). 衬底预除气: 经过去油和化学腐蚀处理后的 InP 衬底，在装进 MBE 系统中时，不可避免地会吸附一些氧、碳等杂质气体。衬底进入生长室之前必须先在除气室中加热至 250° 使其充分放气，达到 $<2\times10^{-9}Torr$。

(3). 脱氧化层及生长温度定标: 用反射高能电子衍射仪(RHEED)原位监测衬底表面的再构情况。取 InP 表面的氧化层在 540° 脱附，在 As₄ 束流 $1\times10^{-5}Torr$ 保护下 InP 表面将发生由 2×4 到 4×2 表面再构转变。由此可对生长温度进行定标。

(4). 生长条件的选取:

a. 衬底温度的考虑: 适当提高衬底温度，可以增加被吸附原子在表面的扩散长度，从而提高外延层晶格质量。当衬底温度达到某一临界值，可以实现 MBE 理想的台阶流生长模式而获得高质量的异质界面。由于 InP 表面是靠适当的 As 压来保护的，它不同于 MOCVD 生长中是靠磷烷来保护的。过高的生长温度将导致衬底表面 P 的析出和因三元合金在生长表面的分凝效应而产生的组份不均匀。一般衬底温度选则在 500-525°C 之间，我们选用 515°C。

b. V/III 束流比: 除了选则适当的 In、 Ga、 Al 束流外，As₄/(In+Ga)和 As₄/(In+Al)等效束流比是一个很关键的参量。依据生长速率的不同，我们选则在 15-25 之间。这主要是考虑到 As 压过高限制了表面 In、 Ga、 Al 等的表面迁移，而 As 压过低将使表面处于富 Ga、 Al 状态。另外在选取 In、 Ga、 Al 束流时，在无法保证完全匹配的情况下，应尽量避免出现负失配，因为负失配容易使表面出现凹凸不平。

c. *生长速率*：生长速率太高不易得到高质量的外延层，我们一般使生长速率在 0.6-0.9μm/h 范围。生长速率的标定由 RHEED 振荡周期及压片测量来实现。在生长时不宜采用中断生长方法来提高界面质量。尽管中断生长为表面原子提供了必要的迁移时间，但频繁地开启源炉挡板将使束流的涨落加剧。 InGaAs 和 InAlAs 层的 In 组份与失配度之间的关系分别为 $x=0.532+7.2\Delta a_\perp/a_s$ 和 $x=0.523+7.4\Delta a_\perp/a_s$。因此生长匹配在 InP 衬底上的 InGaAs/InAlAs 需要极为严格的组份配比，束流的 1% 涨落就会产生 7×10^{-4} 的晶格失配度，要使失配度小于 10^{-3} 必须保证束流涨落小于 2%(而具体到每一个源炉，其束流涨落应更小)。生长一个量子级联激光材料一般需要 5–8 小时，在这么长的时间内要达到以上精度，这实际上是对生长工艺极限的挑战：一方面受分子束外延设备系统的稳定性的制约；另一方面是液氮流量、流量稳定性及人为因素的干预和控制。
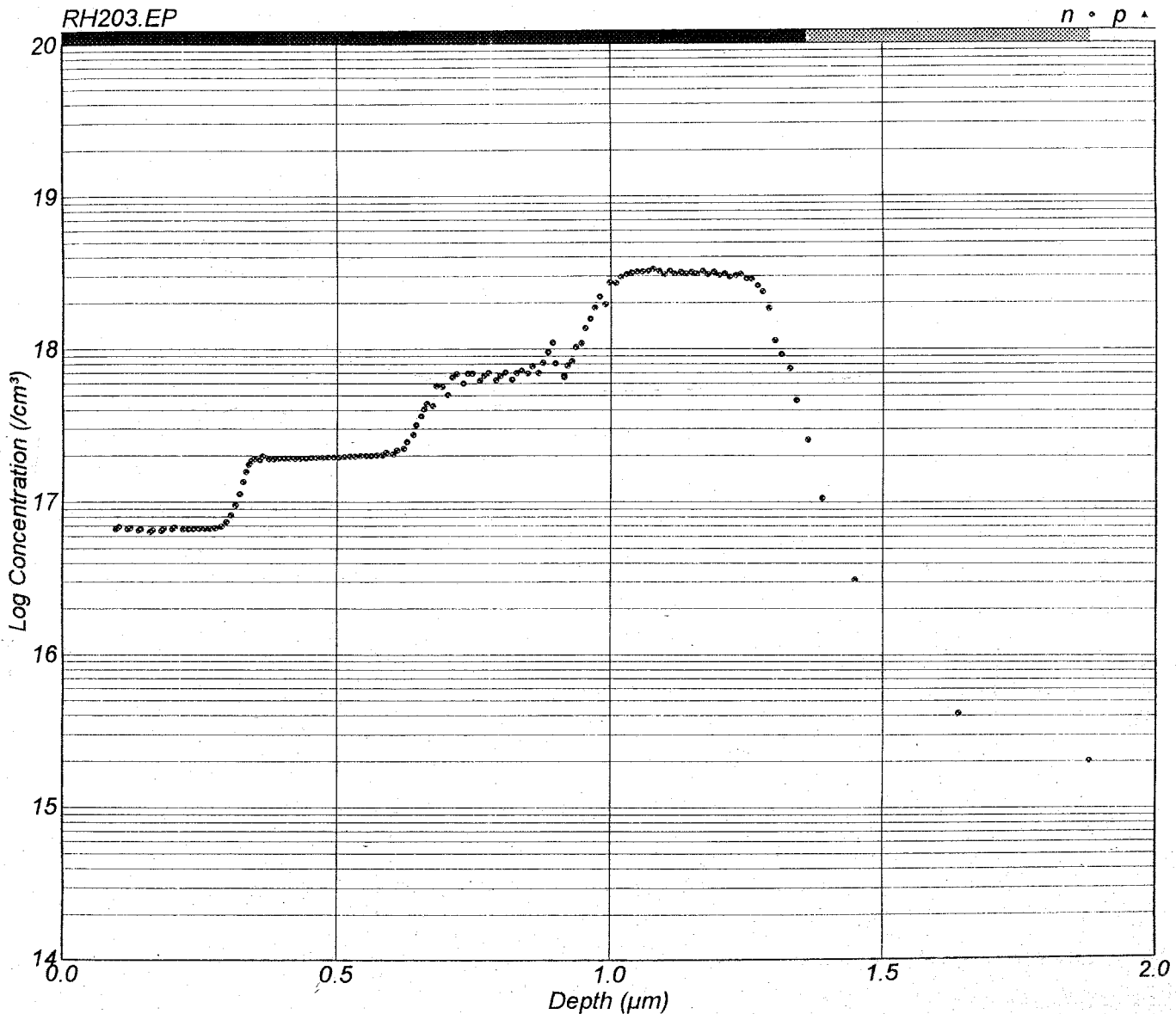

图 1. InGaAs/InP 外延层中 n 型掺杂台阶的电化学 C-V 结果(B927)。

d. *掺杂浓度*：量子级联激光材料仅需 n 型掺杂。掺杂浓度的大小及掺杂区域对量子级

联激光器的光谱特性产生很大的影响。精确控制掺杂浓度是一步关键工艺。我们用 Si 作为 n 型掺杂剂，在同一片衬底上生长 InGaAs 的 n 型掺杂台阶（每个台阶宽度不小于 350nm）可以得到在此生长速率下的掺杂浓度和 Si 炉温度的对应关系。同样可以得到某一生长速率下 InAlAs 中的掺杂浓度与 Si 炉温度的关系。掺杂浓度由电化学 C-V 方法确定，图 1 为一典型的 n 型掺杂台阶结果。控制好生长速率，将多个掺杂台阶的浓度与对应的 Si 炉温度(或温度倒数)实验结果线性拟合，得到图 2 和图 3 的半对数变化关系。
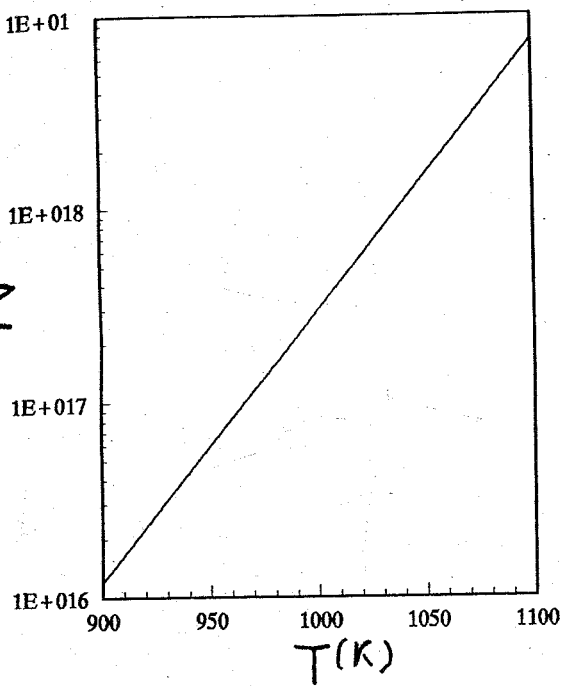
图 2. 生长速率为 0.824μm/h 时 InGaAs 外延层中掺杂浓度随 Si 炉温度的变化。
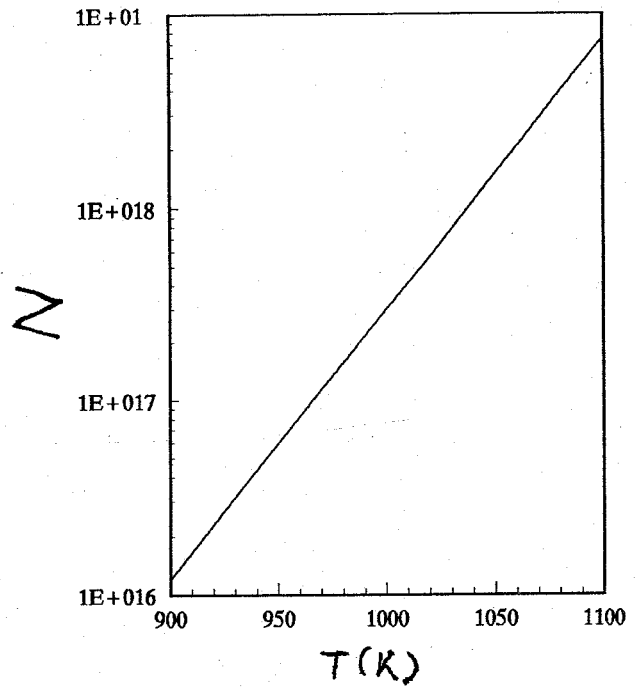
图 3. 生长速率为 0.84μm/h 时 InAlAs 外延层中掺杂浓度随 Si 炉温度的变化。

2. 外延质量鉴定

RHEED 原位观察：在生长材料时的最初阶段和最后阶段可以用 RHEED 原位观察手段对外延材料的生长质量有一个粗略的估计。一般情况下，生长初期由于氧化层的脱离和较高的衬底温度，As 压保护的 InP 表面不是特别平整，RHEED 图象为点、线共存；经过几秒钟外延以后，RHEED 图象很快变为线状。这是外延高质量材料的最基本的"风景点"之一。

双晶 X 射线(DCXRD)：由外延层衍射峰与 InP 衬底峰之间的角间距可以确定外延层与衬底在垂直方向上的晶格失配：

$$\frac{\triangle a_\perp}{a_s} = \triangle\theta \, ctg\theta_B \tag{1}$$

θ_B 为 Bragg 衍射角。

利用 Poisson 公式和 Vegard 定律得到晶格失配度和化学组份之间的关系

对 $In_{1-x}Ga_xAs$ 有

$$x = \frac{a_{InP}[1 + \frac{c_{11}}{c_{11}+2c_{12}} \cdot \frac{\triangle a_\perp}{a_{In_{1-x}Ga_xAs}}] - a_{InAs}}{a_{GaAs} - a_{InAs}} \qquad (2)$$

对 $In_{1-y}Al_yAs$ 有

$$y = \frac{a_{InP}[1 + \frac{c_{11}}{c_{11}+2c_{12}} \cdot \frac{\triangle a_\perp}{a_{In_{1-y}Al_yAs}}] - a_{InAs}}{a_{AlAs} - a_{InAs}} \qquad (3)$$

InGaAs/InP 及 InAlAs/InP 的双晶 X 射线衍射结果分别示于图 4 和图 5。
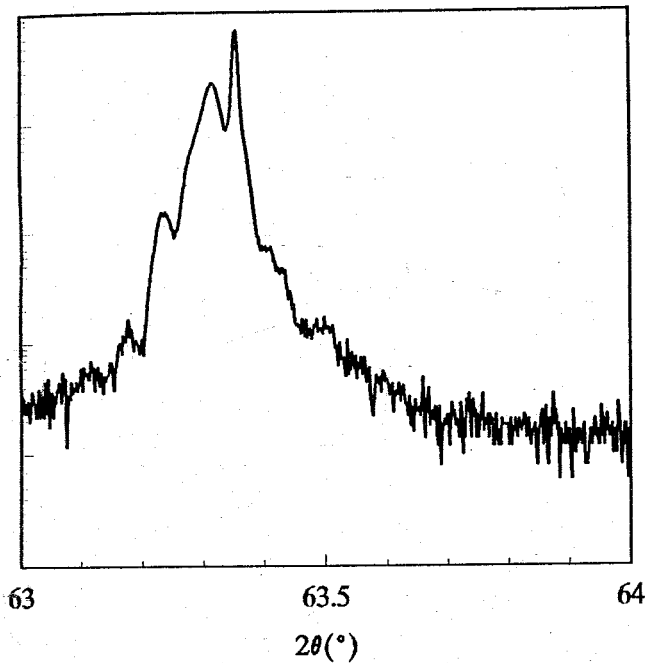
图 4. 外延层厚 1.5μm 时 InGaAs/InP 的
双晶 X 射线结果(B927)。
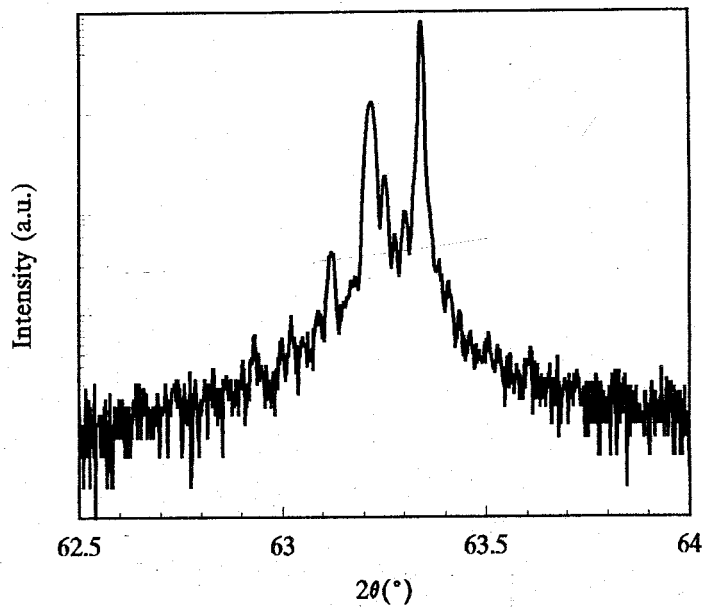
图 5. 外延层为 1.2μm 时 InAlAs/InP
双晶 X 射线结果(B924)

光荧光 由光荧光的峰位可以确定化学组份；而光荧光的半高宽可以作为评价外延材料质量的依据之一。图 6 是 30K 温度下 InGaAs/InP(样品号 B923)的光荧光结果。InGaAs 外延层的激子峰位在 0.799eV，半高宽为 7meV。外延层的厚度为 1.12μm，晶格失配度$\Delta a_\perp/a_s$ =-5.66×10^{-4}，外延层组份为 $In_{0.528}Ga_{0.472}As$。2K 温度下 $In_{1-x}Ga_xAs$ 的禁带宽度为：

$E_g=0.4105+0.6337x+0.475x^2$ (eV)

另外，$In_{1-x}Ga_xAs$ 材料因应变引起的带隙变化为 $1.52\Delta a_\perp/a_s$ (eV)；而温度引起的带隙收缩为：

$$-\frac{\alpha T^2}{\beta + T}$$

12

考虑到以上各种因素以后，理论估计(0.803eV)与实验结果符合的相当好．图 6 中在 0.755eV 处的一个很宽的发光峰来自 (D,A)跃迁．
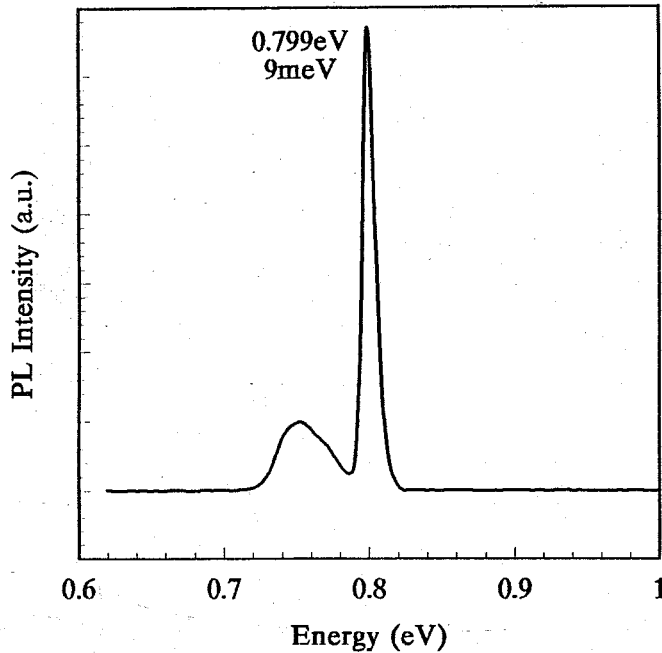
图 6. 30K 下 InGaAs/InP(样品号 B923)的光荧光

3. 量子级联激光器的材料生长

我们利用 Riber 32p 分子束外延设备生长匹配在 n^+ InP 衬底上的 InGaAs/InAlAs 量子级联激光器结构．有源区由 25 级组成，每一级包含 2 个量子阱有源区和一个超晶格注入、/弛豫区．图 7 为完整结构的剖面示意图．整个量子级联激光材料的双晶 X 射线结果示于图 8 , 由图可知整个外延材料的晶格失配度已控制在 10^{-4} 量级．由于顶层光波导的厚度在 2.5μm 以上，波导芯部的晶格质量信息难以突出．为了抽取有源区和注入区(弛豫区)晶格质量的信息，我们单独生长以有源区和注入区(弛豫区)为主的外延材料．图 9(a)和 9(b)分别为材料的结构和双晶 X 射线结果．由图可以看到 20 级以上的卫星峰，表明样品的质量较高．根据所测卫星峰的角间距，可计算出多量子阱的周期．计算结果表明多量子阱的实际周期与设计的周期基本相符．

Graded InGaAs/InAlAs	SL 40nm $7\times10^{18}cm^{-3}$
InAlAs	1250nm $7\times10^{18}cm^{-3}$
InAlAs	350nm $3\times10^{17}cm^{-3}$
InAlAs	300nm $2\times10^{17}cm^{-3}$
Graded InGaAs/InAlAs	SL 30nm $2\times10^{17}cm^{-3}$
InGaAs	300nm $1\times10^{17}cm^{-3}$
End (Active +Injector)	
(Active +Injector)×25	
InGaAs	2.2nm
InAlAs	2.2nm
InGaAs	2.1nm
InAlAs	2.1nm
InGaAs	2.0nm
InAlAs	2.0nm
InGaAs	1.8nm $3\times10^{17}cm^{-3}$
InAlAs	1.8nm $3\times10^{17}cm^{-3}$
InGaAs	1.7nm $3\times10^{17}cm^{-3}$
InAlAs	2.0nm $3\times10^{17}cm^{-3}$
InGaAs	1.6nm $3\times10^{17}cm^{-3}$
InAlAs	2.2nm $3\times10^{17}cm^{-3}$
InGaAs	1.6nm $3\times10^{17}cm^{-3}$
InAlAs	2.4nm
InGaAs	1.4nm
InAlAs	6.8nm
InGaAs	4.8nm
InAlAs	2.8nm
InGaAs	3.9nm
InAlAs	2.7nm
Begin(Active+Injector)	
InGaAs	300nm $1\times10^{17}cm^{-3}$
Graded InGaAs/InAlAs	SL 25nm $2\times10^{17}cm^{-3}$
N^+ InP	

图 7. 整个量子级联激光器结构的剖面图

InGaAs	200nm	2×10^{18}cm^{-3}	
MQW: (Active+Injector)×**20**			
InGaAs	450nm	2×10^{18}cm^{-3}	
InGaAs	30nm		
Semi-insulating	InP		
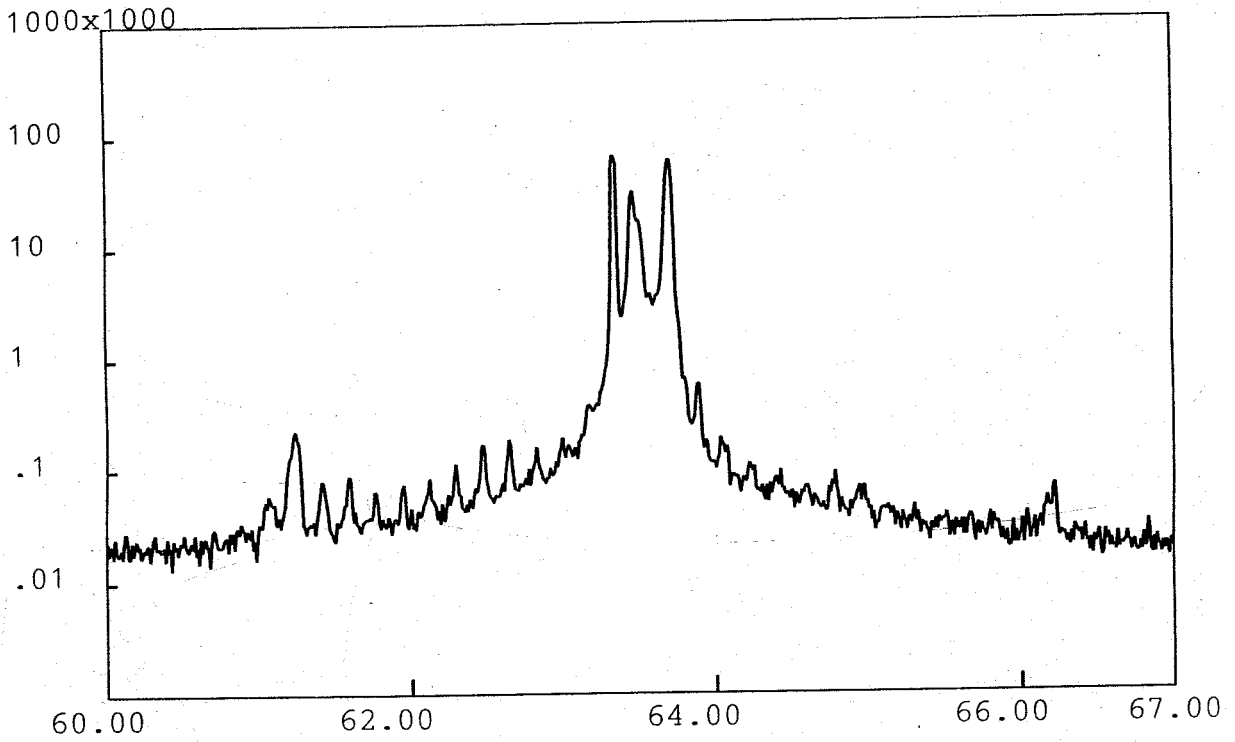
图 9. 由量子级联激光器有源区部分构成的多量子阱结构简图(a)
及材料的双晶 X 射线测试结果(b).

4. 部分器件结果:

将图 7 结构对应的量子级联激光材料制成宽接触器件，低温下的 I-V 曲线结果示于图 10．该结果已接近 Faist[5,6]等人的结果，表明我们的材料质量可靠．进一步的器件测试工作正在进行中．

15
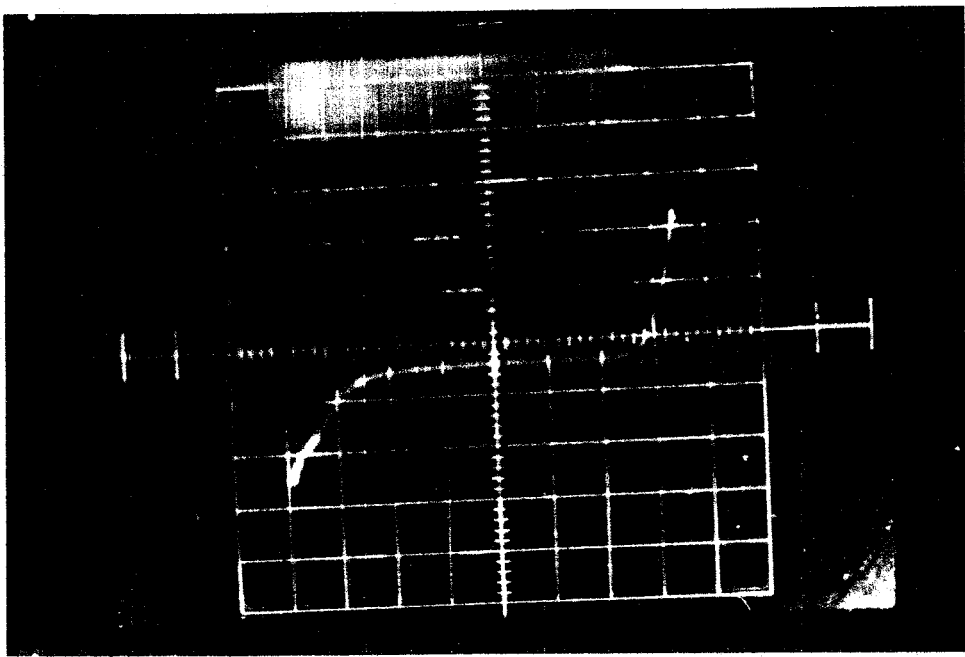
(a) 正向及反向结果: x=2V, y=1mA
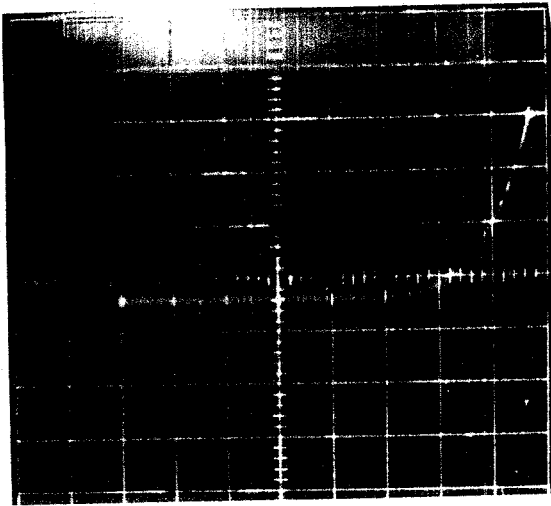
(b) 正向结果: x=1V, y=10mA
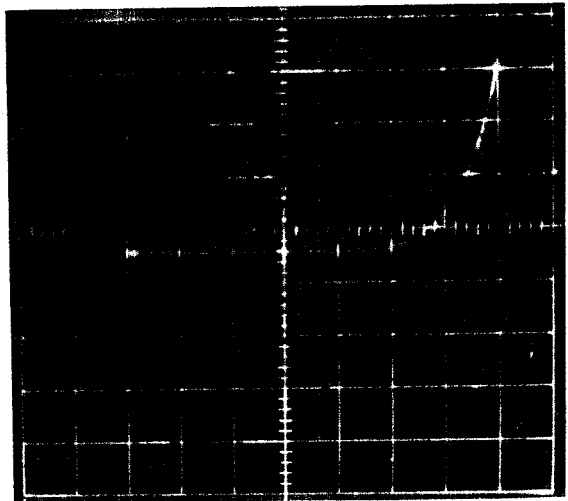
(c) 反向结果: x=1V, y=10mA

图 10 宽接触量子级联激光器 78K 低温下的 I-V 特性:

参考文献

1. 张立纲, 克劳斯·普络格 分子束外延和异质结构(中译本), 复旦大学出版社, 1988 年。

2. H.Hillmer, R.Losch, W.Schlapp, A.Pocker J. Crystal Growth **146**, 159(1995).

3. J.M.Schneider, J.-T.Pietralla, H.Heinecke, J. Crystal Growth **175/176**, 184(1997).

4. J.Faist, F.Capasso, C.Sirtori, D.L.Sivco, A.L.Hutchinson, and A.Y.Cho, Superlattice and Microstructure **19**, 337(1996).

5. J.Faist, F.Capasso, C.Sirtori, D.L.Sivco, A.L.Hutchinson and A.Y.Cho, Appl.Phys.Lett. **67**, 3057(1995).

6. J.Faist, A.Tredicucci, F.Capasso, C.Sirtori, D.L.Sivco, J.N.Baillargeon, A.L.Hutchinson and A.Y.Cho, IEEE J.Quantum Electron.**34**, 336(1998).

InGaAs/InAlAs 耦合量子阱子带间红外吸收
——量子级联激光器的波长定标

用分子束外延技术生长匹配在 InP 衬底上的 InGaAs/InAlAs 量子级联激光材料是一个耗时耗资的高技术工程[1,2]。生长高质量的量子级联激光器材料是研制量子级联激光器的前提，一个最基本的问题是在研制器件之前要大致知道激射波长。只有这样才能做到有的放矢、事半功倍，避免不必要的人力财力浪费。通过对有源区子带间的红外吸收研究可以预先确定波长。

由前面的原理部分的介绍我们知道激光器的激射波长主要由有源区耦合阱的第二和第三能级间距决定。加电场后和不加电场的子带能级间距[3,4]有如下关系：

$$\Delta E(F) = \Delta E_0 \left[1 + \left(\frac{q_e F d}{\Delta E_0} \right)^2 \right]^{\frac{1}{2}} \tag{1}$$

其中ΔE_0和$\Delta E(F)$分别是加场前后子带间距。因此，加场前后子带间距变化不大。

1. 量子级联激光器耦合量子阱有源区材料制备

利用 Riber 32p 分子束外延设备在我所生产的半绝缘 InP 衬底上生长 InGaAs/InAlAs 耦合量子阱结构。样品结构如图 1 所示：B932 有 40 周期，每个周期由三个耦合阱和一个 15nm 厚的隔离势垒组成；B941 有 20 周期，每个周期由双阱耦合区和梯度带隙超晶格区组成。样品 B932 的 X 射线双晶衍射结果示于图 2，由图可以看到多级卫星峰，表明样品的质量较高。根据所测卫星峰的角间距，可计算出耦合量子阱的周期，计算结果表明多量子阱的实际周期与设计的周期基本相符(误差<2%)；而 B941 的 X 射线双晶衍射结果已在前文中给出。将生长后的样品进行 45°机械研磨和抛光，抛光至镜面后进行 FTIR 光吸收测量。

InGaAs　300nm　$1.5 \times 10^{18} \mathrm{cm}^{-3}$
InAlAs　15nm
Repeat Active ×39
End Active
InGaAs　4.0nm
InAlAs　2.2nm
InGaAs　4.7nm
InAlAs　1.5nm
InGaAs　0.9nm
InAlAs　15nm
Begin Active
InGaAs　300nm　$1.5 \times 10^{18} \mathrm{cm}^{-3}$
Semi-insulating　InP

(a)，B932，三阱耦合；

InGaAs	180nm	2×10^{18}cm^{-3}

End (Active +Injector)

(Active +Injector)×20

InGaAs	2.2nm
InAlAs	2.2nm
InGaAs	2.1nm
InAlAs	2.1nm
InGaAs	2.0nm
InAlAs	2.0nm

InGaAs	1.8nm	3×10^{17}cm^{-3}
InAlAs	1.8nm	3×10^{17}cm^{-3}
InGaAs	1.7nm	3×10^{17}cm^{-3}
InAlAs	2.0nm	3×10^{17}cm^{-3}
InGaAs	1.6nm	3×10^{17}cm^{-3}
InAlAs	2.2nm	3×10^{17}cm^{-3}
InGaAs	1.6nm	3×10^{17}cm^{-3}

InAlAs	2.4nm
InGaAs	1.4nm
InAlAs	6.8nm
InGaAs	4.8nm
InAlAs	2.8nm
InGaAs	3.9nm
InAlAs	2.7nm

Begin(Active+Injector)

InGaAs	400nm	2×10^{18}cm^{-3}
InGaAs	30nm	

Semi-insulating InP

(b), B941, 双阱耦合及梯度带隙超晶格。

图1. 红外吸收样品的结构简图:
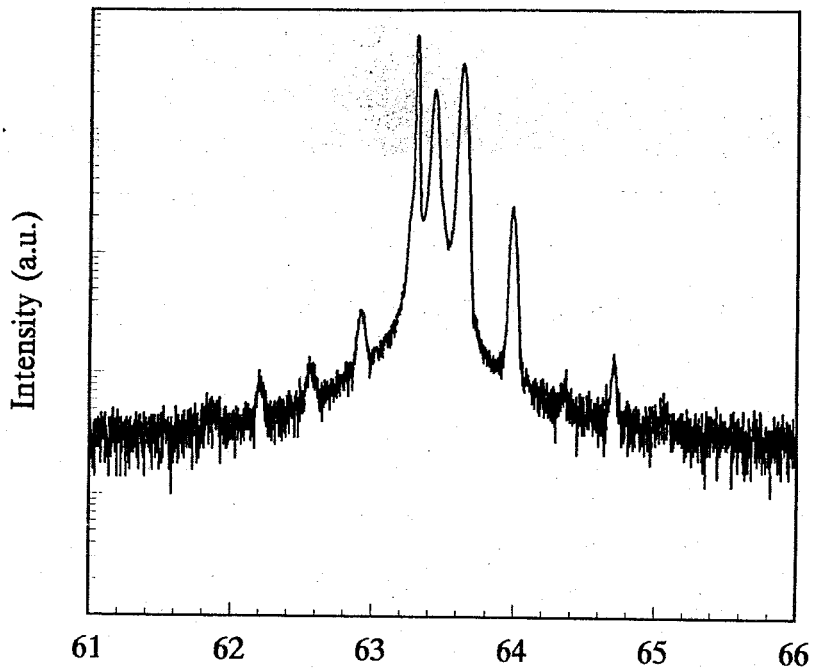
图 2. 样品 B932 的 X 射双晶衍射结果。　　2θ(°)

2. 测试结果及分析

样品 B932 和 B941 的 FTIR 结果分别如图 3、图 4 所示。B932 显示两个子带吸收峰，波长分别为 4μm(0.298eV) 和 5μm(0.241eV)，对应的半高宽分别为 21meV 和 19.6meV。样品 B941 也显示出两个子带吸收峰，波长分别为 4μm(0.3128eV) 和 4.7μm(0.2616eV)，对应的半高宽分别为 16meV 和 13meV。
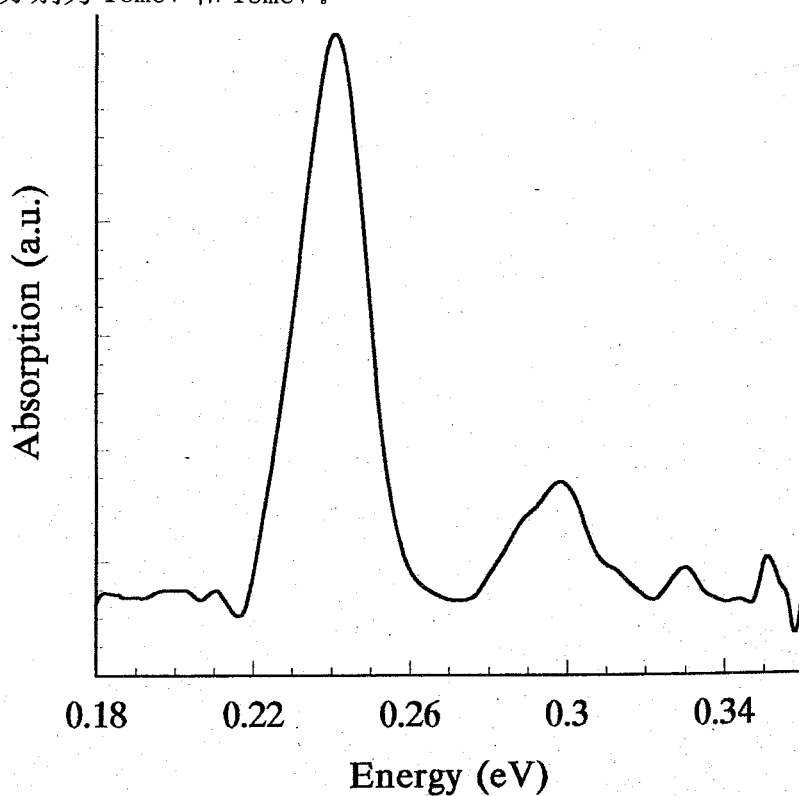
图 3 样品 B932 室温下的子带吸收谱。
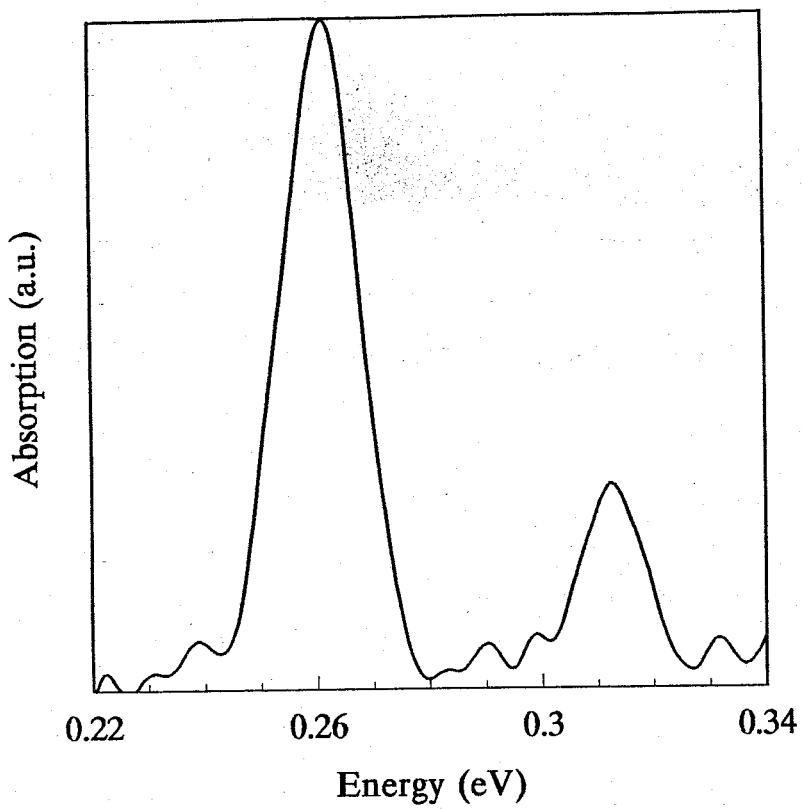
图 4 样品 B941 室温下的子带吸收谱.

为了说明测试结果的正确性，需要与理论设计进行比较．图 5 和图 6 分别是 B932 和 B941 的导带形状示意图及计算得到的子带能级位置．
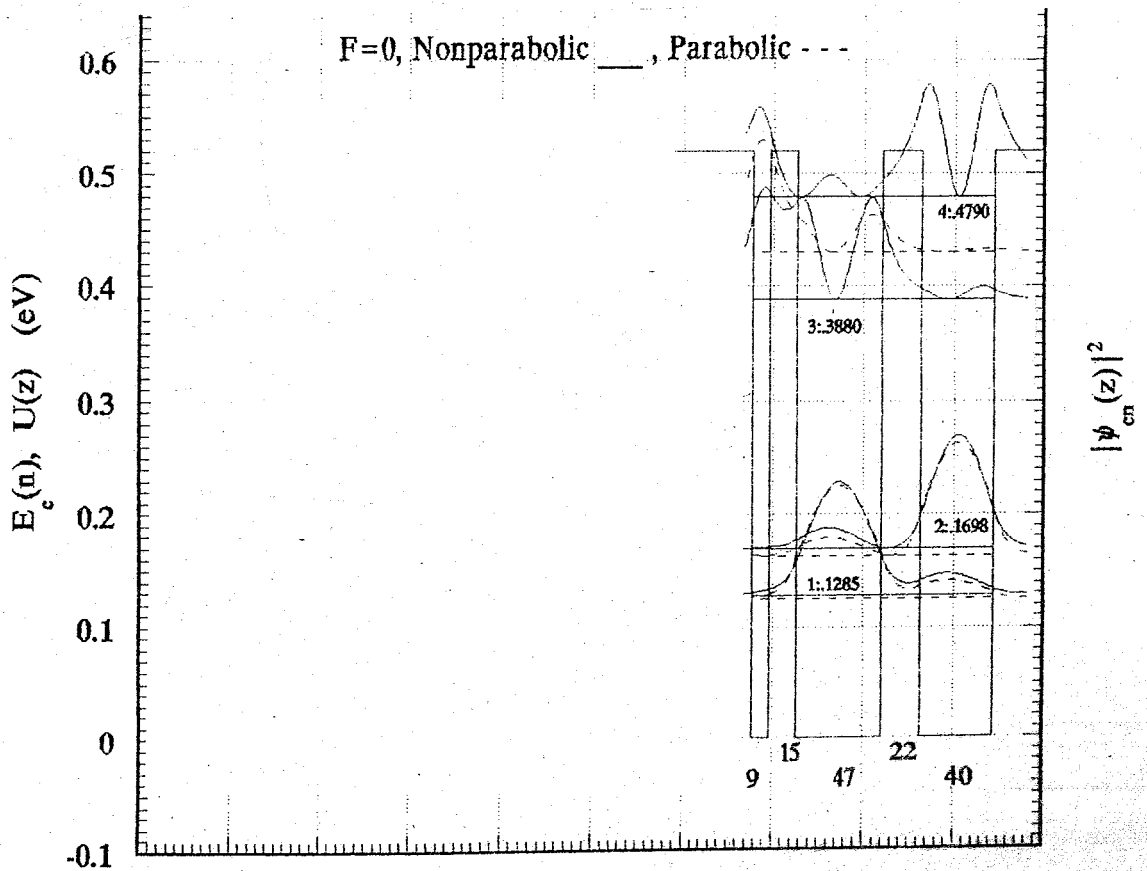
图 5 样品 B932 的导带形状示意图及子带能级位置.
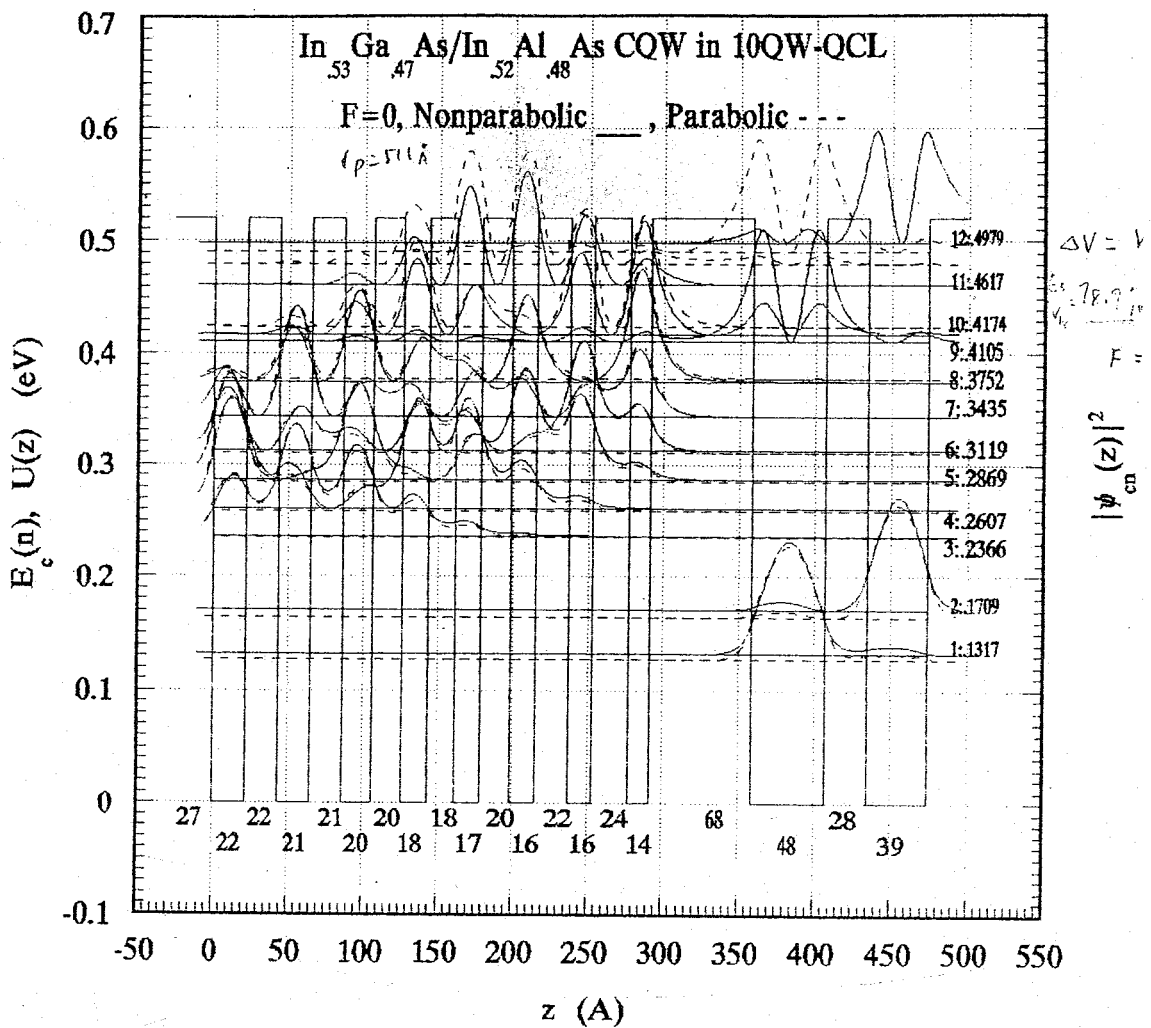
图6 样品 B941 的导带形状示意图及子带能级位置。

  比较图 3 和图 5 可以看出，样品 B932 在 5μm(0.241eV) 处的主吸收峰对应于 1→3 子带跃迁，而 4μm(0.298eV) 处的吸收对应于 2→4 子带跃迁。 5μm(0.241eV) 处的子带吸收正好对应于我们设计激光器的激射波长。同样， 比较图 4 和图 6 可以看出， 样品 B941 在 4.7μm(0.2616eV) 处的主吸收峰对应于图 6 中 1→9 子带跃迁，而 4μm(0.3128eV) 处的吸收对应于图 6 中的 2→12 子带跃迁。我们的结果与 Faist 等人的结果相近[5,6]，但我们测得的子带吸收半高宽均小于 Faist 等人的结果。这表明我们生长的样品质量是十分可靠的。

  我们以样品 B941 为例给出我们的子带能级计算方法。为了简化计算方法， 我们近似地把整个结构当作一个无限超晶格来处理。用 Kronig-Penney 模型[3,4,7] 求解 10 个耦合阱周期结构的 Schrödinger 方程，用顺序的整数标定每个相邻的区域。在阱 n 和垒 n+1 中的波函数可以分别表达为：

$$\phi_n = A_n \cos \alpha x + B_n \sin \alpha x \tag{2}$$

$$\phi_{n+1} = A_{n+1} e^{\beta x} + B_{n+1} e^{-\beta x} \tag{3}$$

阱中波矢α 和垒中波矢β 有如下关系式：

$$\frac{\hbar^2 \alpha^2}{2m_w^*} + \frac{\hbar^2 \beta^2}{2m_b^*} = V_{offsec} \tag{4}$$

21

其中 V_{offset} 是 InGaAs 和 InAlAs 之间的导带带阶。由阱 n 和垒 n+1 的边界条件 ϕ 连续，$(1/m^{*}(z))(d\phi/dz)$ 连续，可以得到一个 2×2 矩阵 $T^{(n)}_{2\times2}$，将系数 A_n，B_n 和 A_{n+1}，B_{n+1} 联系起来，得到以下关系式：

$$\begin{pmatrix} A_{n+1} \\ B_{n+1} \end{pmatrix} = T^{(n)}_{(2\times2)} \begin{pmatrix} A_n \\ B_n \end{pmatrix} \qquad (5)$$

另外，考虑到周期性边界条件

$$\phi_1 = \phi_{21}e^{ik_{SL}L}, \qquad \phi_n = \phi_{n+20}e^{ik_{SL}L} \qquad (6)$$

我们得到：

$$(T^{(20)}_{(2\times2)}T^{(19)}_{(2\times2)}\cdots T^{(1)}_{(2\times2)} - I_{(2\times2)})\begin{pmatrix} A_1 \\ B_1 \end{pmatrix} = 0 \qquad (7)$$

这里 $I_{2\times2}$ 是 2×2 单位矩阵。由下式可以得到波函数的非零解：

$$det(T^{(20)}_{(2\times2)}T^{(19)}_{(2\times2)}\cdots T^{(1)}_{(2\times2)} - I_{(2\times2)}) = 0 \qquad (8)$$

对一个给定超晶格波矢 k_{SL}，行列式通常是 α 的函数，将(8)式的矩阵归一化就可得到本征方程(8)的本征值 α_i，从而得到第 i 个子带的能量本征值和对应的包络波函数。

3. 结论

通过分子束外延技术成功地生长出高质量的量子级联激光器的有源区结构材料。FTIR 测量结果表明存在显著的子带间红外吸收(~5μm)，其波长与设计的结果精确符合，主吸收峰的半高宽均小于 Faist 等人的结果，说明我们生长的材料有很高的可信度，为后续器件的研制打下良好的基础。

参考文献

1. J.Faist, F.Capasso, D.L.Sivco, C.Sirtori, A.L.Hutchinson and A.Y.Cho, Science **264**, 553(1994).

2 J.Faist, A.Tredicucci, F.Capasso, C.Sirtori, D.L.Sivco, J.N.Baillargeon, A.L.Hutchinson and A.Y.Cho, IEEE J.Quantum Electron.**34**, 336(1998).

3 夏建白，朱邦芬，*半导体超晶格物理*，上海科学技术出版社，1995 年.

4. 郭长志、陈水莲，私人通讯.

5. J.Faist, F.Capasso, C.Sirtori, D.L.Sivco, A.L.Hutchinson, S.N.G.Chu, and A.Y.Cho, Appl.Phys.Lett. **65**, 94(1994).

6. J.Faist, F.Capasso, C.Sirtori, D.L.Sivco, A.L.Hutchinson, S.N.G.Chu, and A.Y.Cho, Appl.Phys.Lett. **64**, 1144(1994).

7. G.Bastard, Wave Mechanics Applied to Heterostructures (Les Editions de Physique, Les Ulis, France, 1988).

量子级联激光材料的负微分电阻现象

　　量子级联激光器的有源区由五百多层极薄的 InGaAs 层和 InAlAs 层组成，它的工作原理是子带间的粒子数反转和电子的多级共振隧穿．这要求不同层之间应具有非常清晰的界面[1,2,3]．因此，可以用多级共振隧穿来作为量子级联激光材料的"指纹"认定．

　　在前面的关于量子级联激光器工作原理部分的介绍中我们知道，电子是靠一定宽度的注入微带实现有效注入的，为了研究共振隧穿现象，应该将第一级注入器舍弃．实验样品做成宽接触器件，图 1 是实验样品(编号为 QC2-2)的生长结构剖面图．该样品几个典型的 I-V 测试结果示于图 2．

Graded InGaAs/InAlAs SL 40.8nm		$7\times10^{18}\text{cm}^{-3}$
InAlAs 1250nm	$7\times10^{18}\text{cm}^{-3}$	
InAlAs 350nm	$3\times10^{17}\text{cm}^{-3}$	
InAlAs 300nm	$2\times10^{17}\text{cm}^{-3}$	
Graded InGaAs/InAlAs SL 30nm		$2\times10^{17}\text{cm}^{-3}$
InGaAs 300nm	$1\times10^{17}\text{cm}^{-3}$	
End (Active +Injector)		
(Active +Injector)×15		
InGaAs 1.4nm		
InAlAs 2.4nm		
InGaAs 1.6nm	$3\times10^{17}\text{cm}^{-3}$	
InAlAs 2.2nm	$3\times10^{17}\text{cm}^{-3}$	
InGaAs 1.6nm	$3\times10^{17}\text{cm}^{-3}$	
InAlAs 2.0nm	$3\times10^{17}\text{cm}^{-3}$	
InGaAs 1.7nm	$3\times10^{17}\text{cm}^{-3}$	
InAlAs 1.8nm	$3\times10^{17}\text{cm}^{-3}$	
InGaAs 1.8nm	$3\times10^{17}\text{cm}^{-3}$	
InAlAs 2.0nm		
InGaAs 2.0nm		
InAlAs 2.1nm		
InGaAs 2.1nm		
InAlAs 2.2nm		
InGaAs 2.2nm		
InAlAs 2.7nm		
InGaAs 3.9nm		
InAlAs 2.8nm		
InGaAs 4.8nm		
InAlAs 6.8nm		
Begin Active		
InGaAs 300nm	$1\times10^{17}\text{cm}^{-3}$	
Graded InGaAs/InAlAs SL 25nm		$2\times10^{17}\text{cm}^{-3}$

　　N^+ InP

图 1 QC2-2 样品的生长结构剖面简图
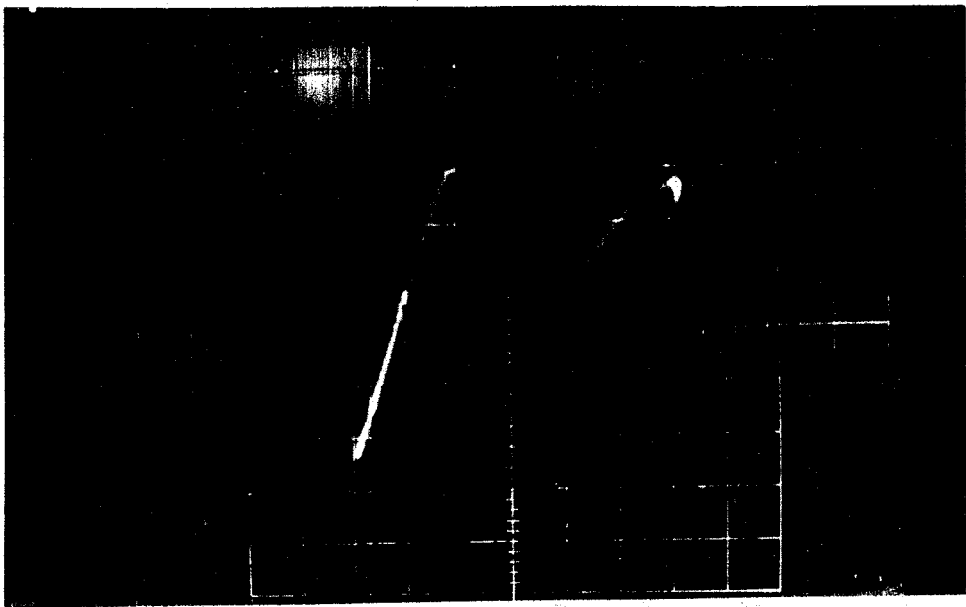
(a) 293K: x=0.5V/格, y=50mA/格
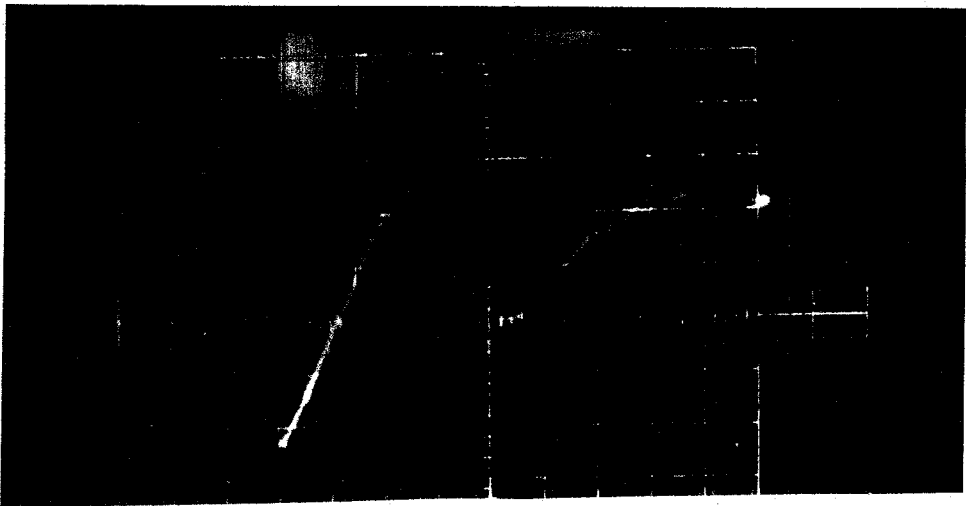
(b) 243K: x=0.5V/格, y=50mA/格
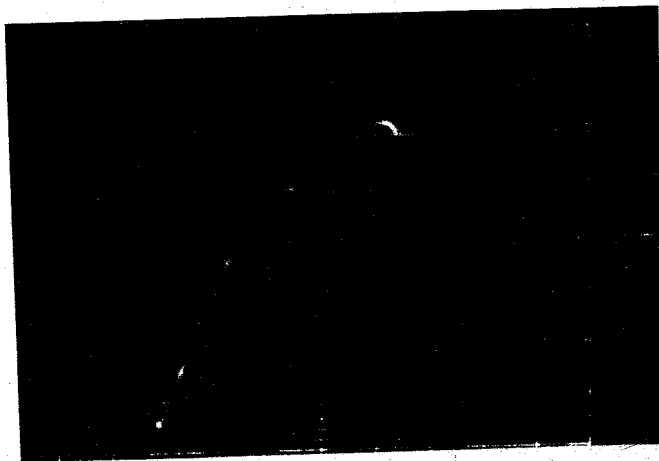
(c) 175K: x=0.5V/格, y=100mA/格

24
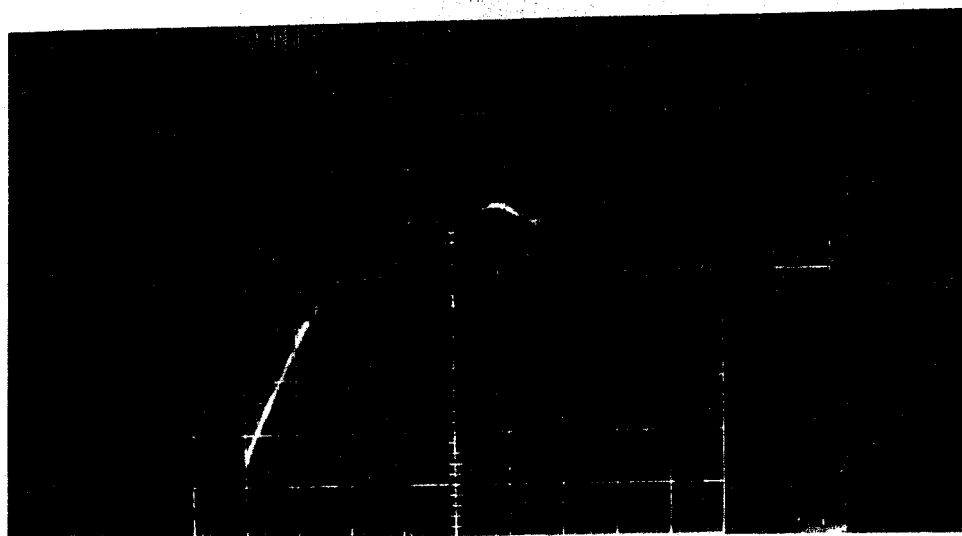
(d) 293K： x=0.5V/格， y=100mA/格

图 2 不同温度下 QC2-2 样品几个典型的 I-V 测试结果:。

  由图 2 的 I-V 测试结果可以看出显著的负微分电阻现象，表明不同层之间具有清晰的界面。由于该结构十分复杂，定量计算还很困难。由于时间关系，对该结果的细节的理解还不明了。特别是低温下的负阻现象更加奇特，我们将在以后的工作中作进一步的探究。

参考文献

1. F.Capasso, S.Sen, F.Belram, L.Lunadri, A.Vengurlekar, P.R.Smith, N.J.Shah, R.Malik, and A.Y.Cho, IEEE Trans. Electron Devices, **36**, 2065(1989).

2. F.Capasso, K.Mohammed, and A.Y.Cho, IEEE J.Quantum Electron, **22**, 1853(1986).

3. F.Capasso and Datta, Physics Today(Feb.), 74(1990).

Photoluminescence of strained InGaAs/InAlAs single quantum wells

Feng-Qi Liu[a] , Zhan-Guo Wang, Bo Xu, Qian Gong, Quan-Sheng Zhang, Ji-Ben Liang

Laboratory of semiconductor materials science, Institute of semiconductors,

Chinese Academy of Sciences, P. O. Box 912, Beijing 100083, China

Abstract

Photoluminescence measurements have been performed on $In_{0.6}Ga_{0.4}As$ /$In_{0.52}Al_{0.48}As$ and $In_{0.46}Ga_{0.54}As/In_{0.52}Al_{0.48}As$ strained single quantum wells with well widths each of 16 monolayers and 3monolayers. The strained single quantum wells were grown side-by-side with corresponding lattice matched $In_{0.53}Ga_{0.47}As/In_{0.52}Al_{0.48}As$ single quantum wells on a InP substrate by molecular beam epitaxy. Conspicuous photoluminescence peak shifts due to strain are observed for 16monolayers single quantum wells, and the emission energies are in agreement with the theoretical expected excitonic peak energies. To our surprise, luminescence from 3 monolayers triplet single quantum wells shows only a single peak. This phenomenon appears to arise from the energy gap increment of $In_{0.6}Ga_{0.4}As$ well due to the enhanced random alloy disorder and possibly the formation of quantum plates on the one hand, and the energy gap shrinkage of $In_{0.46}Ga_{0.54}As$ due to the presence of CuPt-type ordering on the other hand.

PACS: 78.66Fd, 78.55.Cr, 68.65.+g

---

[a] To whom correspondence should be addressed. E-mail: fqliu@red.semi.ac.cn

I. INTRODUCTION

Recently, InGaAs/InAlAs quantum wells have received considerable attention for the potential applications in the field of long wavelength optoelectronic devices, ultrahigh-speed microelectronic devices and infrared detectors[1-3], thanks to the large conduction band discontinuity at the interfaces and the significant band nonparabolicity in the InGaAs quantum wells. A typical provoking breakthrough of the applications started with the successful growth of InGaAs/InAlAs quantum cascade lasers which based on one type of carrier (elecrons) between energy levels created by quantum confinement[4,5]. A crucial aspect for the device application of these quantum wells is the layer quality and the abruptness of interfaces. Consequently, the unavoidable problems are alloy disorder and strain due to the lattice mismatch. However, strained-layer structures of high crystalline quality can be fabricated on condition that the layer thicknesses do not exceed certain critical values[6].An introduction of strain in the InGaAs well from the lattice-matched composition can dramatically alter the energy band structure and thereby the optical properties. Strained quantum wells have opened rich perspectives for the low threshould current diode lasers[7] and high-electron-mobility transistor devices with high cut-off frequency[8]. These brilliant achievements have been inspiring us to explore the possible applications of strained quantum wells in other advanced optoelectronic devices such as quantum cascade lasers. However, there have been relatively few reports of the optical studies of strained InGaAs/InAlAs quantum wells narrower than 5nm.

This paper presents photoluminescence (PL) studies of narrow InGaAs/InAlAs strained single quantum wells (SQWs) grown side-by-side with the corresponding lattice matched SQW by solid-source molecular beam epitaxy (MBE). Good crystal quality in the strained SQWs has been confirmed by the sharp PL spectra. In addition, conspicuous PL energy shifts due to strain were observed for 16 monolayers (MLs) SQWs. However, contrary to our expections, still pronounced but a single PL spectrum emerged for the compressive-strained, lattice-matched, and tensile-strained narrow 3MLs SQW. This PL mergence feature can be attributed to the surfaced-induced CuPt-type ordering of tensile strained SQW and the enhanced alloy disorder at the interfaces of the compressive strained SQW.

II. EXPERIMENT

16 and 3MLs of $In_{0.6}Ga_{0.4}As$ /$In_{0.52}Al_{0.48}As$ and $In_{0.46}Ga_{0.54}As$/$In_{0.52}Al_{0.48}As$ SQWs were grown side-by-side with corresponding lattice matched $In_{0.53}Ga_{0.47}As$/$In_{0.52}Al_{0.48}As$ SQW sequentially according to the indiction of Fig. 1 on a (100) semi-insulating Fe-doped InP susbtrate in a Riber 32p MBE system. This geometric structure ensures us a *direct comparison* of the optical properties between latice-matched and strained SQWs. The growth temperature was measured by a thermocouple and referenced to the (2×4) to (4×2) suface reconstruction transition of the InP substrate. This transition was assumed to occur at 520°C under an As_4 beam equivalent pressure of 1×10^{-5} Torr. The V/III beam equivalent pressure ratio amounted to 14. The sample was grown at a substrate temperature of 500°C with growth rates of 0.62 and 0.644μm/h for InGaAs and InAlAs, respectively. The lattice mismatch, with respect to an InP substrate, was determined by double-crystal x-ray diffraction measurements. PL measurements were performed on a IFS120 HR fourier transform infrared spectrameter at various temperatures with the sample cooled in a closed-cycle He cryostat. The 514.5 nm line of an Ar-ion laser was used as the excitation source and photomultiplier and InGaAs detector were employed to record the spectra. The output power of the laser was about 50mW which corresponds to approximately 0.5W/cm^2. The optical measurements were made at the resolution of 5cm^{-1}.

III. RESULTS AND DISCUSSION

Fig. 2 shows the infrared PL spectra from lattice-matched and strained InGaAs/InAlAs narrow SQWs. Two characteristic features can be derived. (i) 16MLs $In_{0.6}Ga_{0.4}As/In_{0.52}Al_{0.48}As$, $In_{0.6}Ga_{0.4}As/In_{0.52}Al_{0.48}As$, and $In_{0.46}Ga_{0.54}As/In_{0.52}Al_{0.48}As$ SQW exhibits distinctively a triplicate strong PL, and these PL energies coincide with the heavy hole excitonic peak energies calculated by a finite square-well model including the effect due to the band nonparabolicity and the effects due to the revisions of composition and strain. In addition, the energy shifts of strained SQWs relative to the lattice-matched SQW are larger than expected for a variation of the well thickness by 1 ML at low temperature. The PL line width (FWHM, full width at half maximum) at 15K of $In_{0.6}Ga_{0.4}As/In_{0.52}Al_{0.48}As$ (13meV) and $In_{0.46}Ga_{0.54}As/In_{0.52}Al_{0.48}As$ (10meV) are narrower than that of $In_{0.53}Ga_{0.47}As/In_{0.52}Al_{0.48}As$ (14meV). The emission from the lattice-matched $In_{0.53}Ga_{0.47}As/In_{0.52}Al_{0.48}As$ SQW is somewhat broader, possibly stems from substrate misorientation[9]. (ii) Instead of a triplicate PL peak, compressive-strained, lattice-matched, and tensile-strained narrow 3MLs SQWs only exhibit a single PL peak. The FWHM of this merged-peak at 15K is 24meV. Figure 3 presents how the PL peak energies and the corresponding FWHM vary with temperature. Within the temperature range from 15 to 100K, the PL peak energies correspond to 16MLs SQWs almost unchanged, while the corresponding FWHM linearly increase by 0.82meV/K (a rate of approximately kT). This is a proof of good crystal quality of 16MLs SQWs. In the same temperature range, the PL merged-peak energy of 3MLs SQWs linearly decreases by 0.47meV/K (a rate slightly greater than the bulk band-gap shrinkage rate), while the corresponding FWHM linearly increases by 0.6meV/K. The emission broadening originates from two possible aspects, i.e, the variations in the well thickness and random alloy disorder. The expected broadening of the quantum well resulting from islands with a height of one monolayer and a lateral radius comparable to the exciton radius are 15 and 55meV at 15K for 16 and 3MLs SQW, respectively, which are larger than the experimental values at 15K. This leads to the conclusion that the hetero-interfaces must be of high quality and the lateral dimensions of the islands (if exist) must be smaller than the exciton radius. The effect of random alloy variation in InGaAs on the luminescence broadening can be rougtly estimated by[10]

$$\Delta E = 2.36 \frac{dE_g}{dx} \left(\frac{x(1-x)}{k\pi \left(\frac{\varepsilon_r}{m_r/m_0} a_B \right)^2 L_z} \right)^{1/2} \tag{1}$$

$$k = a_0^{-3}$$

where ε_r is the dielectric constant, m_r is the reduced effective mass, a_B is the Bohr radius, L_z is the quantum well thickness, x is the composition, and a_0 is the lattice constant, the peak brodenings due to random alloy variation in InGaAs are about 7 and 15meV for 16 and 3MLs SQWs, respectively.

In order to elucidate the experimental results, the theoretical depiction is necessary. The two-dimensional heavy hole excitonic transition energy is given by

$$\hbar\omega = E_g + E_e + E_h - E_b \tag{2}$$

Where E_e and E_h are the confinement energies of the electrons and holes, respectively, E_b is the two-dimensional exciton binding energy, and, E_g is the three dimensional effect band gap of InGaAs at the temperature T, which is given by

$$E_g = E_g^0 + \Delta E - \frac{\alpha T^2}{\beta + T} \qquad (3)$$

Where E_g^0 is the composition-dependent band gap of unstrained $In_xGa_{1-x}As$ at 2K, and can be deduced from[11]

$$E_g^0(x) = 1.5192 - 1.5837x + 0.475x^2 \qquad (4)$$

consequently, we obtain 0.813, 0.736, and 0.892eV at 2K for $In_{0.53}Ga_{0.47}As$, $In_{0.6}Ga_{0.4}As$, and $In_{0.46}Ga_{0.54}As$, respectively. ΔE is the energy shift due to strain. It is assumed to depend linearly on the biaxial strain, ε, according to[12]

$$\Delta E = [-2a(c_{11} - c_{12})/c_{11} + b(c_{11} + 2c_{12})/c_{11}]\varepsilon \qquad (5)$$

a and b being the hydrostatic and shear stress deformation potentials, respectively, and c_{ij} the elastic stiffness coefficients. The third term in Eq.(3) accounts for the band-gap dependence on the temperature. In our calculation, the parameters are gathered in Table I. The alloy parameters are interpolated from the values corresponding to the binaries. The confinement energy levels within the wells for electrons and heavy holes can be calculated using the finite square potential well model[14]. Nonporabolicity is included in both well and barrier layers through the expression $m(E)=m^*(1+2\alpha E)$. The effective masses of electrons and heavy holes used for InGaAs are $m_e(E)=0.043m_0(1+2\times1.13E)$ and $m_h(E)=0.38m_0(1+2\times0.387E)$, respectively; while for InAlAs are $m_e(E)=0.078m_0(1+2\times0.582E)$ and $m_h(E)=0.57m_0(1+2\times0.027E)$, respectively[15]. The 2K low-temperature band gap energy of $In_{0.52}Al_{0.48}As$ barrier is taken to be 1.511eV[16]. ΔE_c at 2k is 0.52eV for lattice-matched heterostructures corresponding to the conduction band offset ratio 74.5%, and assuming this ratio is endorsed by strained SQWs. The theoretical predictions and the experimental results at 15K are summarized in Table II. The 15K PL peak energies of 16MLs SQWs of $In_{0.6}Ga_{0.4}As/In_{0.52}Al_{0.48}As$, $In_{0.53}Ga_{0.47}As/In_{0.52}Al_{0.48}As$ and $In_{0.46}Ga_{0.54}As/In_{0.52}Al_{0.48}As$ are 0.943, 0.968, and 1.000eV, respectively, which are higher than the corresponding calculated values. This discrepancy is, however, understandable taking into account the uncertainty of the valance-band offset, deformation potentials, and valance-band masses used in the calculation.

The experimental results for the 3MLs SQWs are exceed our expectations. The PL peaks of 3MLs $In_{0.6}Ga_{0.4}As/In_{0.52}Al_{0.48}As$, $In_{0.53}Ga_{0.47}As/In_{0.52}Al_{0.48}As$ and $In_{0.46}Ga_{0.54}As/In_{0.52}Al_{0.48}As$ SQWs contract into a single, indicting that a change in composition of a few percent has no significant effect on the emission energy of 3MLs SQW. But the theoretical estimation of PL peak energy difference between 3MLs $In_{0.6}Ga_{0.4}As/In_{0.52}Al_{0.48}As$ and $In_{0.46}Ga_{0.54}As/In_{0.52}Al_{0.48}As$ SQWs at low temperature is about 39meV. What is the origin of the PL peak contraction of 3MLs SQWs ? The PL peak mergence indicates that the luminescence energies of compressive-strained, lattice-matched and tensile-strained 3MLs SQW are nearly equal. We can rationally assumed that the emission energy of the compressive-strained 3MLs SQW presents a blue shift, and simultaneously the emission energy of tensile-strained 3MLs SQW give a red shift. Two aspects account for this feature, the energy gap increment of $In_{0.6}Ga_{0.4}As$ well due to the enhanced random alloy disorder and possible the formation of quantum plates at the interfaces on the one hand, and the energy gap shrinkage of $In_{0.46}Ga_{0.54}As$ well due to the presence of CuPt-type ordering on the other hand. This picture can be explained as follows. (i) The undulated growth front and fuzzy boundary of barriers enhance the surface roughning of compressive-strained $In_{0.6}Ga_{0.4}As$ layer, and thus provides possible nucleation sites for

"islanding"[17]. This contributes to the formation of disk-like morphology, and maybe the quantum plates are formed. In addition, strain-assisted interface segregations of the compositions can increase the degree of disorder to some extent. Just like the energy band of amorphous silicon is larger than the band gap of crystalline silicon, this enhanced disorder of the interfaces will increase the energy gap more or less. Consequently, quantum plates coexist with the enhanced disorder cause the PL line blue shift of compressive strained 3MLs SQW. (ii) The PL line red shift of the 3MLs $In_{0.46}Ga_{0.54}As/In_{0.52}Al_{0.48}As$ SQW possibly correlates with the presence of strong CuPt-type ordering. The CuPt-type ordering is a surface related phonomenon occuring during the layer growth, and is energetically more stable at the layer interfaces than any other kind of ordering or the disordered state[18]. Calculations have predicted that CuPt-type ordering can produce significant decreases in the band-gap energy[19] and experimental measurements have proved this to be the case for $In_xGa_{1-x}As$ layers[20,21] grown on (100) InP substrate. This ordering is preferable to occuring at the tensile-strained and lattice-matched layer interfaces[22]. The amount of ordering present in the layer was controled by the two competing processes, namely, ordering occuring initially at the growing interfaces and disorder occuring subsequently in a transition region. The surface undulations of the barrier layers and the InGaAs well layer will provide a wide range of surface configurations, and the segregation of InAs at the steps will play an auxiliary role of the formation of ordering. This sublattice ordering is also suggested by noting the broader FWHM of PL[23], which is one characteristic feature of ordered material. The broader PL line width arises from the presence of potential fluctuations due to sublattice ordering. Thus the red shift of PL line can be explained if one assumes that the $In_{0.46}Ga_{0.54}As$ layer is a mixture of ordered and random (disordered) alloy domains. According the Wei *et al.*[24], the ordernig induced band-gap change is given by

$$B(\eta) = [\Delta E_g(1,0) + \frac{1}{3}\Delta_{111}^o(1,0)]\eta^2$$

where $\Delta E_g(1,0)$ is the band gap reduction of the strain-free and fully order alloy relative to the perfectly random alloy, η is the CuPt-type order parameter, and Δ_{111}^o is the valance band lift due to ordering-induced crystal field splitting. We can roughly estimate the band gap shrinkage based on the band structure values calculated for $In_{0.5}Ga_{0.5}As$ by Wei *et al.*,[25] i.e., Δ_{111}^o =0.1eV and $\Delta E_g(1,0)$=−0.3eV. According to Table II, $B(\eta)$ is taken to be 0.029eV, and we obtain η=0.33. It is necessary to point out that the above mentioned interface-related feature have no valid effect on 16MLs strained SQWs because of the small interfacial ratio.

The temperature dependence of the PL intensities indicating the presence of nonradiative recombination mechanisms. This thermal quenching mechanism of luminescence in SQW structure can be attributed to thermal activated detraping of carriers from the wells into barriers, followed by nonradiative recombination in the barriers[26,27]. To quantitative analyze the experimental data is laborious due to so many arbitrary adjustable parameters. The red shift due to the temperature increases from 15 to 100K for 3MLs SQWs is larger than the corresponding band-gap decrease of InGaAs bulk material. At present, we have no sound explanation for the additional temperature-related red shift of PL peaks.

IV. SUMMARY

In conclusion, PL measurements have been performed on $In_{0.6}Ga_{0.4}As /In_{0.52}Al_{0.48}As$ and $In_{0.46}Ga_{0.54}As/In_{0.52}Al_{0.48}As$ strained single quantum wells with well widths each of 16 and 3MLs grown side-by-side with the corresponding lattice matched $In_{0.53}Ga_{0.47}As/In_{0.52}Al_{0.48}As$

single quantum wells on a InP substrate by MBE. Apparent PL peak shifts due to strain are observed for 16MLs strained SQWs, and the emission energies can be attributed to excitonic peak energies. Out of our expections, luminescence from 3MLs triplet SQWs shows only a single peak. Two aspects account for this phenomenon, one aspect is the energy gap increment of $In_{0.6}Ga_{0.4}As$ well due to the enhanced random alloy disorder and possibly the formation of quantum plates, the other aspect is the energy gap shrinkage of $In_{0.46}Ga_{0.54}As$ due to the presence of CuPt-type ordering. This little dependence of energy band on the strain in very thin quantum wells will find important implications for device applications, giving a new opportunity for quantum cascade lasers.

ACKNOWLEDGEMENTS

References

1. H.Temkin, K.Alavi, W.R.Wagner, T.P.Pearsall, and A.Y.Cho, Appl.Phys.Lett.**42**, 845(1983).
2. B.F.Levine, A.Y.Cho, J.Walker, R.J.Malik, D.A.Kleinman, and D.L.Sivco, Appl.Phys.Lett.**52**, 1481(1988).
3. V.Drouot, M.Gendry, C.Santinelli, X.Letratre, J.Tardy, P.Viktorovitch, G.Hollinger, M.Ambri, and M.Pitaval, IEEE Trans.Electron Devices **43**, 1326(1996).
4. J.Faist, F.Capasso, D.L.Sivco, C.Sirtori, A.L.Hutchinson, and A.Y.Cho, Science **264**, 553(1994).
5. J.Faist, F.Capasso, C.Sirtori, D.L.Sivco, A.L.Hutchinson, M.S.Hybertsen, and A.Y.Cho, Phys.Rev.Lett. **76**, 411(1996).
6. G.Ji, D.Huang, O.K.Reddy, T.S.Henderson, R.Houdre, and H.Morkoç J.Appl.Phys.**62**, 3366(1987).
7. A.Mathur, P.D.Dapkus, IEEE J.Quantum Electronics **32**, 222(1996).
8. G.I.Ng, D.Pavlidis, M.Jaffe, J.Singh, and H.F.Chau, IEEE Trans. Electron Devices **ED-36**, 2249(1989).
9. J.R.Botha and A.W.R.Leitch, Mater.Sci.Forum **143-147**, 635(1994).
10. E.F.Schubert, E.O.Gobel, Y.Horikoshi, K.Ploog, and H.J.Queisser, Phys.Rev.B**30**, 813(1984).
11. K.M.Geotz and D.Bimberg, J.Appl.Phys.**54**, 4543(1983).
12. H.Asai and K.Oe, J.Appl.Phys.**54**, 2052(1983).
13. J.M.Gilp—rez et al., J.Appl.Phys.**76**, 5931(1994).
14. D.B.Tran Thoai, R.Zimmermann, M.Grundmann, and D.Bimberg, Phys.Rev.B**42**, 5906(1990).
15. The effective masses and nonparabolicity values are obtained from Ref.5; and W.Stolz et al., Phys.Rev.B**36**, 4310(1987); and J.S.A.Adelabu et al., Semicond.Technol.**4**,677(1989).
16. D.Oertel, D.Bimberg, R.K.Bauer, and K.W.Carely, Appl.Phys.Lett.**55**, 140(1989).
17. R.N¬tzel, J.Temmyo, and T.Tamamura, Nature **369**, 131(1994).
18. T.Kanata, M.Nishimoto, H.Nakayama, and T.Nishino, Phys.Rev.B**45**, 6637(1992).
19. S.Froyen, and A.Zunger, Phys.Rev.Lett.**66**, 2132(1991).
20. D.J.Arent, M.Bode, K.A.Bertness, S.R.Kurtz, and J.M.Olson, Appl.Phys.Lett.**62**, 1806(1993).
21. J.-W.Lee, A.T.Schremer, D.Fekete, and J.M.Ballantyne, Appl.Phys.Lett.**70**, 756(1997).
22. C.Geng, M.Moser, R.Winterhoff, E.Lux, J.Hommel, B.Hohing, and H.Schweizer, J.Cryst.Growth **145**,740(1994).
23. R.P.Schneider, Jr., E.D.Jones, J.A.Lott, and R.P.Bryan, J.Appl.Phys.**72**, 5397(1992).
24. S.-H.Wei and A.Zunger, Appl.Phys.Lett.**64**, 757(1994).
25. S.-H.Wei, D.B.Laks, and A.Zunger, Appl.Phys.Lett.**62**, 1937(1993).
26. J.R.Botha and A.W.R.Leith, Phys.Rev.B**50**, 18147(1994).
27. E.M.Daly, T.J.Glynn, J.D.Lambkin, L.Considine and S.Walsh, Phys.Rev.B**52**, 4696(1995).

TABLE I. InGaAs parameters used in the calculation of energy shift due to strain. α and β are obtained from Ref[13].

Materials	a(eV)	b(eV)	$c_{11}(10^{11}\text{dyn/cm}^{-1})$	$c_{12}(10^{11}\text{dyn/cm}^{-2})$	$\alpha\,(10^{-4}\text{eV/K})$	β (K)
$In_{0.46}Ga_{0.54}As$	-7.41	-1.75	10.25	4.99	4.07	227
$In_{0.6}Ga_{0.4}As$	-7.01	-1.76	9.74	4.87	3.65	235
$In_{0.53}Ga_{0.47}As$					3.86	231

TABLE II. Comparison of the experimental PL energies (in eV unit) at 15K and the theoretical results.

well width	$In_{0.6}Ga_{0.4}As$		$In_{0.53}Ga_{0.47}As$		$In_{0.46}Ga_{0.54}As$	
	exp.	theory	exp.	theory	exp.	theory
16MLs	0.943	0.914	0.968	0.954	1.000	0.990
3MLs		1.341	1.351	1.347		1.380

Figure captions

Figure 1.   Schematic cross section of the complete InGaAs/InAlAs single qwantum wells structure.

Figure 2.   Photoluminescence spectra of 16 and 3MLs SQWs at different temperature.

Figure 3.   (a) PL peak energy versus the sample temperature. Crosses, dots, and triangles are measured data of compressive-strained, lattice-matched, and tensile-strained 16MLs SQW, respectively; circles are measured data of 3MLs SQWs. (b) PL peak FWHM versus the sample temperature.

$In_{0.53}Ga_{0.47}As$ 10nm
InAlAs 150nm
$In_{0.6}Ga_{0.4}As$ 3MLs
InAlAs 25nm
$In_{0.6}Ga_{0.4}As$ 16MLs
InAlAs 40nm
$In_{0.46}Ga_{0.54}As$ 3MLs
InAlAs 25nm
$In_{0.46}Ga_{0.54}As$ 16MLs
InAlAs 40nm
$In_{0.53}Ga_{0.47}As$ 3MLs
InAlAs 25nm
$In_{0.53}Ga_{0.47}As$ 16MLs
InAlAs 350nm
InP substrate
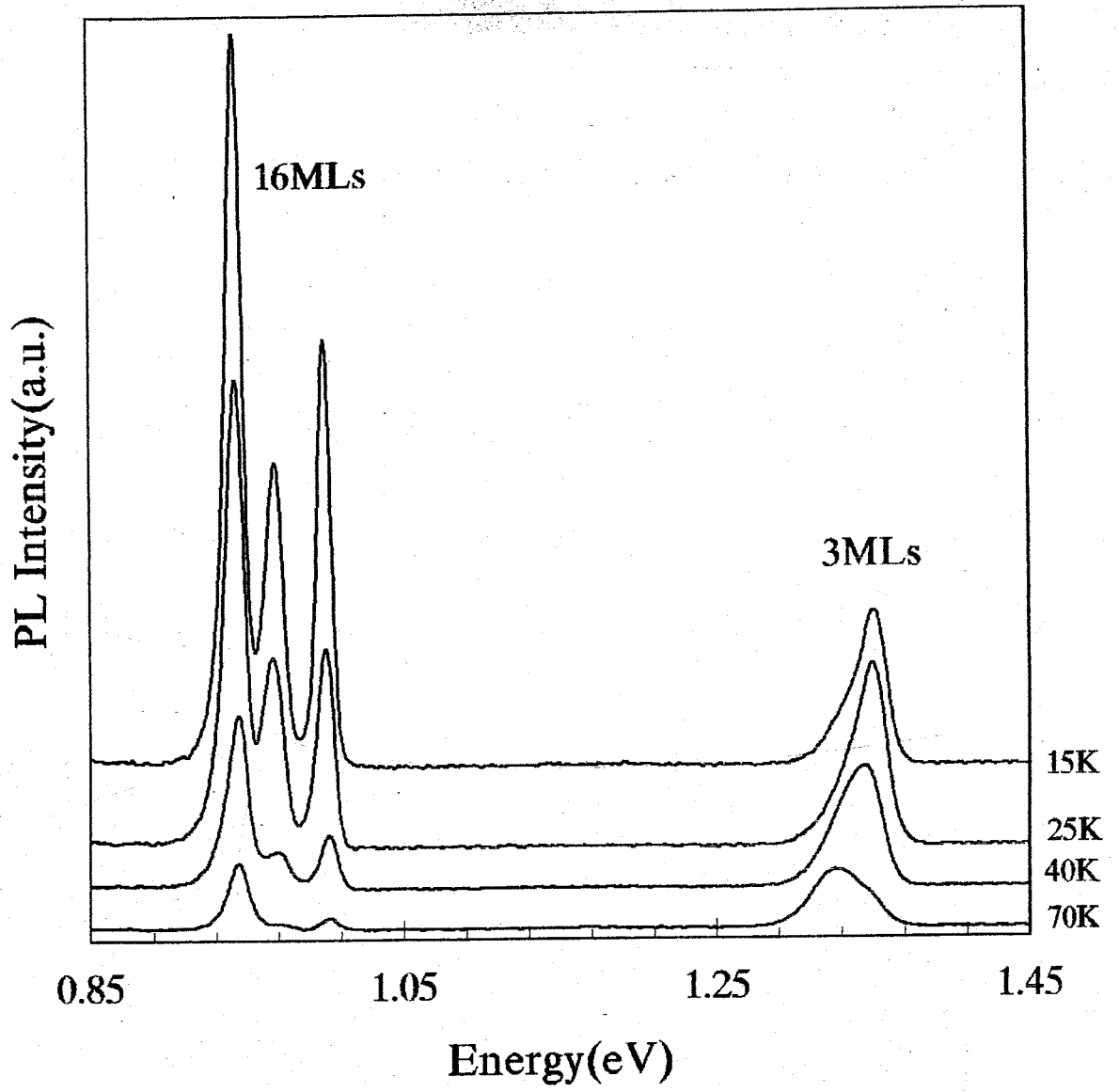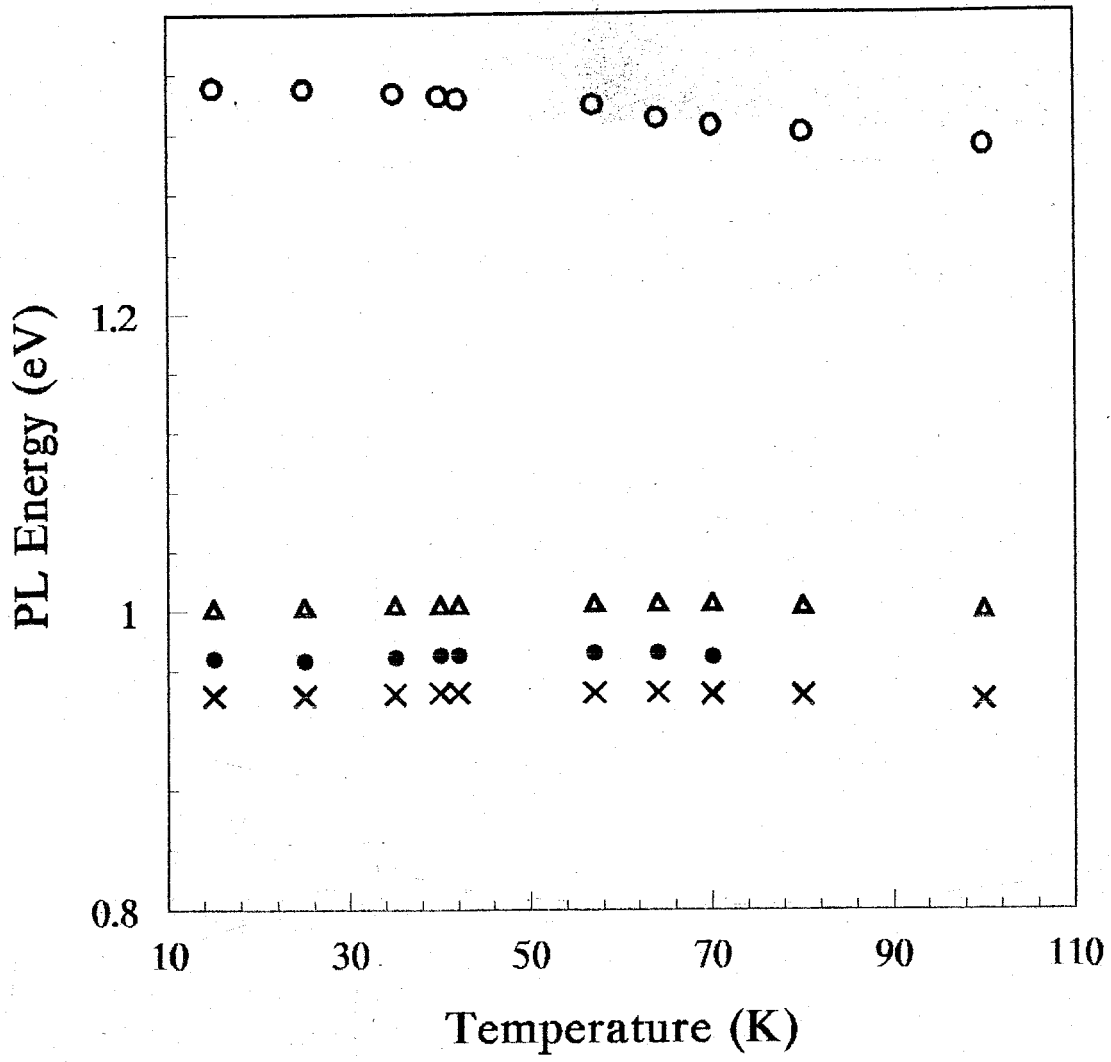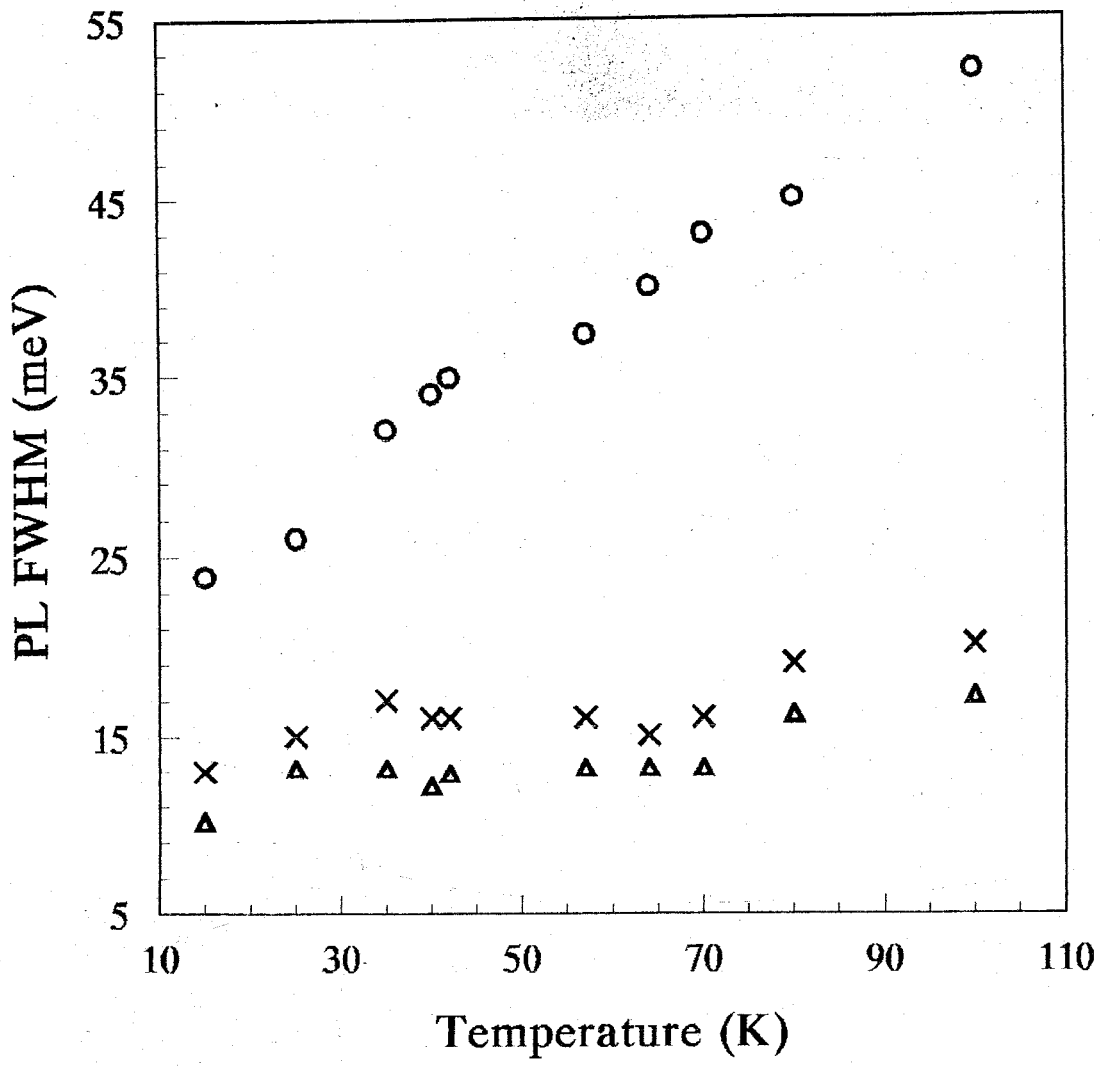
Structure and photoluminescence of InGaAs self-assembled quantum dots grown on InP(001)

Feng-Qi Liu[a] , Zhan-Guo Wang, Ju Wu, Bo Xu, Qian Gong, and Ji-Ben Liang

Laboratory of semiconductor materials science, Institute of semiconductors,

Chinese Academy of Sciences, P. O. Box 912, Beijing 100083, China

Abstract

Molecular beam epitaxy has been used for growing InGaAs self-assembled quantum dots (QDs) in InAlAs on an InP(001) substrate. Nominal deposition of 9.6 monolayers (ML) of $In_{0.9}Ga_{0.1}As$ resluts in QDs of ~6.5nm high with areal density of $3.3 \times 10^{11} cm^{-2}$. Conspicuous bimodal size distribution is identified, and is responsible for the observed QDs photoluminescence (PL) emission with two peaks at 0.627 and 0.657eV. Good agreement is achieved between the observed PL peak energies and calculated results.

PACS: 78.55.Cr,   78.66.Fd,   68.65.+g

---

[a] To whom correspondence should be addressed. E-mail: fqliu@red.semi.ac.cn

Self-assembled quantum dots (QDs) have been generated a great deal of scientific and technological interest, promising new applications like single electron transistors[1] and lasers[2] with improved performance. Various QD structures with an excellent radiative quantum yield have been produced on GaAs[3,4] and InP[5,6] substrates. The study of these new QD structures has permitted the identification of unique and interesting physical phenomena. Although there are many publications about dot formation and results of their spectroscopy[7-10], a careful study of lateral size effect on the optical properties is still lacking. In this letter, we present the pronounced lateral confinement influence on the PL energy of InGaAs QDs in InAlAs grown on InP(001). PL emission with two peaks at 0.627 and 0.657eV is observed, and is correlated to the distinct bimodal size distribution of QDs.

The sample was grown by molecular beam epitaxy (MBE) on a semi-insulating Fe-doped InP(001) substrate in a Riber 32p MBE system under an As_4 partial pressure of 1×10^{-7} Torr. A 300nm lattice-matched $In_{0.52}Al_{0.48}As$ was grown on the InP substrate at a growth rate of 0.6μm/h at 500°C. After cooling the substrate to 470°C, the nominal $In_{0.9}Ga_{0.1}As$ of 9.6ML was deposited at a reduced growth rate of ~0.08ML/s. Subsequent 80nm $In_{0.52}Al_{0.48}As$ layer was then grown in order to freeze the evolution of the InGaAs layer morphology, while the temperature was ramped back to 500°C. A 5nm $In_{0.53}Ga_{0.47}As$ cap layer was grown as the last layer to protect the $In_{0.52}Al_{0.48}As$ from oxidation. The QDs formation was observed by the reflection high energy electron diffraction spectrum from a streaked to a spotty pattern. A transmission electron microscopy (TEM) study was performed at 200kV using plan-view and [110] cross sectional specimens thinned by mechanical polishing and argon ion milling. The PL measurements were performed on an IFS120 HR fourier transform infrared spectrameter with an Ar^+ laser (514.5nm) source. The sample was cooled in a closed-cycle He cryostat. An InSb detector and a CaF_2 beam splitter were employed to record the spectra.

Plan-view micrograph of sample is shown in Fig.1(a). The coherent dot formation is clearly evident through the strain contrast. The diameter of the dots was determined by measuring the the length of the white/black boundary. The dark area originates from the nonuniformity introduced in TEM specimens fabrication process (polishing and milling). The areal density of QDs is $3.3\times10^{11}cm^{-2}$. A high-magnification cross section micrograph of sample is displayed in Fig.1(b). The QDs is about 6.5nm in height with very small fluctuation, indicating most of QDs reach their height limit at high InGaAs coverage. Moreover, the InGaAs wetting layer is generally very thin and some of breaking. Using the plan-view TEM

result, statics on the QD size is summarized in Fig.2. Obvious bimodal size distribution is observed. The mean diameters and the corresponding standard deviations were obtained according to the method used in Ref.11: 30 and 5nm, 70 and 6nm for two branches, respectively. Each branch of QDs is fairly uniform in size. For the coherent Stranski-Krastanow growth mode, the best dot uniformity has been found to be for thicknesses just slightly larger than the critical thickness necessary to induce the dot formation (~8ML)[5,12]. The 2D nominal coverage of 9.6ML $In_{0.9}Ga_{0.1}As$ happens to satisfy this condition. These unexpected TEM results are different from the results of strained InGaAs/InAlAs system on InP(311) substrates[13] and InAs QDs in InAlAs on InP(001) substrate[5].

The sample gave relatively strong PL emission. Fig.3 displays PL spectra measured at 15K with various excitation power densities. The lineshapes show well-resolved doublet peaks at the energies of 0.627 and 0.657eV with full width at half maximum (FWHM) of 29 and 71meV, respectively. The PL can unambiguously be attributed to the InGaAs QDs, since the buffer layers have been found to have PL emission only near the InAlAs band gap. We attribute the discrete emission energies of the PL spectrum to radiative recombination from dots grouped in distinct branches, each one with almost the same dot height but with remarkably well defined lateral sizes as indicated by the TEM results. Indeed, we exclude that the higher energy component of spectra may stem from excited states of QDs, since the integrated PL intensities depend linearly on the excitation density. On the other hand, the intensity ratio of two peaks keeps constant, proving no efficient carrier transfer between two families of QDs. In addition, emission signal from InGaAs wetting layer is not observed, indicating efficient carrier transfer from 2D wetting layer to QDs due to the high areal density of QDs. Fig.4 shows two spectra obtained at temperatures of 15 and 80K. Each FWHM of resolved doublet peaks is temperature-independent up to 80K, but both PL peaks redshifted by 6meV. This temperature-independent FWHM is one of the predominant characteristics of QD structures[14].

To corroborate the interpretation on the correlation of bimodal size distribution and PL spectrum of QDs, theoretical depiction is necessary. Vertical and lateral confinements are handled separately. Due to the strong confinement in the growth direction, the energetic position of the QDs PL is mainly determined by the height of the QDs[10]. If we do not take into account lateral confinement, we can calculate the electron to heavy hole (e-hh) transition energy by modeling the QDs as a quantum well, in which the width is the height of the QDs

determined with TEM. In calculation, the strain-induced band shift is neglected, since the dots allow the system to lower its energy through relaxation of strain at the free surface. The conduction band offset is taken to be 70% of the band gap difference. The QDs of 6.5nm in height gives the e-hh transition energy of 0.61eV.

Coming now to the influence of lateral confinement of QDs. As a first approximation, we use a simple 2D infinite harmonic potential model and neglect the Coulomb interaction between the electrons and holes[15]. The infinite rotational-symmetric parabolic potential is given by $V_i = \frac{1}{2} m_i^* \omega_i^2 r^2$, where i=e or h, ω_i is the characteristic frequency, m_i is the effective mass, and r is the radius of the potential. The lateral confinement energy is given by $\Delta E = \frac{1}{2} \hbar \omega_e + \frac{1}{2} \hbar \omega_h$. For $In_{0.9}Ga_{0.1}As$, m_e^*=0.028m_o, m_{hh}^*=0.333m_o. Consequently, we obtain ΔE=39 and 17meV for r=30 and 70nm, respectively. Lateral confinement induced PL peak separation is 22meV. Considering the dot diameter determined by TEM is an overestimation of actual dot diameter, this calculated peak separation should be even larger. Pronounced influence of the lateral confinement of QDs accounts sucessfully for the experimental PL peak separation. Furthermore, different FWHMs of well-resolved doublet peaks correlate to the different lateral size distribution range of two QD branches.

In conclusion, we have presented the results of MBE grown InGaAs self-assembled QDs in InAlAs on an InP substrate. The islands formation is confirmed from the TEM measurements which showed an areal density of $3.3 \times 10^{11} cm^{-2}$, 6.5nm in height, and a bimodal size distribution with average diameters of 30 and 70nm, respectively. The PL emission with two peaks centered at 0.627 and 0.657eV strongly correlates to the bimodal size distribution of QDs.

References

[1] N.Yokoyama,S.Muto, K.Imamura, M.Takatsu, T.Mori, Y.Sugiyama, Y.Sakuma, H.Nakao, and T.Adachihara, Solid-State Electron. **40**, 505(1996).

[2] H.Shoji, K.Mukai, N.Ohtsuka, M.Sugawara, T.Uchida, and H.Ishikawa, IEEE Photonics Technol.Lett. **7**, 1385(1995).

[3] J.Y.Marzin and J.M.Gérard, Superlattices Microstruct. **5**, 51(1989).

[4] D.Leonard, M.Krishnamurthy, C.M.Reaves, S.P.DenBaars, and P.M.Petroff, Appl.Phys.Lett. **63**, 3203(1993).

[5] S.Fafard, Z.Wasilewski, J.McCattrey, S.Raymond, and S.Charbonneau, Appl.Phys.Lett. **68**, 991(1996).

[6] N.Marchand, P.Desjardins, S.Guillon, J.-E.Paultre, Z.Bougrioua, R.Y.-F.Yip, and R.A.Masut, Appl.Phys.Lett. **71**, 527(1997).

[7] K.Mukai, N.Ohtsuka, H.Shoji, and M.Sugawara, Appl.Phys.Lett. **68**, 3013(1996).

[8] M.Colocci, F.Bogani, L.Carraresi, R.Mattolini, A.Bosacchi, S.Franchi, P.Frigeri, M.Rosa-Clot, and S.Taddei, Appl.Phys.Lett. **70**, 3140(1997).

[9] M.Colocci, F.Bogani, L.Carraresi, R.Mattolini, A.Bosacchi, S.Franchi, P.Frigeri, S.Taddei, and M.Rosa-Clot, Superlattices Microstruct. **22**, 81(1997).

[10] K.H.Schmidt, G.Medeiros-Ribeiro, J.Garcia, and P.M.Petroff, Appl.Phys.Lett. **70**, 1727(1997).

[11] Y.Madea, Phys.Rev. B**51**, 1658(1995).

[12] B.W.Wessel, J.Vac.Sci.Technol.B**15**, 1056(1997).

[13] R.Nö tzel, J.Temmyo, A.Kozen, and T.Tamamura, Appl.Phys.Lett. **66**, 2525(1995).

[14] S.Raymond, S.Fafard, S.Charbonneau, R.Leon, D.Leonard, P.M.Petroff, and J.L.Merz, Phys.Rev. B**52**, 17238(1995).

[15] H.Lipsanen, M.Sopanen, and J.Ahopelto, Phys.Rev. B**51**, 13868(1995).

Figure captions

Figure 1. TEM micrograph of QDs developed after the growth of nominal 9.6ML $In_{0.9}Ga_{0.1}As$ in InAlAs lattice-matcned to InP. The plan view is shown in (a), and the cross-section view is in (b).

Figure 2. Statics of the size of the InGaAs QDs grown on InAlAs lattice-matched to InP, from TEM plan view. The measured dot number is 155. The average diameters and standard deviations of two branches are 30 and 5nm, 70 and 6nm, respectively.

Figure 3. PL spectra at 15K with different excitation intensities. I= $0.2W/cm^2$.

Figure 4. PL spectra obtained at different temperature.
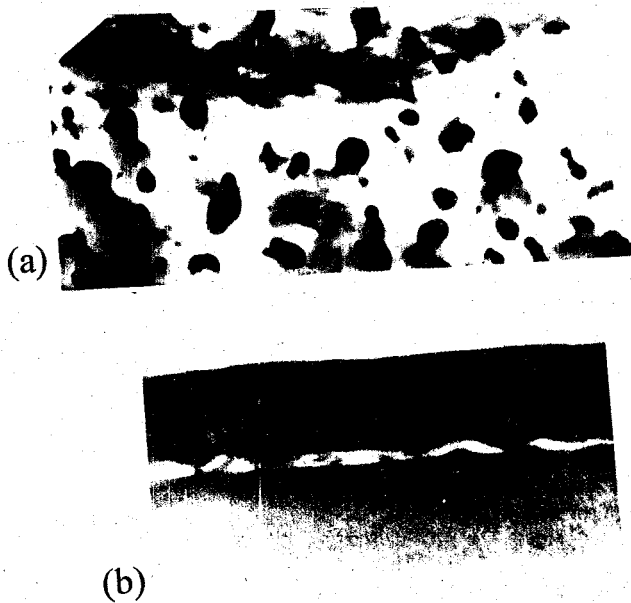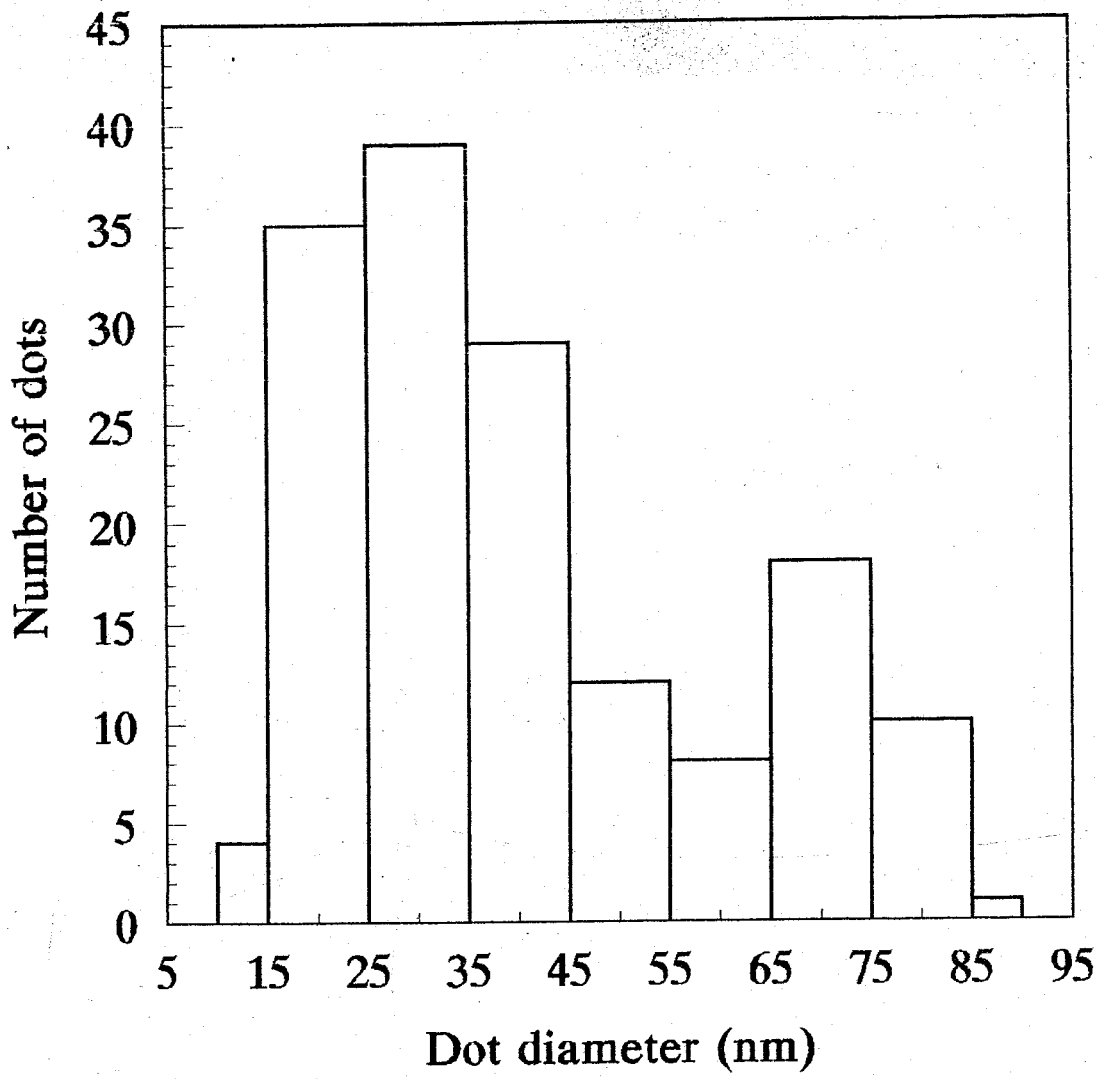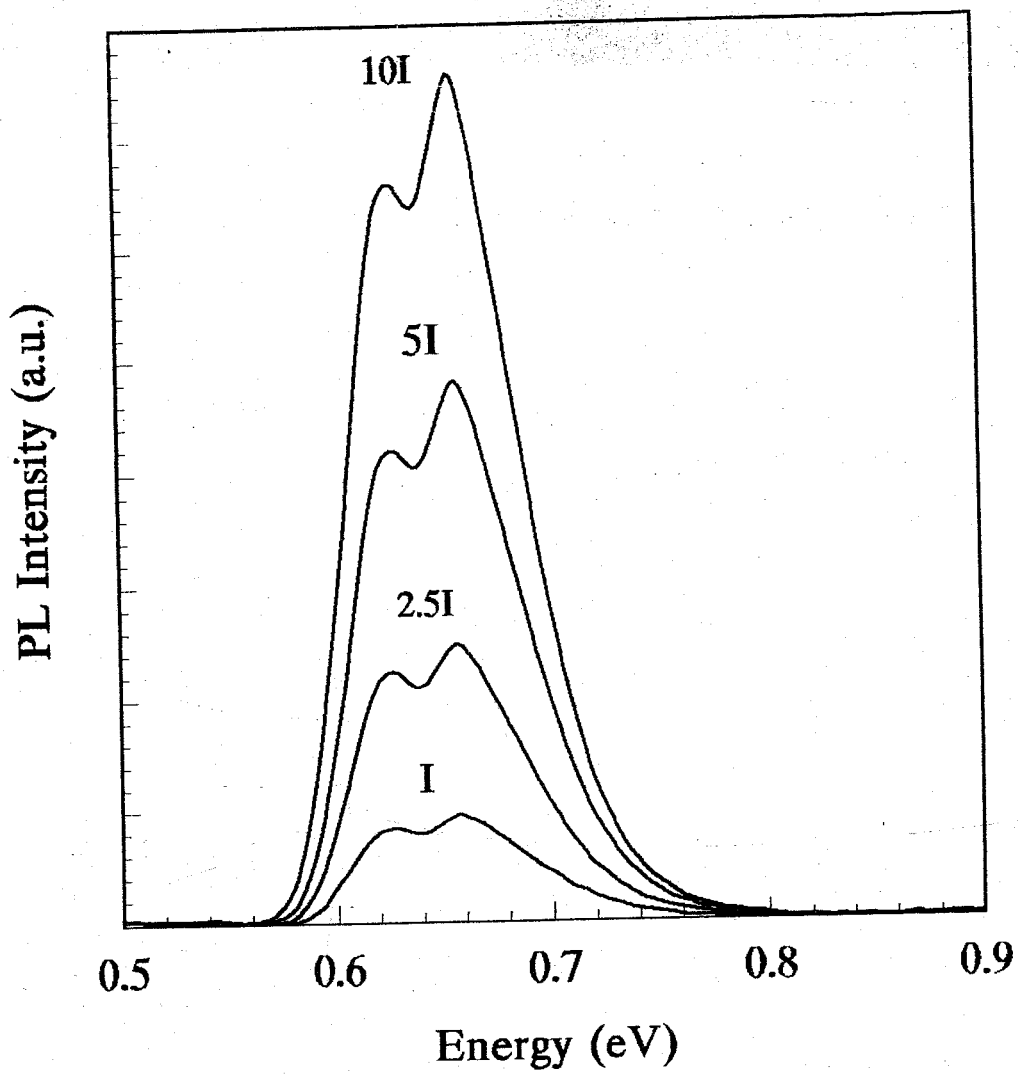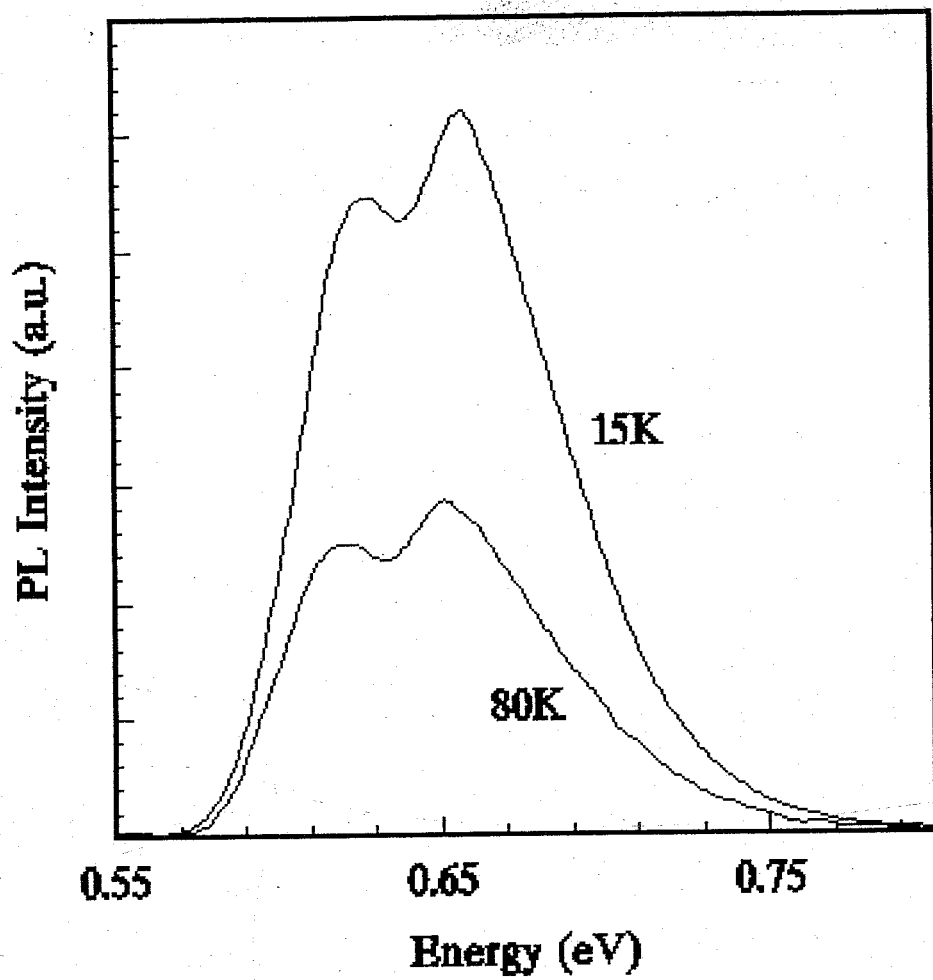
(a)

Fig. 1

(b)

Fig. 2

43

Fig. 3

44

Fig. 4

45

Size quantization effects in InAs self-assembled islands on InP(001)

at the onset of 2D-to-3D transition

Feng-Qi Liu[a] , Zhan-Guo Wang, Ju Wu, Bo Xu, Jia-Jun Qian, and Ji-Ben Liang

Laboratory of semiconductor materials science, Institute of semiconductors,

Chinese Academy of Sciences, P. O. Box 912, Beijing 100083, China

Abstract

Photoluminescence spectroscopy has been used to investigate self-assembled InAs islands in InAlAs grown on InP(001) by molecular beam epitaxy, in correlation with transmission electron microscopy. The nominal deposition of 3.6 monolayers of InAs at 470°C achieves the onset stage of coherent island formation. In addition to one strong emission around 0.74eV, the sample displaces several emission peaks at 0.87, 0.92, 0.98, and 1.046eV. Fully developed islands coexist with semi-finished disk islands account for the multipeak emission. These results provide strong evidence of size quantization effects in InAs islands.

PACS: 78.55.Cr, 78.66.Fd, 68.65.+g

---

[a] To whom correspondence should be addressed. E-mail: fqliu@red.semi.ac.cn

1. Introduction

The formation of coherent three-dimensional (3D) islands in lattice mismatched systems by the Stranski-Krastanov growth mode has attracted much attention since these defect-free islands are expected to lead to major developments for future nanoscale optoelectronic devices[1]. The island formation process is driven by the reduction of the total strain and surface energy of the layer-substrate system and is limited by kinetic factors such as adotom diffusion[2,3]. To capture the evolution of island formation and growth, several groups have investigated the initial morphological instability of a strained layer and the kinetic pathways to 3D islands[4,5]. Although there are many publications about islands growth and results of their spectroscopy in the InAs/GaAs system[6,7], a careful study of InAs islands on InP at the onset of 2D-to-3D transition is still lacking. In this letter, we report the photoluminescence (PL) and transmission electron microscopy (TEM) results obtained for the molecular beam epitaxy (MBE) grown InAs islands embedded in InAlAs lattice-matched to an InP substrate, at the very onset of 2D-to-3D transition.

2. Experiments

The sample was grown by molecular beam epitaxy (MBE) on a semi-insulating Fe-doped InP(001) substrate in a Riber 32p MBE system. Substrate rotation and an As_4 partial pressure of 1×10^{-7} Torr were used during the growth. A 300nm lattice-matched $In_{0.52}Al_{0.48}As$ was grown on the InP substrate at a growth rate of $0.6\mu m/h$ at 500°C. After cooling the substrate to 470°C, the thin InAs layer was deposited at a reduced growth rate of $\sim 0.2\mu m/h$, and this was done until the transition from 2D growth to 3D growth was observed by the reflection high-energy electron diffraction (RHEED) spectrum from a streaked to a spotty pattern. This transition corresponds to 2D nominal deposition of 3.6 monolayers (ML) which is in excellent quantitative agreement with the predicted critical thickness[8]. After a 2s growth interruption, subsequent 80nm $In_{0.52}Al_{0.48}As$ layer was then grown in order to freeze the evolution of the InAs layer morphology, while the temperature was ramped back to 500°C. A 5nm $In_{0.53}Ga_{0.47}As$ cap layer was grown as the last layer to protect the $In_{0.52}Al_{0.48}As$ from oxidation. Specimens for TEM were prepared in plan-view and in cross section manners. The PL measurements were performed on an IFS120 HR fourier transform infrared spectrometer with an Ar^+ laser (514.5nm) source. The sample was cooled in a closed-cycle He cryostat. An InSb detector and a CaF_2 beam splitter were employed to record the spectra.

3.Results and discussion

TEM micrographs of the sample are shown in Figure 1. The coherent island formation is clearly evident through the strain contrasts as previously observed for the case of InGaAs/GaAs and InAlAs/AlGaAs self-assembled islands. The areal density of islands is 4×10^9cm^{-2}, and the size distribution of islands is relatively wide. In Fig.1(a), besides the apparent 3D islands, some of threadlike microstructures are observed. We observe islands coexist with wires clearly, but we have no sound explanation about these wire structures at present. The high-magnification cross section micrograph in Fig.1(b) also reveals the island formation. Unfortunately, it is difficult to obtain a clear contrast in cross-section TEM for this material system. Although we can not exactly determine the island height, we can see the large fluctuations in height and in width clearly. Also apparent here is the semi-finished disk islands coexist with fully developed islands. What is more, the separation between semi-finished island and fully developed island is large. Using the plan-view TEM result, statics on the island size is extracted and is indicated in Fig.2. The 3D islands show large dispersion is size, seemingly multimodal size distribution with most frequent diameters of 40, 70, and 100nm, respectively, is observed. These TEM results are quite different from those reported results about InAs islands on InP substrate[9-12].

According to Mérard et al.[6], island nucleation is governed by random surface process, step, defects, or local thickness fluctuations[6]. All islands rapidly reach a certain size, below which they are unstable and which more or less corresponds to an optimum of the elastic relaxation. The fast initial stage of the evolution of the InAs islands corresponds to the growth at the expense of the surrounding 2D InAs layer, after which the film undergoes a much slower evolution by inter-island matter transfer. The size fluctuation is more striking when the InAs deposition rate reduced. This picture concering the nucleation and growth kinetics of InAs islands is particularly useful to understand the origin of their size fluctuation. At the very onset of 2D-to-3D transition, the growth of islands is initiated via the formation of 2D platelets which act as precursors[3]. It has been proposed that 2D platelets may have an energetic minimum at a certain size, leading to equal size islands assuming that the islands do not change their volume during nucleation[3]. However, the growth of 2D platelets is a kinetically controlled process; the size deviation for 2D platelets is usually much large[13].

For lower growth temperature and thinner InAs layer thickness, lateral mass transport is hindered to some extent. The surface diffusion is not fast enough for these platelets to reach an equilibrium distribution, and consequently, the resulting islands have relative large fluctuations in height and in width. The very small growth interrption time and the subsequent InAlAs cap layer provide a prerequisite for freezing the evolution of the InAs layer morphology.

The sample gave distinctive strong PL emission. Fig.3(a) presents PL emission obtained at different temperatures with excitation power of $0.5W/cm^2$. In addition to an intense PL peak around 0.74eV, several peaks at 0.87, 0.92, 0.98, and 1.04eV are seen. Each peak energy and the corresponding full width at half maximum (FWHM) almost unchanged up to 118K. Since the possible PL emission from buffers is only near the InAlAs band gap (~1.5eV at low temperature), the observed multipeak emission can unambiguously attributed to InAs layer. The 2D emission from the wetting layer is obsent in the spectra (2D emission energy of 3.6ML InAs is no less than 1.2eV[14], wetting layer emission energy is still more higher). This behavior is due to the absence of bound states in the well. As a result, a "quantum depletion" takes place that drives the charges toward the islands. Fig.3(b) shows spectra obtained at various excitation power densities. The integrated PL intensity of each peak depends linearly on the excitation density, and the relative amplitude keeps constant. From the intensity-independent feature and relative lower excitation in our experiment, the possibility of state filling can be ruled out[15].

We attribute the observed peaks to the ground state emission of island families with different heights. The main PL peak at 0.74eV is correlated with the fully developed island family, while the other peaks are related to families of semi-finished islands with different heights. To elucidate this phophesy, theoretical evaluation is necessary. Due to the strong confinement in the growth direction, the energetic position of the PL is mainly determined by the height of the islands. Since the island height is much smaller than its diameter, a change in the overal thickness of the island has a big influence on the absolute energetic position of the PL. If we do not take into account lateral confinement, we can roughly calculate the electron to heavy hole (e-hh) transition energy by modeling the island as a quantum well, in which the width is the height of island. The observed PL peak energies at 0.74, 0.87, 0.92,

0.98, and 1.04eV give the calculated island heights of 13, 9, 8, 7, and 6ML, respectively. As expected, a change in lateral size, mainly influence the FWHM to some extent. By modeling the lateral quantum confinement potential for both an electron and a hole as harmonic-oscillator-type potentials, we get lateral confinement energies 30, 17, and 13meV for lateral sizes of 40, 70, and 100nm, respectively. Thus the lateral confinement influence on the PL energy is trivial, and will not affect the above qualitative results. We can conclude that the obvious steplike behavior of PL peak energies stems from island families with distinctive heights. These results clearly indicate that the size quantization effect is pronounced at the onset of 2D-to-3D transition[7,16,17].

4. Conclusions

We have presented a correlated PL and TEM study of MBE grown InAs islands in InAlAs on an InP substrate at the onset of 2D-to-3D transition. The island formation is confirmed from the TEM measurements which showed large fluctuation in height and in width. Fully developed islands coexist with semi-finished disk islands are identified. Strong radiative recombination is observed, with steplike PL energies at 0.74, 0.87, 0.92, 0.98, and 1.04eV. Our results provide strong evidence of the size quantization effects in InAs islands.

Acknowledgements

References

1. B.G.Levi, Phys.Today **49**, No.6, 22(1996).

2. J.Tersoff and F.K.Le Goues, Phys.Rev.Lett.**72**, 3570(1994).

3. C.Priester and M.Lannoo, Phys.Rev.Lett.**75**, 93(1995).

4. J.Tersoff, Y.H.Phang, Z.Zhang, and M.G.Lagally, Phys.Rev.Lett.**75**, 2730(1995).

5. K.M.Chen, D.E.Jesson, S.J.Pennycook, T.Thundat, and R.J.Warmack, Phys.Rev. B**56**, 1700(1997).

6. J.M.Gérard, J.B.Génin, J.Lefebvre, J.M.Moison, N.Lebouché, and F.Barthe, J.Crystal Growth **150**, 351(1995).

7. M.Colocci, F.Bogani, L.Carraresi, R.Mattolini, A.Bosacchi, S.Franchi, P.Frigeri, M.Rosa-Clot, and S.Taddei, Appl.Phys.Lett.**70**, 3140(1997).

8. B.W.Wessels, J.Vac.Sci.Technol.B**15**, 1056(1997).

9. S.Fafard, Z.Wasilewski, J.McCaffrey, S.Raymond, and S.Charbonneau, Appl.Phys.Lett. **68**, 991(1996).

10. A.Ponchet, A.Le Corre, H.L' Haridon, B.Lambert, and S.Salaün, Appl.Phys.Lett.**67**, 1850(1995).

11. H.Marchand, P.Desjardins, S.Guillon, J.-E.Paultre, Z.Bougrioua, R.Y.-F.Yip, and R.A.Masut, Appl.Phys.Lett.**71**, 527(1997).

12. S.Fréchengues, V.Drouot, B.Lambert, D.Lemoine, S.Loualiche, A.Le Corre, and H.L'Haridon, Appl.Phys.Lett.**71**, 2818(1997).

13. J.G.Amar and F.Family, Phys.Rev.Lett.**74**, 2066(1995).

14. E.Tournié, O.Brandt, and K.Ploog, Appl.Phys.Lett.**60**, 2877(1992).

15. S.Raymond, S.Fafard, P.J.Poole, A.Wojs, P.Hawrylak, S.Charbonneau, D.Leonard, R.Leon, P.M.Petroff, and J.L.Merz, Phys.Rev.B**54**, 11548(1996).

16. M.Colocci, F.Bogani, L.Carraresi, R.Mattolini, A.Bosacchi, S.Franchi, P.Frigeri, S.Taddei, and M.Rosa-Clot, Superlattices Microstruct.**22**, 81(1997).

17. K.H.Schmidt, G.Medeiros-Ribeiro, J.Garcia, and P.M.Petroff, Appl.Phys.Lett. **70**, 1727(1997).

Figure captions

Figure 1. TEM micrographs of InAs islands developed after a 2D nominal deposition of 3.6ML in InAlAs lattice-matcned to InP. The plan view and cross-section view are shown in (a) and (b), respectively.

Figure 2. Statics of the size of the InAs islands grown on InAlAs lattice-matched to InP, from TEM plan view.

Figure 3. PL spectra obtained at different temperature with excitation density of $0.5 W/cm^2$.

Figure 4. PL spectra at 15K with different excitation intensities. $I= 0.25 W/cm^2$.

(a) 400nm

(b) 200nm

(c) 50nm
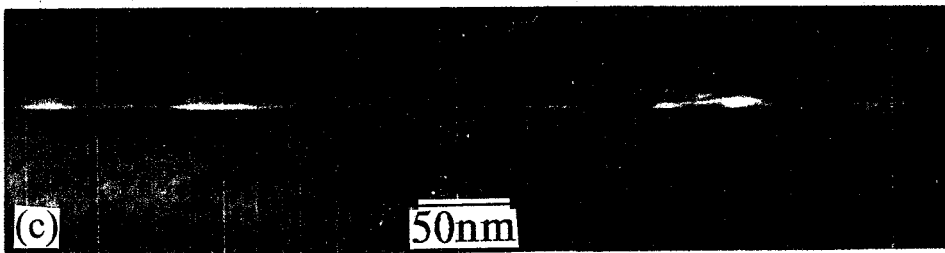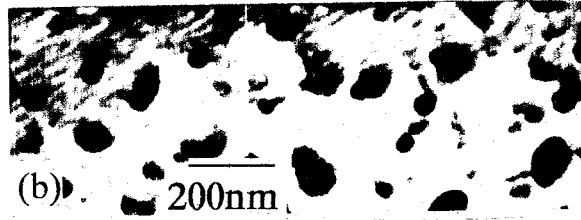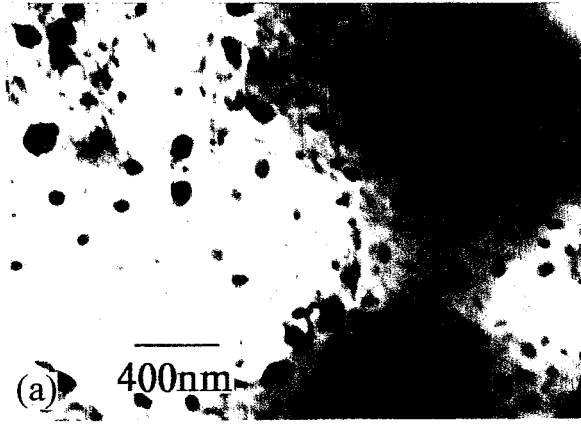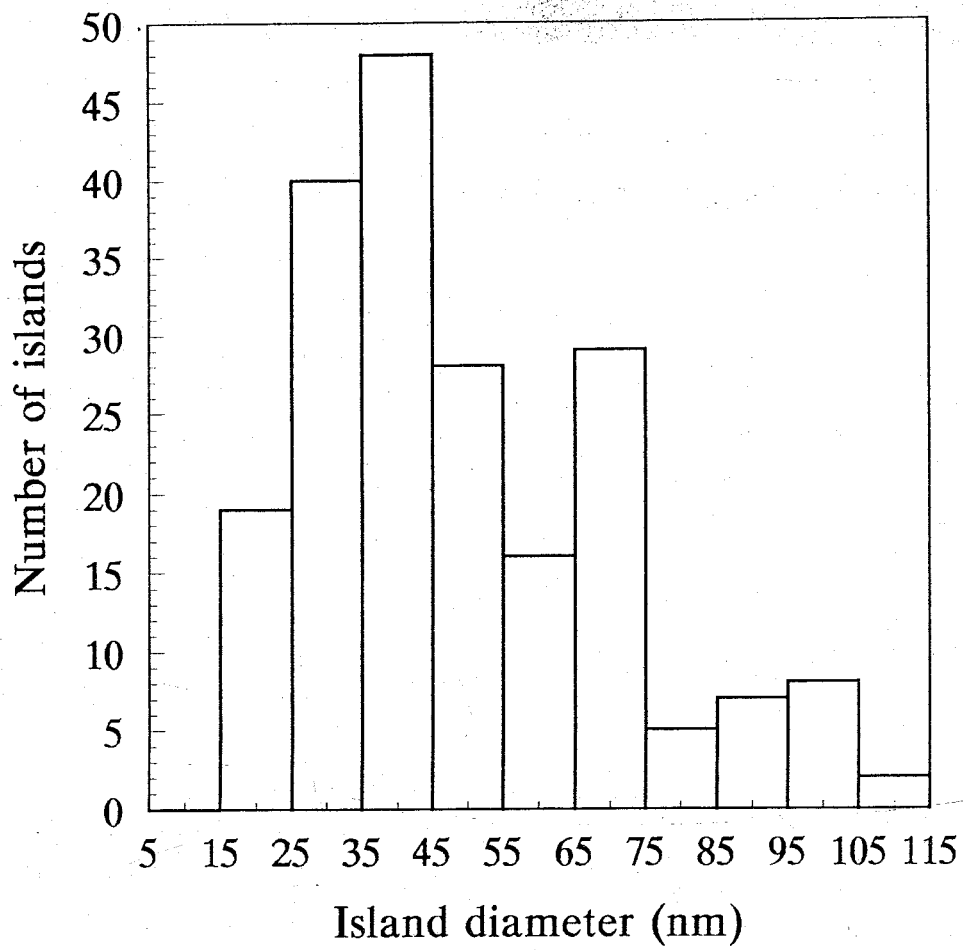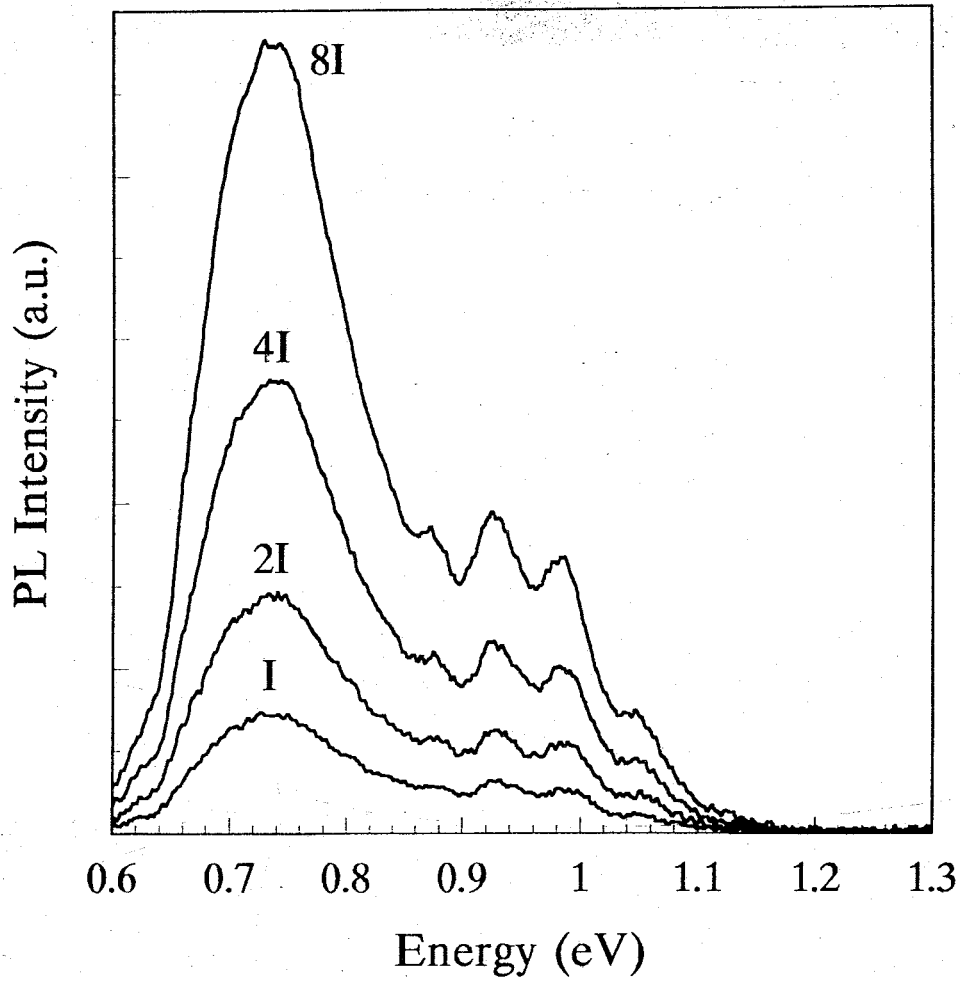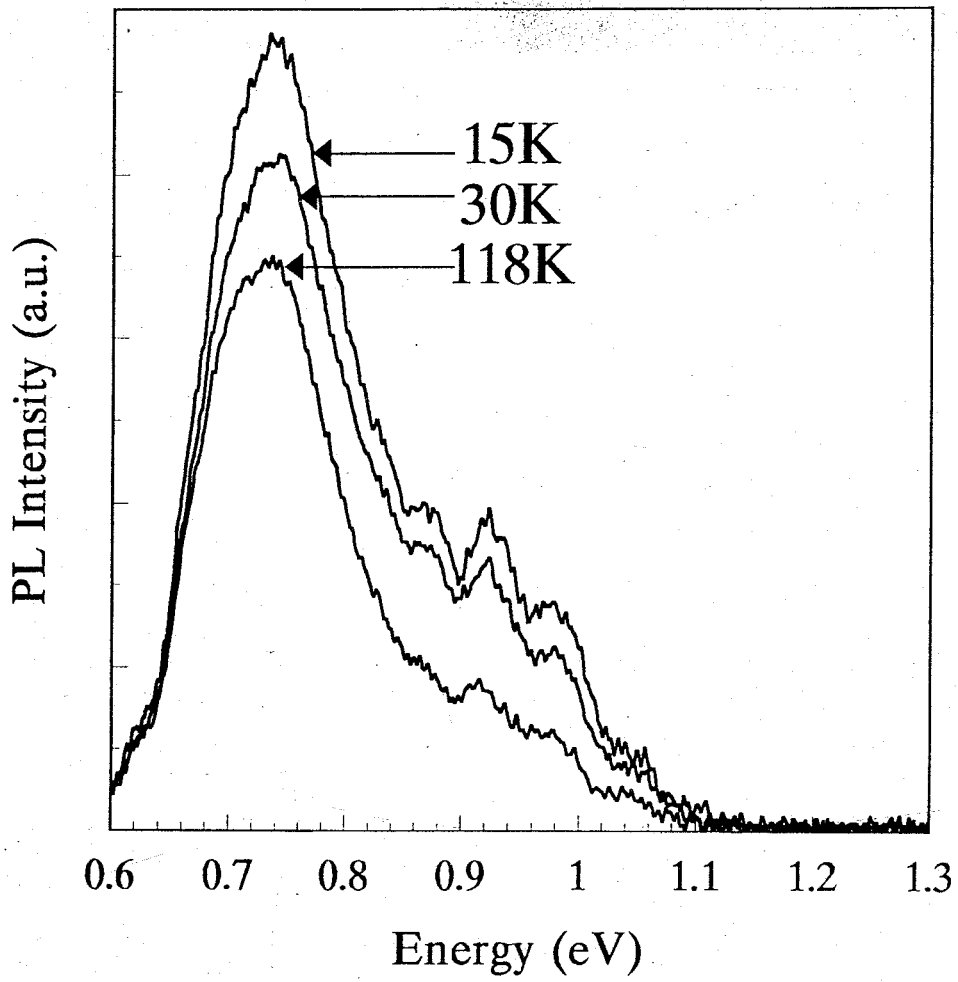
Metamorphosis of Self-Organized Quantum Dots into Quantum Wires

Feng-Qi Liu[a], Zhan-Guo Wang, Bo Xu, Ju Wu, and Jia-Jun Qian

Laboratory of semiconductor materials science, Institute of semiconductors, Chinese Academy of Sciences, P. O. Box 912, Beijing 100083, China

Abstract

Spontaneous formation of InAs quantum wires in InAlAs on InP(001) via sequential chain-like coalescence of quantum dots along $[1\bar{1}0]$ are realized. Theoretical calculation based on the energetics of interacting steps provides a qualitative explanation for the experimental results. Sequential coalescence of initial isolate dots reduces the total free energy strikingly. Thus the wire-like structure is energetically favorable.

Keywords: Quantum dot; Sequential coalescence; Quantum wire.

PACS: 68.65+g, 81.10.Aj, 81.15.Hi, 61.16.Bg

Recently, much effort has been devoted to study quasi-one-dimensional structures, which act as "quantum wires" with fascinating electronic and optical properties[1,2]. Quantum wire structures grown by conventional methods of patterning, etching or compositional modulation typically suffer from insufficient confinement, large wire-width, increased surface defects etc[1-4]. Although formation methods of strain induced lateral ordering[5] and one-dimensional (1D) faceting[6] offer attractive routes to overcome these difficulties, the strigent requirements for device purposes remain challenging issues. Therefore it is necessary to explore some new methods for fabricating true quantum wires in the sense of significant lateral and longitudinal confinement, which promise practical applications.

It is well known that highly mismatched heteroexpitaxy can lead to the formation of self-assembled quantum dots, and well-ordered and high-density arrays of dots with clear faceting have been achieved[7]. On the other hand, surprising alignment and pronounced preferential elongation of dots under specific condition have been reported[8,9]. These brilliant achievements and interesting phenomena, have, in turn, sparked our prevision that spontaneous formation of quantum wires may be occur if elongated dots are sequentially arranged.

In this Letter we report a surprising route to spontaneous formation of InAs quantum wires on InP (001) by sequential chain-like coalescence of dots along [$1\bar{1}0$]. This is very different from the 1D faceting by step bunching epitaxial growth. The distinct elongated dots and their sequential coalescence traces are directly revealed by transmission elctron microscopy (TEM) measurements. The change of the strain and surface energy has been calculated, which has shown that the decrease of surface energy can outweigh the increase of the strain energy when isolate dots coalesce sequentially. This fascinating self-assembling feature of quantum wires may point the way toward a new approach to the fabrication of such structures.

The samples were grown by molecular beam epitaxy (MBE) on semi-insulating Fe-doped InP(001) substrates in a Riber 32p MBE system. Substrate rotation and an As_4 partial pressure of 1×10^{-7}Torr were used during the growth. The growth temperature

was monitored using the substrate thermocouple. A 0.3μm lattice-matched InAlAs buffer layer was grown on the InP substrate at a growth rate of 0.6μm/h at 500°C. For more accurate control, after cooling the substrate to 470°C, the thin InAs layer(s) and InGaAs marker layer(s) were deposited at reduced growth rates. Sample 1 contains 3.6 monolayers (ML) InAs layer ($\sim 0.18\mu/h$) and 2ML $In_{0.6}Ga_{0.4}As$ marker layer($\sim 0.3\mu/h$), which were capped with 35nm InAlAs. For sample 2, the combination of 4ML InAs layer, 2ML $In_{0.53}Ga_{0.47}As$ marker layer($\sim 0.34\mu/h$), and 5nm InAlAs spacer layer($\sim 0.346\mu/h$) was repeated 5 times, and capped with 35nm InAlAs. After each InAs layer, a 30s growth interruption was introduced. The transition from 2D growth to 3D growth was observed by the reflection high-energy electron diffraction spectrum from a streaked to a spotty pattern.

TEM micrographs of the samples 1 and 2 are shown in Figs. 1(a) and 1(b), respectively. The coherent formation of elongated dots and wire-like structures are clearly evident. Slightly different features between 1(a) and 1(b) arise from different sample growth conditions. These TEM results are quite different from those reported results about InAs and InGaAs heteroepitaxial layers on InP substrate[8-11]. *The pronounced feature is the sequential ordering and coalescence along [1$\bar{1}$0] direction.* Although platelets elongated along the [1$\bar{1}$0] and a height undulation in the [110] direction both in compressive and tensile strained $In_{1-x}Ga_xAs$/InP(001) epilayers have been reported[9], the detailed mechanisms governing the formation of elongated 3D dots or chain-like surface structures have not been well characterized.

We now consider the physical origin of this crossover from dots to wire. As we know, under conditions of relatively high misfit coherency strain, heteroepitaxial thin film exhibits a morphological instability, characterized by spontaneous roughening[12-14]. The stress-induced roughening of an initially flat surface requires nucleation of steps or facets. The properties of atomic steps play an important role in determining the equalibrium morphologies of surfaces and dynamics of 3D dot formation process and surface faceting[15,16]. This behavior is governed by the energetics of the strain field and the surface, subject to the kinetics of adatom transport that regulate nucleation

and evolution of dots, in competition with dislocation introduction. Here we consider the growth of quantum wires is initiated via the formation of quantum dots which act as presursors. We suppose that the surface diffusion is fast enough for these initial quantum dots to reach an equilibrium redistribution and ordering[8], and we show from total energy calculations that the quantum dots sequential coalescence driven by anisotropic stress is energetically favored. For simplicity, we take the initial isolate dots to be square-based pyramidal in shape, with stepped surfaces just as illustrated by Chen *et al.*[17], and the dots geometry are given in Fig.2(a). The average spacing between neighboring step edges is determined by the mean inclination angle θ of the surface and the dot base size 2s. We use the kinetic model based on interacting surface steps to evaluate the surface energy of quantum dot. In this case, the energetics of the interacting steps, rather than the surface energy of a particular stable facet, will dominate the kinetic pathway of dot nucleation. The elastic relaxation energy drives the 3D dot formation but is opposed by the cost in surface energy associated with the creation of steps. Since the dot preferentially elongated along [1$\bar{1}$0] direction, we label two distinct steps running [1$\bar{1}$0] and [110] directions as S_A and S_B, respectively[9]. We simply adopt the corresponding step creation energies per unit length, λ_A and λ_B, by the forms[17]

$$\lambda_A = \lambda_{A0} + \lambda_{Ad}(\frac{a}{h\cot\theta})^2; \qquad \lambda_B = \lambda_{B0} + \lambda_{Bd}(\frac{a}{h\cot\theta})^2 \qquad (1)$$

where h and a are the step height and surface lattice constant, respectively, each second term represents contributions from repulsive interactions between steps or "force dipoles". In order to simplify calculation, we assume $\lambda_{B0} = \alpha\lambda_{A0}$ and $\lambda_{Bd} = \alpha\lambda_{Ad}$. Due to dots elongated along [1$\bar{1}$0] direction as illustrated in Figs.1(a) and 1(b), the strain is relaxed mainly along [110] direction. therefore $\alpha \geq 1$. The total free energy of a pyramidal stepped dot is [13,17]

$$E_1(s, \theta) = -6cs^3 \tan^2\theta + \frac{2s^2(1 + \alpha)\tan\theta}{h}[\lambda_{A0} + \lambda_{Ad}(\frac{a}{h\cot\theta})^2] \qquad (2)$$

The first term is the energy change due to elastic relaxation, and second term is the additional cost in surface free energy. Here $c = \sigma^2(1 - \nu)/2\pi\mu$, where μ and ν are the shear modulus and Poisson ratio of the substrate and σ is the bulk stress of the uniform

epilayer. Clearly a minimum energy barrier $E_1^*(s_c, \theta_c)$ must be overcome to form a dot. This barrier height is

$$E_1^*(s_c, \theta_c) = \frac{64}{225\sqrt{5}}(1 + \alpha)^3 \frac{a\lambda_{A0}^2 \sqrt{\lambda_{A0}\lambda_{Ad}}}{h^4 c^2} \tag{3}$$

which occurs at a saddle point (s_c, θ_c) with

$$\tan \theta_c = (\frac{h}{a})\sqrt{\frac{\lambda_{A0}}{5\lambda_{Ad}}} \tag{4}$$

$$s_c = \frac{4(1 + \alpha)}{3\sqrt{5}} \times \frac{a\sqrt{\lambda_{A0}\lambda_{Ad}}}{h^2 c} \tag{5}$$

Now we consider the sequential coalescence of N isolate dots. When the stress is anisotropic, the dot should align perpendicular to the direction of maximum stress[18]. Therefore the quantum-dot-assembled wires should along [1$\bar{1}$0] direction just as the observed results. We assume that the final wire keeps hut shape (triangular cross section in the width), and shape changes only in [1$\bar{1}$0] direction, while the base width $2s$ and inclination angle θ fixed as indicated in Fig.2(b). The total free energy of the final wire is

$$E_N(s, \theta) = -2[2N+1+\ln\frac{4N-1}{3}]cs^3 \tan^2\theta + [(1+\alpha) + \frac{4\alpha}{3}(N-1)]\frac{2s^2 \tan\theta}{h}[\lambda_{A0} + \lambda_{Ad}(\frac{a}{h\cot\theta})^2] \tag{6}$$

The energy change $\triangle E$ due to coalescence is $\triangle E = E_N(s, \theta) - NE_1(s, \theta)$. If we assume the saddle point of isolate dot remain, we get

$$\triangle E = [-7(N-1) + 5\alpha(N-1) - 2(1+\alpha)\ln\frac{4N-1}{3}] \times \frac{64(1+\alpha)^2}{675\sqrt{5}} \times \frac{a\lambda_{A0}^2 \sqrt{\lambda_{A0}\lambda_{Ad}}}{h^4 c^2} \tag{7}$$

We obtain $\triangle E < 0$ on condition that

$$\alpha < \frac{6}{2.5 - (N-1)^{-1}\ln\frac{4N-1}{3}} - 1 \tag{8}$$

Thus, if above coudition is satisfied, the quantum wire can be spontaueously formed.

If we do not fix the width of wire, the saddle point $(s_c^{wire}, \theta_c^{wire})$ of quantum wire can be deduced from Eq.(6),

$$\tan \theta_c^{wire} = (\frac{h}{a})\sqrt{\frac{\lambda_{A0}}{5\lambda_{Ad}}} \tag{9}$$

61

$$s_c^{wire} = \frac{4[(1+\alpha) + \frac{4\alpha(N-1)}{3}]}{\sqrt{5}(2N+1+\ln\frac{4N-1}{3})} \times \frac{a\sqrt{\lambda_{A0}\lambda_{Ad}}}{h^2 c} \tag{10}$$

The corresponding minimum energy barrier is

$$E(s_c^{wire}, \theta_c^{wire}) = \frac{64}{25\sqrt{5}} \times \frac{[(1+\alpha) + \frac{4\alpha(N-1)}{3}]^3}{(2N+1+\ln\frac{4N-1}{3})^2} \times \frac{a\lambda_{A0}^2\sqrt{\lambda_{A0}\lambda_{Ad}}}{h^4 c^2} \tag{11}$$

The criterion for $s_c^{wire} = s_c$ is

$$\alpha = \frac{2N-2+\ln\frac{4N-1}{3}}{2N-2-\ln\frac{4N-1}{3}} \tag{12}$$

What is the essence of critical value of α to form quantum wire? Large α increases the minimum energy barrier $E_1^*(s_c, \theta_c)$, as a result, significantly reduces the maximum rate of initial dot nucleation. On the other hand, large α indicates large anisotropic stress. Since the spatial variation of stress associated with the step instability can dramatically affect the activation barrier for 3D dot nucleation[19], the anisotropy in step creation energies governs the equilibrium shape of dots[16]. Smaller S_A step creation energy indicate that preferential nucleation and coalescence along [1$\bar{1}$0] direction are permissive. Additionally, during dots growth and coalescence adatoms tend to diffuse on a surface away from sites with higher strain to sites with a lower strain[20]. This process still more facilitates the formation of quantum-dot-assembled wire.

The relationship between the ratio of step creation energies α and maximum coalescent dot number is displayed in Fig.3. Large difference of corresponding N indicates that prerequisite condition of $\triangle E > 0$ takes priority of $s_c^{wire} = s_c$. Invariably, $E(s_c^{wire}, \theta_c^{wire}) > E_1^*(s_c, \theta_c)$, consequently the quantum wire can not be spontaneously formed at the initial stage. Clearly the merely evolutionary pathway of wire is the sequential coalescence of initial dots, which are constrained to passover the saddle point of dots where the activation barrier is a minimum. The quantum dots can thus be reviewed as precursors for the formation of quantum wires. Based on our observations and calculations, we clearly demonstrate the route of metamorphosis of quantum dots into quantum wires.

In summary, we have demonstrated a kinetic pathway of quantum dot assembled wires. our simple model, based on the energetics of interacting steps, provides a useful qualitative description of observed results. The rather fascinating result of this study is that anisotropic stress in combination with interacing steps govern the metamorphosis of quantum dots into quantum wires.

References

[a] To whom the correspondence should be addressed. E-mail: fqliu@red.semi.ac.cn

1. K.Kash, J.M.Worlock, M.D.Sturge, P.Grabbe, J.P.Harbison, A.Scherer, and P.S.D.Lin, Appl.Phys.Lett. **53**, 782(1988).
2. M.L.Roukes, A.Scherer, S.J.Jr.Allen, H.G.Craighead, R.M.Ruthen, E.D.Beebe, and J.P.Harbison, Phys.Rev.Lett. **59**, 3011(1987).
3. B.I.Miller, A.Shahar, U.Koren, and P.I.Corvini, Appl.Phys.Lett. **54**, 188(1989).
4. J.Cibert, P.M.Petroff, G.J.Dolan, S.J.Pearton, A.C.Gossard, and J.H.English, Appl.Phys.Lett. **49**, 1275(1986).
5. P.Dua, S.L.Cooper, A.C.Chen, and K.Y.Cheng, Appl.Phys.Lett. **69**, 2261(1996).
6. R.Nötzel, J.Temmyo, and T.Tamamure, Appl.Phys.Lett. **64**, 3557(1994).
7. R.Nötzel, J.Temmyo, T.Tamamure, Science **369**, 131(1994).
8. A.Ponchet, A.Le Corre, H.L'Haridon, B.Lambert, and S.Salaün, Appl.Phys.Lett. **67**, 1850(1995).
9. P.Krapf, Y.Robach, M.Gendry, and L.Porte, Phys.Rev. **B55**, 10229(1997); J.Cryst.Growth **181**, 337(1997).
10. S.Fafard, Z.Wasilewski, J.McCaffrey, S.Raymond, and S.Charbonneau, Appl.Phys.Lett. **68**, 991(1996); R.Nötzel, J.Temmyo, A.Kozen, and T.Tamamure, *ibid.* **66**, 2525(1995).
11. H.Marchand, P.Desjardins, S.Guillon, J.-E.Paultre, Z.Bougrioua, R.Y.-F.Yip, and R.A.Masut, Appl.Phys.Lett. **71**, 527(1997); S.Fréchengues, V.Drouot, B.Lambert, D.Lemoine, S.Loualiche, A.Le Corre, and H.L'Haridon, *ibid.* **71**, 2818(1997).
12. B.J.Spencer, P.W.Voohees, and S.H.Davis, Phys.Rev.Lett. **67**, 3696(1991).
13. J.Tersoff and F.K.Le Goues, Phys.Rev.Lett. **72**, 3570(1994).
14. Y.H.Xie *et al.*, Phys.Rev.Lett. **73**, 3006(1994); *ibid.* **74**, 4963(1995).
15. E.D.Williams, Surf.Sci. **299/300**, 502(1994).
16. N.C.Bartlet, R.M.Tromp, and E.D.Williams, Phys.Rev.Lett. **73**, 1656(1994).
17. K.M.Chen, D.E.Jesson, S.J.Pennycook, T.Thundat, and R.J.Warmack, Phys.Rev. **B56**, 1700(1997).
18. J.Tersoff and R.M.Tromp, Phys.Rev.Lett. **70**, 2782(1993).
19. K.M.Chen, D.E.Jesson, S.J.Pennycook, M.Mostoller, and T.Kaplan, Phys.Rev.Lett. **75**, 1582(1995).
20. Q.Xie, P.Chen, and A.Madhukar, Appl.Phys.Lett. **65**, 2051(1994).

Figure captions

Figure 1. TEM micrographs of InAs quantum dot assembed wires in InAlAs lattice-matcned to InP: (a) sample 1, 3.6ML InAs marked by 2ML $In_{0.6}Ga_{0.4}As$; (b) sample 2, 4ML InAs marked by 2ML $In_{0.53}Ga_{0.47}As$, repeated 5 times and separated by 5nm InAlAs spacer layers.

Figure 2. Schematic illustration of shape assumed for: (a) a square-based pyramidal dot geometry with base width 2s and surface inclination angle θ ; (b) quantum-dot-assembled wire geometry, triangular cross section in the width, base width and inclination angle are identical with the component dots.

Figure 3. Relation between the ratio of step creation energies α and maximum coalescent dot number N: (a) $\alpha = 6\left(2.5 - (N-1)^{-1} \ln \frac{4N-1}{3} \right)^{-1} - 1$;

(b) $\alpha = \left(2N - 2 + \ln \frac{4N-1}{3} \right)\left(2N - 2 - \ln \frac{4N-1}{3} \right)^{-1}$.

(a)
[1̄10]
[011̄]
250nm

(b)
[1̄10]
[110]
250nm

(c)
[1̄10]
[001]
20nm

(a)

[1$\bar{1}$0]

[110]

(b)

[1$\bar{1}$0]

[110]
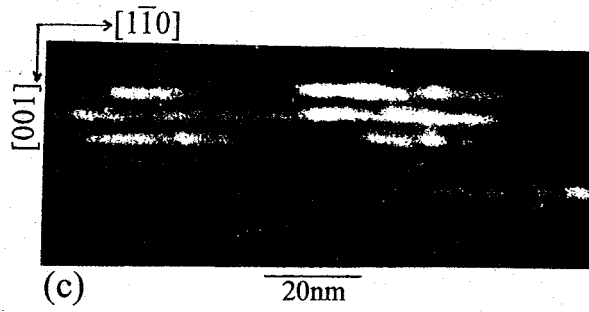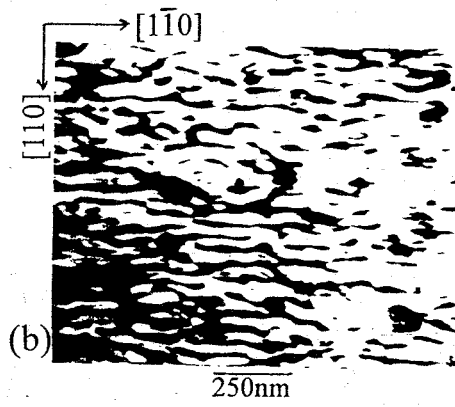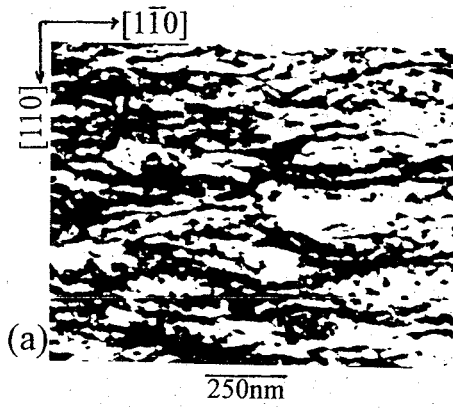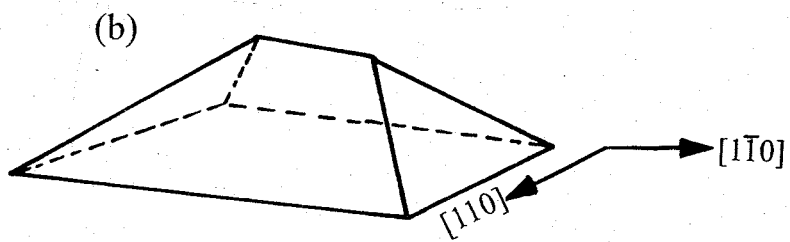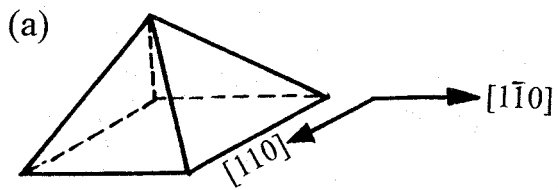
Photoluminescence from Ge clusters embedded in porous silicon

Feng-Qi Liu[a)] and Zhan-Guo Wang
Laboratory of Semiconductor Materials Science, Institute of Semiconductors, Chinese Academy of Sciences, P.O. Box 912, Beijing 100083, China

Guo-Hua Li
National Laboratory for Superlattices and Microstructures, Institute of Semiconductors, Chinese Academy of Sciences, P.O. Box 912, Beijing 100083, China

Guang-Hou Wang
Department of Physics and National Laboratory of Solid State Microstructures, Nanjing University, Nanjing 210093, China

Visible photoluminescence (PL) and Raman spectra of Ge clusters embedded in porous silicon (PS) have been studied. The as-prepared sample shows redshifted and enhanced room temperature PL relative to reference PS. This result can be explained by the quantum confinement effect on excitons in Ge clusters and tunnel of excitons from Si units of the PS skeleton to Ge clusters. One year storage in dry air results in a pronounced decrease in PL intensity but blue-shifted in contrast to reference PS. This phenomenon correlates to the size decrease of macerated Ge clusters and occurrence of "quantum depletion" in Ge clusters. Consequently, only excitons in Si units contribute to PL. © *1998 American Institute of Physics.* [S0021-8979(98)06006-X]

Clusters and cluster-assembled semiconductor materials are currently stimulating much interest, because they show optical and electronic properties which are quite different from those of bulk crystals.[1-5] The visible luminescence in cluster-assembled materials of an indirect gap semiconductor may open up new possibilities for fabricating visible light emitting devices based on group IV semiconductors. Quantum confinement effects play an essential role in the luminescence process. To obtain three-dimensionally confined Ge systems, different groups have exploited a variety of techniques.[6-9] The synthesis of semiconductor clusters inside the cavities of certain zeolites or some of the microporous materials is one promising technique.[10,11] Recently, Ozin and co-workers have prepared Si clusters inside Y–zeolite using the chemical vapor deposition method and observed orange luminescence from them.[11] Filling of the pores network of porous material with semiconductor clusters provides a simple route for the investigation of the quantum confinement effect in clusters.

It is well known that the pore diameter of porous silicon (PS) layers can be varied over a wide range (from 2 to 100 nm).[12] This provides a feasibility of pore filling with Ge clusters. Halimaoui et al.[12] have filled PS pores with Ge and Si using a chemical vapor deposition method at low temperature. However, to our knowledge, no systematic investigation of Ge clusters embedded in PS has been made so far. In this article, we present a comparative study of visible photoluminescence (PL) and Raman spectra of Ge clusters embedded in PS and corresponding reference PS.

A *p*-type ⟨100⟩-oriented silicon wafer with a resistivity of 1–3 Ω cm was used to fabricate PS substrate. The sample was anodized at a current density of 30 mA/cm² in an HF–

ethanol solution (HF:$C_2H_5OH=2:1$) for 15 min. The anodization was carried out under illumination with a 150 W halogen lamp from a distance of 25 cm. The pores of PS are no less than 13 nm in diameter. Ge clusters were produced by evaporation and inert gas condensation.[13] Ge powder was evaporated in a tungsten boat in Ar gas atmosphere. The clusters were deposited on one-half of a PS substrate; the other half was used as a reference PS. Due to the spongelike structure of PS, the pores are a labyrinth. Therefore, small Ge clusters can softly drop into the pores and weakly touch one another. All optical measurements were made at room temperature, using an Ar+ laser as an excitation with a wavelength at 488 nm. The power was about 50 mW to prevent heating of the absorptive sample. Both Raman and PL spectra were taken at the same sport and during the same run.

To estimate the size of Ge clusters, we use Raman scattering for the structure analysis. Raman spectra of the as-prepared Ge cluster-embedded in PS (Ge–PS) and reference PS are shown in Fig. 1. Reference PS shows only a peak at 516 cm⁻¹. For Ge–PS, besides a peak at 516 cm⁻¹, a small peak at 298.5 cm⁻¹ emerges. The small peak at 298.5 cm⁻¹ reflects the Raman active transverse optical (TO) mode of the introduced Ge clusters. There is no evidence of the Si–Ge alloy mode between 300 and 520 cm⁻¹, indicating that the intermixing at the Ge/Si interfaces is small. The deviation of the TO peak position from that of corresponding bulk Ge correlates with the average cluster size, and the formula proposed by Cardona[14] is:

$$d_R = 2\pi(C/\Delta\omega)^{1/2},$$

where d_R is the average cluster size, $\Delta\omega$ is the deviation of the TO peak, and $C=0.96$ nm² cm⁻¹ for Ge. According to this formula, we obtained the average size of the clusters, which is 5 nm. Figure 2 shows the PL spectra of Ge–PS and

[a)]Electronic mail: fqliu@red.semi.ac.cn
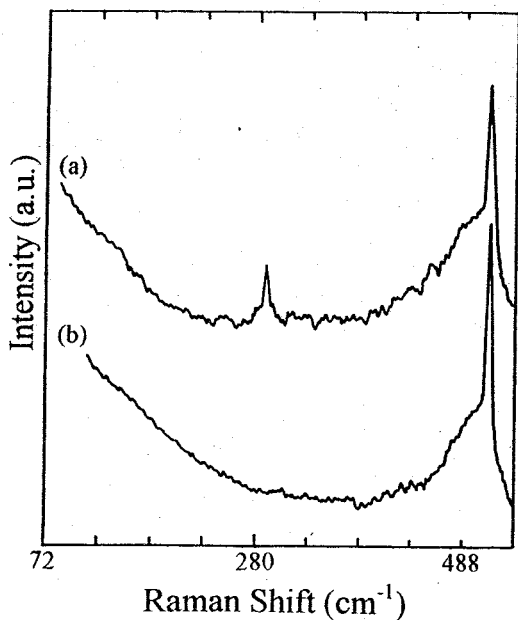
FIG. 1. Raman spectra of as-prepared (a) Ge cluster-embedded in PS and (b) reference PS.

FIG. 3. Raman spectra of prolonged air-stored (a) Ge cluster-embedded in PS and (b) reference PS.

reference PS. The PL peak energies of Ge–PS and reference PS are 1.8 and 1.87 eV, respectively. Compared with the reference PS, Ge–PS appears narrow and enhanced PL. What is more, this feature can be repeated. Even though the presence of some unavoidable nonuniformity of PS substrate may lead to a slight shift of the PL peak, the PL width and

intensity scarcely change. Consequently, the obvious difference in PL of Ge–PS and reference PS correlates to the Ge clusters.

We now come to the PL mechanism in Ge–PS. Since Ge has smaller electron and hole effective masses and a larger dielectric constant than Si, the effective Bohr radius of the excitons in Ge is larger than that in Si, and the quantum confinement effect appears more pronounced in Ge than in Si. A theoretical calculation[15] shows that the indirect band gap energy of Ge clusters is very sensitive to the size of clusters. Therefore, the introduced Ge clusters are expected to display room temperature PL, and a shoulderlike or double-peak structure of PL from Ge–PS is presumed. No shoulderlike structure in the overall PL spectrum indicates that the original luminescence stems from only one constitute of the materials. To explain our result, we propose a model for the PL mechanism of Ge–PS as follows: (1) Due to quantum confinement effect, photoexcitation creates excitons in the nanoscale Si and Ge units (2) In Ge–PS, the diagram of the band gap of the Si unit/interfacial/Ge cluster core acquires a asymmetric shape. (3) The thin interfacial region is a mixture of SiO_x and possible GeO_y. The band gap of the nonstoichometric SiO_x is in the range of 1.8–4 eV depending strongly on the composition,[16] and the band gap of GeO_y is even larger.[9] Because the band gap of 5 nm Ge clusters is smaller than that of Si units (1.87 eV), the carriers in Si units rapidly tunnel into the Ge cluster cores, and radiatively recombine there. This physical picture of PL indicates that the original luminescence of Ge–PS stems from excitons confined in Ge clusters. From the PL peak energy of Ge–PS, the calculated average size of the Ge cluster is 4.8 nm. This value is approximately consistent with the average size estimated by means of Raman spectroscopy. Therefore, our experimental results favor the quantum confinement effect and support the above model. Due to fabrication in the vacuum condition, the Ge cluster is free of adsorbed species.

FIG. 2. Room temperature photoluminescence spectra of as-prepared (a) Ge cluster-embedded in PS and (b) reference PS.
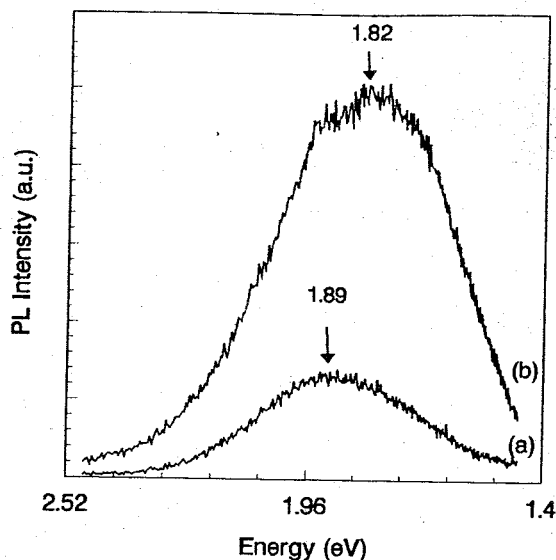
FIG. 4. Room temperature photoluminescence spectra of prolonged air-stored (a) Ge cluster-embedded in PS and (b) reference PS.

Consequently, in Ge–PS, the surface of the Ge cluster is "clearer" than the Si unit of PS. Then a decrease of the nonradiative channels, which can be related to a decreased density of trap states, leads to an increase in the PL intensity. The relative narrow size distribution of Ge clusters results in narrowing of the PL width.

When the same sample is subjected to 1 year storage in dry air, the optical properties change drastically. Two characteristic points should be noted. One point is that the Ge cluster-related Raman peak shifts to 300.5 cm^{-1} as shown in Fig. 3. This peak is broad and weak compared with that of the fresh sample. Due to a long time storage in ambient air, the embedded Ge clusters eventually were macerated by the PS skeleton. The interfacial regions between Ge clusters and Si units may contain SiGe intermixture. The compressive strain at the interfaces, results in Ge–Ge vibration appears at higher energy.[17] The other characteristic point is the striking decrease in PL intensity and slightly blueshift in PL energy of Ge–PS relative to reference PS as shown in Fig. 4. In contrast to the as-prepared sample, both luminescence from Ge–PS and from reference PS originate from excitons confined in Si units of the PS skeleton. This scenario can be explained as follows. Since the Ge clusters were macerated by the PS skeleton, Ge clusters decreased in size, and the remanent Ge clusters or "superatoms" were coated in the inner walls of the PS pores. The band gap increment of Ge clusters is pronounced. The asymmetric band gap of the Si unit/interfacial/Ge cluster core and the very small size of Ge clusters lead to the absence of bound states in Ge clusters. As a result, a "quantum depletion" takes place in Ge clusters that drives the charges toward the Si units.[18] On the other hand, interfacial disorder and large interface-to-volume ratio increase the density of nonradiative recombination centers and degrade PL intensity to a large extent, and for this reason the smearing surface between the Si unit and Ge cluster bring about a reduction in luminescence. In addition, surface tensions of Si units due to intermixing possibly yield cracking and partial disintegration of the PS skeleton, probably causing surface trap states, further reducing PL intensity. The PL width of Ge–PS changes a little in comparison with that of reference PS, indicating that the size distribution of Si units in the Ge cluster-embedded region scarcely change. The slightly inconsistent PL peak position of reference PS in Figs. 2 and 4 relates to the unavoidable nonuniform etching.

In summary, we have preformed PL and Raman spectra investigation of Ge cluster-embedded in PS. As-prepared sample exhibits enhanced PL but blueshifted relative to reference PS. This result can be attributed to the photoexcited excitons in Si units which tunnel into the Ge cluster cores. A long time ambient air storage of the sample results in the maceration of Ge clusters by the PS skeleton. A striking increase of band gap of Ge cluster due to the size decrease leads to "quantum depletion" in Ge clusters. The luminescence originates from the quantum confinement effect on excitons in Si units of the PS skeleton.

[1] A. G. Cullis, L. T. Canham, and P. D. J. Calcott, J. Appl. Phys. **82**, 909 (1997), and references therein.
[2] A. Saito and T. Suemoto, Phys. Rev. B **56**, R1688 (1997); and references therein.
[3] Y. Madea, N. Tsukamoto, Y. Yazawa, Y. Kanemitsu, and Y. Masumoto, Appl. Phys. Lett. **59**, 3168 (1991).
[4] Y. Kanemitsu, H. Uto, Y. Masumoto, and Y. Maeda, Appl. Phys. Lett. **61**, 2187 (1992).
[5] M. Nogami and Y. Abe, Appl. Phys. Lett. **65**, 2545 (1994).
[6] S. Okamoto and Y. Kanemitsu, Phys. Rev. B **54**, 16 421 (1996).
[7] A. K. Dutta, Appl. Phys. Lett. **68**, 1189 (1996).
[8] V. Cracium, C. Boulmer-Leborgne, E. J. Ncholls, and I. W. Boyd, Appl. Phys. Lett. **69**, 1506 (1996).
[9] Y. Maeda, Phys. Rev. B **51**, 1658 (1995).
[10] C. R. Martin, Science **266**, 1961 (1994), and references therein.
[11] O. Dag, A. Kuperman, and G. A. Ozin, Adv. Mater. **7**, 72 (1995).
[12] A. Halimaoui, Y. Campidelli, P. A. Badoz, and D. Bensahel, J. Appl. Phys. **78**, 3248 (1995).
[13] F. Q. Liu, L. S. Liao, G. H. Wang, G. X. Cheng, and X. M. Bao, Phys. Rev. Lett. **76**, 604 (1996).
[14] M. Cardona, in *Light Scattering in Solids*, edited by M. Cardona and G. Guntherodt (Springer, Berlin, 1982), Vol. II, p. 80.
[15] T. Takagahara and K. Takeda, Phys. Rev. B **46**, 15 578 (1992).
[16] M. Zacharias, D. Dimova-Malinovska, and M. Stutzmann, Philos. Mag. B **73**, 799 (1996).
[17] J. Menéndez, A. Pinczuk, J. Bevk, and J. P. Mannaerts, J. Vac. Sci. Technol. B **6**, 1306 (1988).
[18] E. Palange, G. Capellini, L. Di Gaspare, and F. Evangelisti, Appl. Phys. Lett. **68**, 2982 (1996).

Photoluminescence from surface-oxidized Ge nanoclusters

Feng-Qi Liu [a,1], Zhan-Guo Wang [a], Guang-Hou Wang [b]

[a] *Laboratory of Semiconductor Materials Science, Institute of Semiconductors, Chinese Academy of Sciences,*
P.O. Box 912, Beijing 100083, China

[b] *Department of Physics and National Laboratory of Solid State Microstructures, Nanjing University, Nanjing 210093, China*

Abstract

Photoluminescence from gas-evaporated Ge nanoclusters consisting of a crystalline core encased in an oxide shell are presented. An as-grown sample shows room temperature luminescence with separate peaks around 357 and 580 nm. Prolonged air exposure of the clusters reduces the Ge core dimensions, and the emission initially at 580 nm shifts to 420 nm; however, the violet luminescence at 357 nm displays no difference. These results indicate that there are two mechanisms involved with light emission from Ge nanoclusters, visible light emission associated with the quantum confinement effect, and violet light emission correlated to luminescent centers. © 1998 Elsevier Science B.V.

Recently, a great deal of research effort has been devoted to visible light emission from Si nanostructures [1,2]. The discovery of luminescence in Si nanoclusters is an extremely important scientific breakthrough with enormous technological implications. Inspired by the previous work on Si nanoclusters, investigation of Ge nanoclusters has also attracted significant attention [3,4]. Many different methods for synthesizing luminescent Ge nanoclusters have been reported, and similar visible photoluminescence (PL) spectra have been observed [3]. Despite many suggestions, the origin of visible PL has not yet been made clear. The principal debate regarding the origin of luminescence seems to be whether or not the luminescence mechanism can be attributed to the radiative recom-

bination of quantum confined electron–hole pairs (or excitons) in Ge nanoclusters (quantum dots) [5–9].

In this Letter, we report the observation of visible PL of Ge nanoclusters prepared by the gas evaporation method. The PL spectrum of an as-deposited Ge nanoclusters film displays a two-peak structure with peak wavelengths around 357 and 580 nm. Prolonged exposure of the sample to ambient air, however, resulted in the PL peak at 580 nm shifting to 420 nm.

Light-emitting Ge nanoclusters were deposited on a single-crystalline Si wafer following the procedure described in Ref. [10]. The base pressure of the vacuum chamber was 6×10^{-6} Torr. The Ge powder with a high purity of 99.999% was evaporated from a W boat in an Ar gas atmosphere. The cluster size was controlled by adjusting the evaporation temperature, the Ar gas pressure, and the distance between the substrate and the W boat. The PL spectra were mea-

---

[1] E-mail: fqliu@red.semi.ac.cn.

sured by using a HITACHI 850 fluorescence spectrophotometer and 250 nm excitation from a Xe lamp. The spectra have been corrected for the spectral response of the instrument. Raman measurements were carried out in a conventional 90° scattering configuration. The spectra were recorded by a double-grating monochromator and a standard photo-counting system. We used the 488 nm line of an argon ion laser as the excitation source whose power at the sample was less than 5 mW to avoid local heating. Since ambient air oxidation is inevitable, each cluster is composed of a crystalline core and an amorphous oxide shell $\sim$ 1.2 nm thick under room temperature ambient condition [11]. Further, oxidation modifies the shape of small cluster [12]. A prolonged ($\sim$ 4 months) oxidation reduces the mean cluster core size and modifies the shape still more. Thus, the optical properties of an as-prepared sample will be different from that of a prolonged air-exposed sample.

Fig. 1 shows the PL spectra of (a) an as-deposited Ge nanoclusters sample and of (b) a prolonged air-oxidized sample. The PL spectra were measured under 250 nm photoexcitation and a 350 nm shortcut filter was put behind the sample. The spectrum (a) includes two peaks at wavelengths of 357 (violet light emission) and 580 nm (red light emission). The red emission is broad and weak. In spectrum (b) the PL peaks are displaced to around 359 and 420 nm . The intensity of the 357 nm peak in spectrum (a) is nearly the same as that of 359 nm in spectrum (b), but the blue light emission around 420 nm in spectrum (b) is stronger than that of the red light emission near 580 nm in spectrum (a). These observations strongly suggest that there are two kinds of PL mechanisms. The core size of as-deposited nanoclusters is larger than that of prolonged air-oxidized nanoclusters. The red emission in an as-deposited sample shifts to the blue region in a prolonged air-oxidized sample correlates with the decrease of nanocluster size. We assign this feature to the quantum confinement effect on electrons and holes in nanoclusters. The violet light emission shows no size dependence, indicating that the violet light emission arises from luminescent centers.

To verify the size change of a nanocluster when subjected to oxidation in ambient air, we have performed Raman measurements for both samples. The results are shown in Fig. 2. The as-deposited sample shows a Raman peak at 297 cm^{-1} and a broad and
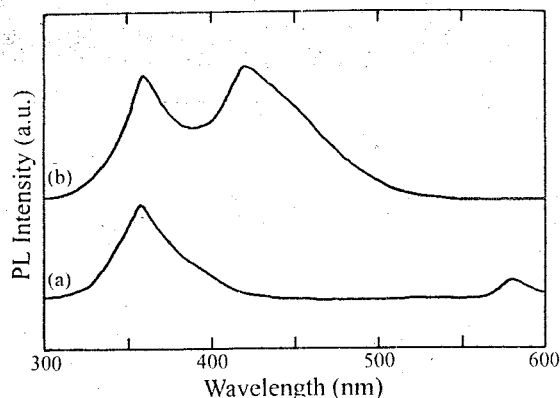

Fig. 1. Room temperature photoluminescence spectra under 250 nm excitation of (a) an as-deposited and (b) a prolonged air-oxidized Ge nanocluster samples.
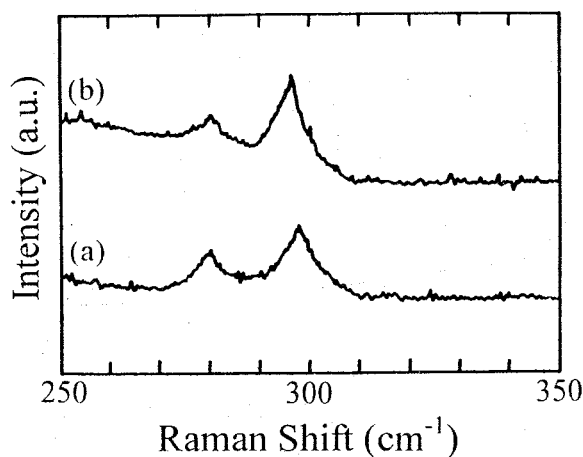

Fig. 2. Raman spectra of (a) an as-deposited and (b) a prolonged air-oxidized Ge nanocluster samples.

weak band centered near 280 cm^{-1} (spectrum a). The Raman spectrum of a prolonged air-oxidized sample (spectrum b), peaking at 296 and 280 cm^{-1}, is very similar to that of the as-deposited sample. The peaks near 300 cm^{-1} originate from an optical phonon (TO-like mode: Γ'_{25}) scattering of Ge nanoclusters, and the deviation of this TO peak position from that of single-crystal Ge at 300 cm^{-1} relates to the finite size effect of a nanocluster. This Raman spectrum feature bears resemblance to that reported by Heath et al. on Ge nanoclusters synthesized via the ultrasonic mediated reduction method [13]. The broad component centered near 280 cm^{-1} is an amorphous-like Raman signal. This feature comes from the surface layers of nanoclusters, whose atomic arrangement is more or less in disorder [14]. Finite size effects relax the k

vector selection rule and this relaxation of the moment conservation leads to a down shift and broadening of the Raman spectrum. An accurate phonon confinement model proposed by Sasaki and Horie [15] can be used for the calculation of the cluster size. However, because of optical phonon softening, lattice expansion [15], and the oxidation induced variation in shape due to changes of the surface tension [12], the real phonon dispersions of Ge cluster is unknown. Thus, we cannot evaluate the cluster size by the above model. As a rough estimation, we use the formula proposed by Cardona [16] to calculate the cluster size. The formula is

$$d_R = 2\pi (C/\Delta\omega)^{1/2},$$

where d_R is the average nanocluster size, $\Delta\omega$ is the deviation of the TO peak, and $C = 0.96$ nm^2 cm^{-1}. In calculation, the lattice-expansion induced frequency shift of 0.5 cm^{-1} in the Ge nanocluster [15] should be subtracted from the observed overall frequency shift. According to this formula, we obtained the average sizes of the nanoclusters, which are 3.9 and 3.4 nm in (a) and (b), respectively. This indicates that a prolonged oxidation reduces the cluster size by 0.5 nm. An interesting aspect is that the TO peak of the smaller clusters (b) has a smaller width as compared to the larger clusters. We think this unexpected feature relates to surface modification and self-limiting oxidation of Ge clusters. The surface modification due to changes of surface tension and bond-angle disorder strongly influences the phonon density of states and dispersion relation [12,17]. The self-limiting oxidation of the Ge clusters results in uniformity in core size, leading to the smaller width of the TO peak. This oxidation retardation is larger for smaller radii and at lower temperatures, where the viscosity of the newly formed oxide is higher. What is more, to have such a self-limiting oxidation effect, the nanocluster shell should be first oxidized [7].

We discuss the mechanism of room temperature PL from surface-oxidized Ge nanoclusters. The above results clearly demonstrate the distinct size shrinkage due to a prolonged air oxidation. Knowing that both GeO_2 and Ge exhibit no visible PL, we suggest that the visible PL (420 and 580 nm) as observed in Fig. 1 arises from the quantum size effects of the Ge nanoclusters. In Ge nanoclusters the effective masses for electrons and holes are very small. Since the exciton Bohr radius in the bulk material is generally larger for the case of smaller carrier masses, the quantum confinement effect appears more pronounced in Ge than in Si. A theoretical calculation [18] shows that the indirect band gap energy of the Ge nanoclusters is very sensitive to the size of nanoclusters. Maeda [9] has confirmed that there is a critical size showing the quantum size effect and this critical size is smaller than roughly 5 nm. From the peak energies of the red light emission band of an as-deposited sample and the blue light emission band of a prolonged air-oxidized sample, the calculated average nanocluster sizes are 4.2 and 3.4 nm, respectively. These values are consistent with the average size estimated by means of Raman spectroscopy. Therefore, our result, a correlation of Raman and PL spectra, provides strong evidence of the quantum size effect in Ge nanoclusters. The presence of dangling bonds at the Ge nanocluster surface affects the radiative efficiency [9], and determines whether we can observe the luminescence or not. From this viewpoint, the surface oxides of nanoclusters are important for the enhancement of radiative efficiency. The Ge–O bonding at the nanocluster surface gives a barrier potential larger than 4 eV [9]. In this case, nonradiative channels can be inhibited, so that we can get enough radiative efficiency to observe the visible luminescence.

The ultraviolet emission reported here is the shortest wavelength reported to date. At present, we have no sound explanation of this result. On the basis of the quantum confinement–luminescent center (QCLC) model proposed by Qin et al. [19], which is used to explain the ultraviolet emission from porous silicon, we might explain our experiment results. For the oxidized Ge nanoclusters, according to the QCLC model, the electron–hole pairs that are photoexcited in Ge nanoclusters transfer outward and recombine at the luminescent centers located at the interfaces of Ge cluster cores/GeO_x or tunnel into the luminescent centers located in GeO_x shells encasing the Ge cluster cores and recombine there. If the luminescent centers have light-emitting energies in the ultraviolet region, then the ultraviolet light emission could be observed. Further work is needed to elucidate the origin of the ultraviolet emission.

In summary, we have demonstrated ultraviolet and visible PL at room temperature in Ge nanoclusters

consisting of a crystalline core encased in an oxide shell fabricated by the gas-evaporation method. Two mechanisms involved with light emission from Ge nanoclusters are found, the pronounced change from red to blue light emission is associated with the quantum size effect, and the size-independence of ultraviolet light emission is correlated to luminescent centers located on the interfaces between the cluster core and Ge oxide or in Ge oxide shells.

References

[1] S. Furukawa, T. Miyasato, Jpn. J. Appl. Phys. 27 (1988) L2207.

[2] H. Takagi, H. Ogawa, Y. Yamazaki, A. Ishizaki, T. Nakagiri, Appl. Phys. Lett. 56 (1990) 2379.

[3] Y. Madea, N. Tsukamoto, Y. Yazawa, Y. Kanemitsu, Y. Masumoto, Appl. Phys. Lett. 59 (1991) 3168.

[4] Y. Kanemitsu, H. Uto, Y. Masumoto, Y. Maeda, Appl. Phys. Lett. 61 (1992) 2187.

[5] S. Okamoto, Y. Kanemitsu, Phys. Rev. B 54 (1996) 16421.

[6] A.K. Dutta, Appl. Phys. Lett. 68 (1996) 1189.

[7] V. Cracium, C.Boulmer-Leborgne, E.J. Ncholls, I.W. Boyd, Appl. Phys. Lett. 69 (1996) 1506.

[8] K.S. Min, K.V. Scheglov, C.M. Yang, H.A. Atwater, M.L. Brongersma, A. Polman, Appl. Phys. Lett. 68 (1996) 2511.

[9] Y. Maeda, Phys. Rev. B 51 (1995) 1658.

[10] F.Q. Liu, L.S. Liao, G.H. Wang, G.X. Cheng, X.M. Bao, Phys. Rev. Lett. 76 (1996) 604.

[11] M. Han et al., Jpn. J. Appl. Phys. Suppl. 34 (1994) 49.

[12] T. Brandt, W. Hoheisel, A. Iline, F. Stietz, F. Trager, Appl. Phys. B 65 (1997) 793.

[13] J.R. Heath, J.J. Shiang, A.P. Alivisatos, J. Chem. Phys. 101 (1994) 1607.

[14] S. Hayashi and Yamamoto, Superlatt. Microstruct. 2 (1986) 581.

[15] Y. Sasaki and Horie, Phys. Rev. B 47 (1993) 3811.

[16] M. Cardona, in: Light Scattering in Solids, eds. M. Cardona, G. Guntherodt (Springer, Berlin,1982), Vol. II, p. 80.

[17] M. Fujii, S. Hayashi, K. Yamamoto, Jpn. J. Appl. Phys. 30 (1991) 687.

[18] T. Takagahara, K. Takeda, Phys. Rev. B 46 (1992) 15578.

[19] G.G. Qin, X.S. Liu, S.Y. Ma, J. Lin, G.Q. Yao, X.Y. Lin, K.X. Lin, Phys. Rev. B 55 (1997) 12876.

致 谢

在我从事博士后研究工作期间，合作导师王占国院士在学术上给予了多方面的指导，在生活上提供了诸多的帮助，谨在此致以最诚挚的谢意。

在两年愉快、紧张的合作研究期间，徐波工程师、钱家骏研究员、陈伟研究员、梁基本研究员在实验方面提供了友好合作和帮助，在此表示感谢。感谢同组的其它老师和博士生们在实验方面提供的协作。

在项目的合作和实施期间，得到张权生研究员多方面的帮助，在合作、讨论中开阔了眼界，愿今后能与张老师愉快、务实、高效地合作。

工作中得到北京大学郭长志教授和清华大学陈水莲教授的具体指导和帮助。在合作研究中，郭先生忘我工作的精神、渊博的学识和严谨的学风，使我受益匪浅。唯有今后加倍努力，才不辜负先生教诲。

感谢王玉田研究员、高维滨研究员、孙明芳高工、陈涌海博士、李国华研究员在对我的帮助。

感谢博士后流动站的领导及所领导对博士后研究工作的关心和严格要求。

博士后流动期间以第一作者身份发表和即将发表的学术论文

1. Photoluminescence from Ge clusters embedded in porous silicon.
   J.Appl.Phys.*Communications*, **83,** 3435 (1998).

2. Photoluminescence from surface oxidized Ge nanoclusters.
   Phys.Lett.A 242/3, 169 (1998).

3. Structure and photoluminescence of InGaAs self-assembled quantum dots
   grown on InP(001).
   J.Appl.Phys.*Communications*, (in press).

4. Size quantization effects in InAs self-assembled islands on InP(001) at the
   onset of 2D-to-3D transition. (submitted to **J.Cryst.Growth**)

5. Metamorphosis of Self-organized Quantum dots into Quantum Wires.
   (submitted to **Appl.Phys.Lett**)

个人简历

刘峰奇，男 1963 年 10 月 10 日出生于河南中牟县。 1981 年 9 月进入河南师范大学物理系， 1985 年 6 月获理学学士学位后留校任教。 1987 年 9 月进入中国科技大学物理系(半导体物理专业)攻读硕士学位，在金怀诚教授和刘洪图教授指导下开展"稀土离子注入单晶硅经快速热退火后的深能级研究"和"非晶硅薄膜材料及太阳能电池研究"。1990 年 7 月获理学硕士学位。 1990 年 8 月至 1993 年 8 月河南师范大学物理系任教并参加"高温超导材料微结构及超导机理研究"及主持"优质 ZnO 压敏陶瓷实用化研究"，1991 年晋升讲师职务。 1993 年 9 月进入南京大学物理系凝聚态物理专业攻读博士学位，在王广厚教授的指导下参加国家自然科学基金资助项目"金属团簇尺寸选择和过渡特性研究"、"团簇构成量子结构材料研究"、" IV 族支撑团簇及其构成纳米材料研究"、以及"团簇结构研究和特殊稳定团簇探索"等。主要对 Si 、 Ge 、 LiF 团簇及团簇组装纳米材料进行研究。 1996 年 6 月获理学博士学位。 1996 年 7 月进入中科院半导体研究所博士后流动站，开展 InP 基超薄层微结构材料研究。 1997 年 6 月在半导体研究所晋升副研究员职务。

95 年 12 月获固体微结构物理国家重点实验室颁发的"天马"奖。

已在 Phys. Rev. Lett.， Appl. Phys. Lett.， Phys. Rev. B 等学术刊物上发表多篇论文。